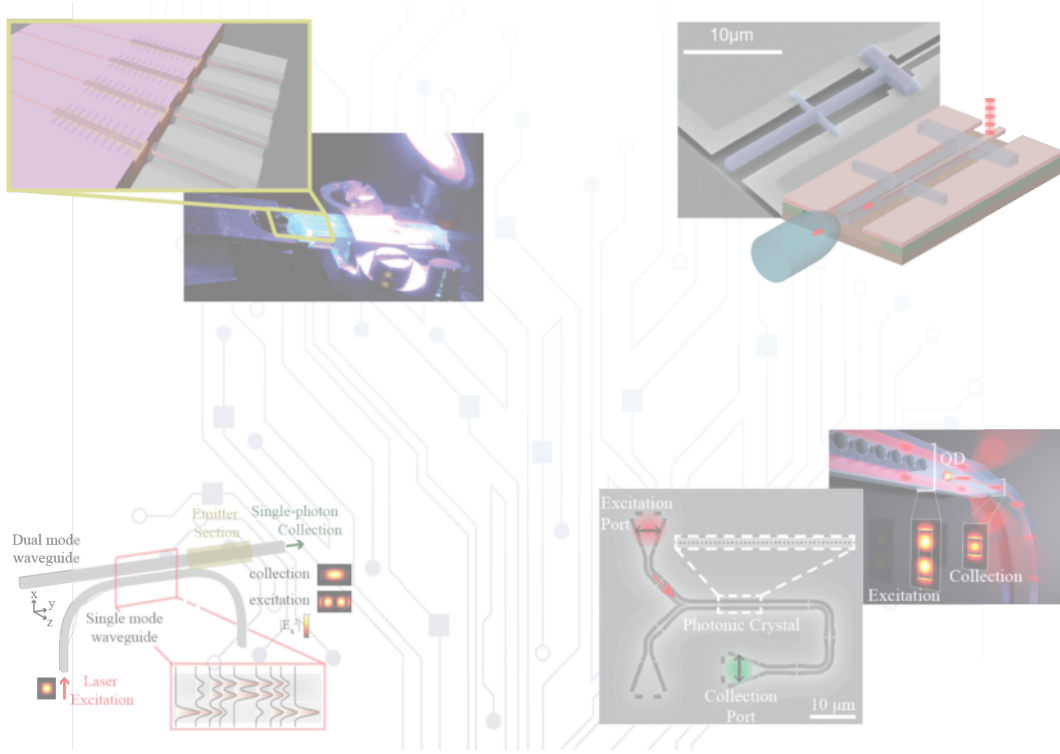


PH.D. THESIS

NOVEL OPTICAL POLYMER-BASED INTERFACES TO QUANTUM PHOTONIC INTEGRATED CIRCUITS



ASLI DİLARA UĞURLU
AUGUST 31, 2021

COVER IMAGE
DEVICE IMAGES PRESENTED WITHIN THIS THESIS.

COLOPHON
This thesis was set with \LaTeX using the memoir class.
The font is Libertine 10, on normal A4 paper
Graphics created using MATLAB, Blender, as well as Adobe Illustrator.
Chapterstyles courtesy CP3.

NOVEL OPTICAL POLYMER-BASED INTERFACES TO QUANTUM PHOTONIC INTEGRATED CIRCUITS

Author Asli Dilara Uğurlu
Advisor Prof. Peter Lodahl
Advisor Assoc. Prof. Leonardo Midolo



UNIVERSITY OF
COPENHAGEN

QUANTUM PHOTONICS

Center for Hybrid Quantum Networks (Hy-Q)
The Niels Bohr Institute

This thesis has been submitted to
The PhD School of The Faculty of Science
University of Copenhagen

August 31, 2021

ABSTRACT

A deterministic source of coherent single photons is a basic building block for future quantum technologies including quantum communication and quantum computation. Platforms based on quantum dots integrated into nanophotonic structures allow the realization of excellent of single-photons sources with the promise of scaling up towards multiple photons and emitters. However, it remains a great challenge to realize deterministic single-photon sources which meet all requirements useful for quantum information processing. For this reason, the implementation of highly efficient, highly coherent, and scalable sources of single photons that can be integrated with on-chip optical networks is of great interest for creating photonic quantum processors.

In this thesis, we advance the on-chip integration of quantum dot platforms to realize scalable multi-photon operation with an architecture that exhibits stability and compatibility with cryogenic temperatures. With a robust fabrication yield in excess of 90%, this work represents a step towards the realization of photonic quantum simulation and quantum computing systems that utilize mature integrated chip technologies. We successfully implemented efficient spot-size converters in planar nanostructures using a novel fabrication method that integrates optical polymers with suspended waveguides. This efficient interface is crucial for scalable heterogeneous integration with low-loss programmable optical networks (realized in e.g. silicon or silicon nitride waveguides) with the potential for large-scale demonstrations of quantum advantage. By further integration with a quantum-dot-based single-photon source on III-V semiconductor platform, we realized a quantum optical interface for lensed fibers, resulting in $\approx 48\%$ chip-to-fiber coupling. However, with optimized fabrication and perfect alignment, this efficiency is theoretically capable of asymptotically approaching unity.

Resonant excitation of quantum dots is the preferred method for generating highly-coherent single-photons. However, resonant excitation poses challenges in rejecting the excitation laser background. Conventionally, background rejection comes at the expense of excess loss that is incompatible with quantum information processing schemes. In this thesis, we demonstrate a novel resonant excitation scheme that leverages the potential of planar nanostructures. Through careful on-chip optical mode engineering, we achieve $> 80\%$ single-photon coupling efficiency into the waveguide, while maintaining laser suppression better than $< 10^{-4}$. The resulting on-chip single-photon source exhibits high-purity ($g^{(2)}(0) = 0.020 \pm 0.005$) and high-indistinguishability ($V = 96 \pm 2\%$). Additionally, we propose a modification in device design for in-plane resonant excitation through the on-chip waveguide. This improvement allows for stronger suppression of the background laser signal ($\sim 10^{-8}$), further boosting the single-photon purity. Subsequently, the operation bandwidth is increased by over an order of magnitude, enhancing the power performance of the resonant excitation.

Further, to demonstrate the potential of the integration and scalability of the platform, we investigated simultaneous coupling of multiple waveguides via chip-to-fiber-array interfacing as well as chip-to-chip interfacing. For this, a novel fabrication method based on glue microdeposition and microfluidics was pursued to fabricate long suspended

tapers that are compatible with quantum experiments at cryogenic conditions. A specific use-case of chip-to-chip interfacing involving gallium arsenide and lithium niobate circuits was explored. Such an approach is expected to reduce interface losses and architecture complexity, compared to multiple chip-to-fiber interfaces. The work of this thesis explores a pathway towards a complete plug-and-play single-photon source where multiple QDs can be triggered simultaneously to emit coherent single photons with high purity and indistinguishability.

SAMMENFATNING

En deterministisk kilde af kohærente enkeltfotoner er en grundkomponent for fremtidige kvanteteknologier inklusiv kvantekommunikation and kvantecomputere. En platform baseret på kvanteprikker integreret i fotoniske nanostrukturerer muliggør glimrende kilder af enkeltfotoner, som ydermere kan skalleres i antal. Dog er det udfordrende at realisere en deterministisk enkeltfoton kilde, som opfylder de mange krav forbundet med kvanteinformations-processering. I forhold til at skabe fotoniske kvanteprocessorer er implementeringen af særdeles effektive, kohærente og skalerbare kilder af enkeltfotoner, der kan interfaces med on-chip optiske netværk, derfor af stor interesse.

I denne afhandling forbedre vi on-chip integrationen af kvanteprikker for at realisere skalerbare multifoton-operation med en tilgang, som udviser stabilitet og er kompatibel med cryogene temperaturer. Ved at anvende en fabrikations process med over 90% succesrate udgør dette arbejde et skridt mod fotonisk kvantesimulation og kvantecomputersystemer, som udnytter modne chip-integrations teknologier. Det lykkedes os at implementere effektiv konvertering af den optiske mode størrelse indenfor plane nanostrukturer. Dette opnår vi med en original fabrikationsmetode, som integrerer optiske polymere med svævende bølgeledere. Dette effektive interface er altafgørende for skalerbar hetrogen integration med lav-tabs programmerbare optiske netværk (lavet af f.eks. silicium eller siliciumnitrat bølgeledere) og har potentiale for stor-skala demonstrationer af kvanteoverlegenhed. Vi integrerer desuden kvanteprik-baserede enkeltfoton-kilder med en III-V halvlederplatform, og dermed opnår vi et kvanteoptisk interface for optiske fibre med integrerede linser, hvilket resulterer i en $\approx 48\%$ chip-til-fiber koblingseffektivitet.

Resonant excitation af kvanteprikker er den fortrukne metode til generere enkeltfotoner med meget høj kohærens. Dog udgør resonant excitation udfordringer I forhold til at undertrykke excitationslaser-baggrund. Normalt resulterer undertrykkelsen I et optisk tab, som er inkompatibelt med kvanteinformationsprocessering. I denne afhandling demonstrerer vi en original resonant excitationmetode, som udnytter potentialet af plane nanostrukturer. Igennem forsigtig optimering af den optiske mode på chippen opnår vi en $> 80\%$ enkelt-photon koblingseffektivitet ind i bølgelederen og en excitationslaser-undertrykkelse bedre en $< 10^{-4}$. Dette fører til, at vores on-chip enkeltfoton-kilde demonstrerer høj enkeltfoton-renhed ($g^{(2)}(0) = 0.020 \pm 0.005$) og høj fotonensartethed ($V = 96 \pm 2\%$). Ydermere foreslår vi forbedringer af designet for i-plan resonant excitation. En sådan forbedring vil medføre forøget undertrykkelse af laserbaggrunden ($\sim 10^{-8}$) og dermed en forøgelse af enkeltfoton-renheden. Ydermere vil båndbredden kunne øges med en størrelsesorden. Endelig vil disse forbedringer øge robustheden mod fabrikationsfejl og dermed øge den eksperimentelle reproducerbarhed samt forøge fabrikationsudbyttet.

For at yderligere demonstrere potentialet af vores platforms integration og skalerbarhed undersøger vi muligheden for simultant at koble flere bølgeledere; enten via chip-til-fiberrække interfaces eller via chip-til-chip interfaces. Vi forsøgte at fabri-

kere lange sværende fiberindsnævninger, som er kompatible med cryogene forhold. Denne fabrikation var baseret på en nyskabende teknik, som kombinerede mikroaflejring af lim og mikrovæsker. Vi undersøge desuden en specifik anvendelse af chip-til-chip kobling mellem GaAs og lithiumniobat. En sådan tilgang forventes at reducere interface-inducerede tab og kompleksitet og dermed være fordelagtig frem for adskillige chip-til-fiber koblinger.

Denne afhandling tegner en vej mod komplette plug-and-play enkeltfoton-kilder, hvor adskillige kvanteprikker exciteres og samtidig udsender kohærente enkeltfotoner med høj renhed og ensartet.

ACKNOWLEDGEMENTS

The work presented in this thesis is the result of research in the Quantum Photonics group at the Niels Bohr Institute, University of Copenhagen, led by Prof. Peter Lodahl, with daily supervision provided by Assoc. Prof. Leonardo Midolo. To start with, the topics covered in this thesis are about component development for photonic integrated circuits built for quantum photonic experiments. This thesis work was dedicated to investigating methods to efficiently out-couple single photons to fibers and circuitry designs enabling on-chip resonant excitation of quantum dots. Later, fabrication techniques were investigated to build multi-channel chip-to-fiber and chip-to-chip coupling.

To Peter and Leonardo, I wish to thank you both for cultivating an environment that provided me, and all of the QP family, a place to freely contribute to science and technology in our own ways. To Peter, you are so good at bringing the right scientists together, not only for progressing research goals, but also for creating a family away from our families. To Leonardo, being my “scientific supervisor” can not solely justify your significance; you are really a dearest friend. This page does not allow me to express how thankful I am to you. You truly allowed me to be a scientific explorer, both figuratively and literally. I appreciate that my supervisors let me hitchhike to meet with different scientific cultures. To my *unofficial* supervisor Ravi, I learned a lot from you and a lot here is really *a lot*. Apart from you being a warrior in the lab, you have shown to me what does it mean to love science and to **just do it**.

Of course to the fabulous, labulous mates: you are all way more than colleagues to me. You are extremely creative, unique, and intelligent scientists and it has been a wonderful opportunity to work with you all. Apart from having the QP family, I think we are actually a way bigger family as all of Quantum Optics. There are wonderful stories with each of you that I think it worthy to spare a full page to everyone individually. Here, in the true karaoke style of NBI, I will sing your names only to say thank you for being in my life and for the all memories. I want to give special thanks to all of you one by one. It was more than what one could expect from any research environment. I start my song with all of your names:

To the ones with whom I share a nest: Camille-CamiLove and Alexey-AlexeyBro, my Shieldmaiden Freja, Nils the Nisse, Zhe, Martin, Rodrigo the Pokemaster, Arianne, Sofie, Ying, Ming-Lai, Vasiliki-Vasso, Patrik-Pat, Atefeh, and Beatrice.

And the ones who left the nest: Tommaso, Raphael, Hanna, Xiaoyan, Maxime, Tim, Dapeng, Thomas H., Henri, Chris, Clauderic, Ela, Gabija, Alisa, Chirag, Sören.

And now my song goes to the membrane homies: Eric the Wings Master, Mads, Yannick, Nenad, Letizia, Chris Ostefledt.

And the ones without a lab. Eva, Johann, Yuixiang.

And to others who left the other nests of Hy-Q: Jason, Vincent, Luca, Yegishe, Junxin, Konstantin, Massi.

And to the ones who helped shape the nest, Dennis, Sören, Thomas,

And, lastly, to the wind beneath our wings: Charlotte, Erika, Lisbeth, Frederik.

Now, I need to thank you my family for shaping the route of me as a bird: Tobias my soul, Nihal and Ahmet - big Ugurlus, Ico, Hiko, Ilos, Ezgi, Turker, Miroshko.. Cansın, Irem, Yigit, Verena, Miriam, Vale, Felix, Babsi, Felix, Zahide, Seven, Kian...Kianoosh, Roger, Lena, Hermine..

All you people can you see? can you see? how your love is effecting my reality?
That makes me you larger than life...

A.D.U.

LIST OF PUBLICATIONS

MANUSCRIPTS

- *On-chip deterministic operation of quantum dots in dual-mode waveguides for a plug-and-play single photon source.* R. Uppu, H.T. Eriksen, H. Thyrrerstrup, **Aslı D. Uğurlu**, Y. Wang, S.Scholz, A.D. Wieck, A. Ludwig, M.C. Löbl, R. J. Warburton, P.Lodahl, L.Midolo. Nature Communication, 2020, Vol 11, 3782.
- *Suspended spot-size converters for scalable single-photon devices.* **Aslı D. Uğurlu**, H. Thyrrerstrup, R. Uppu, C. Ouellet-Plamondon, R. Schott, A.D. Wieck, A. Ludwig, P.Lodahl, L.Midolo. Advanced Quantum Technologies, 2019, Vol 3,1900076, Special Issue: Photonic Quantum Technologies.

CONFERENCE PRESENTATIONS

- *Optical polymers for integrated quantum photonics*, Invited Talk. Symposium on Direct Write, Optical, Ion and Electron Beam Lithography, RAITH Workshop, Institute of Science and Technology. Klosterneuburg, Austria (2019, March). **Aslı D. Uğurlu**, H. Thyrrerstrup, R. Uppu, C. Ouellet-Plamondon, R. Schott, A.W. Wieck, A. Ludwig, P.Lodahl, L.Midolo.
- *Suspended spot-size converters for single-photon devices*, Selected Talk. CLEO Europe - EQEC 2019, Light Coupling Session, Munich, Germany (2019, June). **Aslı D. Uğurlu**, H. Thyrrerstrup, R. Uppu, C. Ouellet-Plamondon, R. Schott, A.W. Wieck, A. Ludwig, P.Lodahl, L.Midolo.
- *Suspended spot-size converters for single-photon devices*, Contributed Talk. QCALL Early-stage researchers conference, Palermo, Italy (2019, September). **Aslı D. Uğurlu**, H. Thyrrerstrup, R. Uppu, C. Ouellet-Plamondon, R. Schott, A.W. Wieck, A. Ludwig, P.Lodahl, L.Midolo.

CONTENTS

Abstract v

Acknowledgements ix

List of publications xi

Abbreviation 3

1 Photonic integration for quantum technology 5

- 1.1 On-chip quantum information processing and communication with photons 6
 - 1.1.1 Integrated deterministic sources of single-photons 9
- 1.2 Semiconductor self-assembled quantum dot 10
 - 1.2.1 Performance characteristics of QD based single-photon sources 12
 - 1.2.2 Optical properties of quantum dots 15
 - 1.2.3 Excitation schemes of QDs 18
 - 1.2.4 Coupling between QD emission and nanophotonic waveguides 21
- 1.3 Hybrid integration of integrated quantum photonics 22
- 1.4 Single-photon out-couplers 28

2 Fabrication of Nanophotonic Devices 33

- 2.1 Epitaxially self-assembled Quantum Dots 34
- 2.2 Electron-Beam Lithography 35
 - 2.2.1 Sample preparation 35
 - 2.2.2 Mask design and exposure preparation 37
 - 2.2.3 Exposure and Development 40
- 2.3 Etching 41
 - 2.3.1 Dry etching 41
 - 2.3.2 Wet etching 42
- 2.4 Process modifications for optical polymers 42
- 2.5 Sample Post-Processing 44

3 Realization of Suspended Spot-Size Converters 47

- 3.1 End-fire coupling between optical waveguides 48

3.2	Suspended spot-size converters for lensed fiber coupling	48
3.3	Numerical analysis of the spot-size converter	50
3.4	Characterization of coupling efficiency	53
3.4.1	Single-photon out-coupling efficiency from the device	56
4	In-plane Resonant Excitation for Plug-and-Play Single-Photon Devices	59
4.1	Waveguide Assisted QD Excitation and Efficient Emission Collection	59
4.1.1	Working Principle of the Device	60
4.2	Performance Figure of Merits of the Device	64
4.2.1	Laser Suppression	65
4.2.2	Single-Photon Impurity	66
4.3	Optimized Experimental Setup	69
4.4	Resonance Fluorescence	73
4.4.1	Resonant Spectroscopy	73
4.5	Demonstration of High Purity Single Photons	77
4.6	Photon Indistinguishability	78
5	Improved design of waveguide integrated single-photon sources	81
5.1	Limitations on the laser extinction	81
5.1.1	Discussion on the device imperfections	82
5.1.2	Asymmetric Directional Coupler for In-plane RF	84
5.1.3	Power Budget for Resonance Fluorescence	87
6	Towards Scalable Chip-To-Fiber Interfaces	91
6.1	Multi-port chip-to-fiber coupling	91
6.1.1	Device design	92
6.1.2	Device fabrication	94
6.2	Outlook	99
7	Concluding Remarks	101
A	Developed nanofabrication recipes	103
A.1	Epoxy cladded inverted taper waveguides	103
A.2	Multiport epoxy cladded inverted taper waveguides with optical adhesive	107
B	Heterostructure composition and sample fabrication	113
C	Resonance fluorescence of a two-level emitter	115
	Bibliography	117

ABBREVIATION

APD	Avalanche Photodiode
CB	Conduction Band
CC	Circular Grating Coupler
CCD	Charge-Coupled Device
CPD	Critical-Point Drying
CMOS	Complementary Metal-Oxide-Semiconductor
CW	Continuous Wave
DC	Direct Current
DBR	Diffraction Bragg Grating
E-beam	Electron Beam
EBL	E-beam Lithography
FDTD	Finite Difference Time Domain
FEM	Finite-element-Method
FIB	Focused Ion Beams
FWHM	Full Width Half Maximum
GPS	Global Positioning System
GaAs	Gallium Arsenide
HBT	Hanbury-Brown-Twiss
HF	Hydrofluoric Acid
HOM	Hong-Ou-Mandel
ICP	Inductively Coupled Plasma
IQP	Integrated Photonic Platforms
InAs	Indium Arsenide
LDOS	Local Density of Optical State

MBE	Molecular Beam Epitaxy
MFD	Mode Field Diameter
PBS	Polarization Beam Splitter
PEB	Post-Exposure Bake
PEC	Proximity Effect Correction
Phc	Photonic Crystal
PIC	Photonic Integrated Circuit
PL	Photoluminescence
PSF	Point Spread Function
QD	Quantum Dot
QIP	Quantum Information Processing
RIE	Reactive Ion Etching
RF	Resonant Fluorescence
SEM	Scanning Electron Microscope
SFWM	Spontaneous Four-Wave Mixing
SK	Stranski-Krastanov
SOI	Signal Of Interest
SPDC	Spontaneous Parametric Down-Conversion
SPS	Single-Photon Source
SNSPDs	Superconducting Nanowire Single-photon Detectors
STM	Scanning Tunneling Microscope
SSC	Spot-Size Converter
TE	Transverse Electric Field
Ti:LN	Titanium-Induffed Lithium Niobate
TO	Transistor-Outline
UV	Ultra-Violet
VB	Valance Band
WL	Wetting Layer
wg	Waveguide



PHOTONIC INTEGRATION FOR QUANTUM TECHNOLOGY

Quantum phenomena and the technologies based on them offer new capabilities to existing technological platforms. For nearly a century, numerous advancements in applied sciences and engineering were reliant on quantum mechanics. For instance, studies on atomic and subatomic systems, which form the basis for solid-state, atomic, and molecular physics, shed light on the laws of quantum tunneling, photoelectric effect, and stimulated emission of electromagnetic radiation. Inventions in quantum technologies manifested groundbreaking applications in what is known as the first quantum revolution. For example, lasers gave rise to classical communication based on laser fiber networks, and optical atomic clocks enabled accurate global positioning systems (GPS). Nevertheless, by controlling and manipulating these quantum systems at the individual level, we can exploit the full power of quantum mechanics (Schleich et al., 2016).

The second quantum revolution has arrived by harnessing the principles unveiled by the first quantum revolution and utilization of quantum phenomena such as entanglement, superposition, uncertainty relations and many-body effects. Beyond doubt, engineered novel materials, advances in device miniaturization, and sophisticated processing technologies enable the realization of these quantum phenomena, and ultimately their control (based on, e.g., photons, electrons, atoms, molecules) (Dowling & Milburn, 2002). This interdisciplinary approach focuses on establishing quantum technologies; quantum information processing (quantum computing and simulation), quantum communication, quantum sensing, metrology, quantum imaging, and quantum clocks.

Quantum information processing uses superposition states of light and matter and the entanglement between them. The physical implementation of entanglement generation and integration of the ensemble into large-scale quantum hardware will

unlock powerful quantum algorithms. The complexity of quantum phenomena gives inherent power to quantum algorithms and leads to exponentially faster computation speeds (National Academies of Sciences & Medicine, 2019). For certain tasks, quantum computers can already outperform supercomputers (Arute et al., 2019). Especially when we employ quantum states of light, quantum operations can be carried out with higher sensitivity, and power consumption is drastically decreased (Laucht et al., 2021).

Modern theory of quantum systems has achieved a high level of maturity in developing protocols, algorithms, and software. However, optimizing these quantum systems remains a challenge, since specific material properties are required to realize quantum operations that can provide excellent coherence properties, near-unity efficiency, and low-noise operation. More importantly, miniaturization of these systems is requisite for increasing computational power and operation rate to extend the scope of their potential functionality. Consequently, chip-scale integration requires persistent development to overcome several challenges for optimizing individual quantum systems hosted in different material platforms. Above all, on-chip integration technologies must allow scaling up quantum systems (in terms of the number of high-performance quantum sources, the density of operational devices) and realizing hybrid integration between different platforms.

This chapter will focus on integrated quantum photonics (IQP) using engineered artificial atoms in solid-state architectures, i.e. quantum dots (QD). We will give an overview of integrated, solid-state *III – V* semiconductor-based QDs as an on-demand source of near-identical single-photons with high coherence and purity. Such single-photons are intended to be used as quantum bits (qubits), the fundamental unit for quantum information (C. P. Dietrich et al., 2016; Lodahl et al., 2015). Qubits form the key elements of quantum computing, simulation, and communication. Then we present the single-photon source generation and its relevant figure-of-merits. Finally, we introduce the importance of photonic integration technologies for scaling up operations by hybrid integration methods. Along with this, we will highlight single-photon source out-coupling as a substantial integrated functionality for scaling-up optical interconnects for hybrid integration and read-out operations.

1.1 ON-CHIP QUANTUM INFORMATION PROCESSING AND COMMUNICATION WITH PHOTONS

In quantum information science, states of two-level quantum mechanical systems (such as an atom or a polarized photon) are used to encode qubits. The state of a qubit can be constructed from the basis states $|0\rangle$ or $|1\rangle$, as an “arbitrary complex combination” – a superposition – of them. In classical information processing, a string of n bits can be prepared in one of 2^n states. Meanwhile, in quantum information processing (QIP), n qubits can represent all 2^n states simultaneously. The vital ingredients for QIP and quantum communication is having qubits that exhibit both non-local correlations and entanglement.

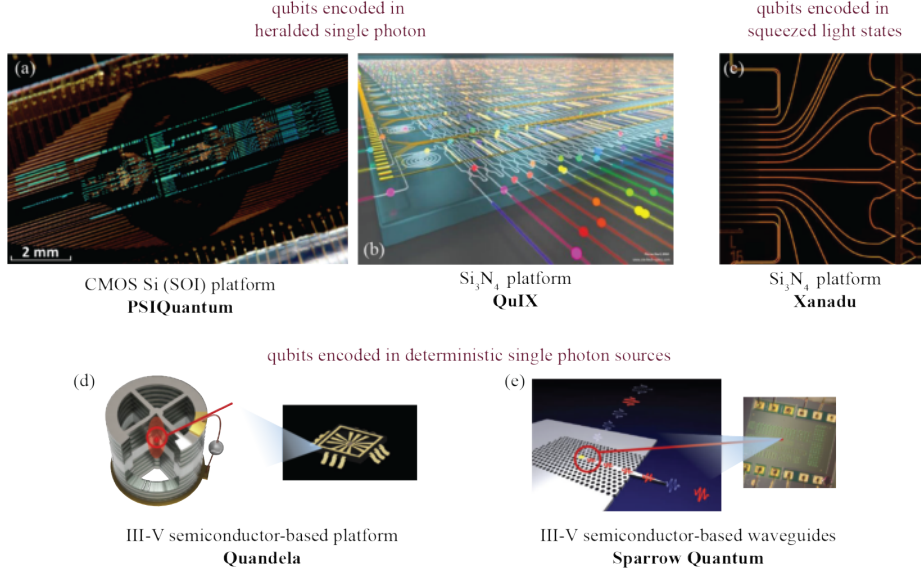


Figure 1.1: Integrated hardware for quantum information processing with photonic qubits. (a) Universal CMOS optical quantum computer by *PSIQuantum* (PsiQuantum, 2021). (b) Si_3N_4 integrated photonics for qubit manipulation for quantum information processing by *QuIX* (Quix, 2021). (c) Photonic quantum computing by squeezed states of light on Si_3N_4 by *Xanadu* (Xanadu, 2021). (d) Solid-state semiconductor deterministic sources of quantum light for quantum applications by *Quandela* (Quandela, 2021). (e) Semiconductor integrated platform with embedded solid-state QD-planar sources for quantum applications by *Sparrow Quantum* (Sparrow, 2021).

The fundamental requisite for realizing a quantum computer and simulator is having scalable physical qubits that can maintain their quantum properties for the amount of time required for the calculations. To perform a universal set of operations (building quantum logic gates), qubits must be first initialized deterministically, their interactions must be controlled, and finally they must be measured (DiVincenzo & Loss, 1998; National Academies of Sciences & Medicine, 2019).

For over two decades, quantum bits have been realized by fundamentally two approaches, matter-based and light-based. Matter-based qubits represent predominantly electronic states such as trapped-ions (motional state) (Monroe & Kim, 2013), superconductors (superconducting flux state) (Devoret & Schoelkopf, 2013), QD semiconductors (spin state) (D. D. Awschalom et al., 2013). Light-based qubits are commonly represented by photonic states, which can be generated by spontaneous parametric down conversion (SPDC) sources in materials with strong second-order optical nonlinearities (e.g. lithium niobate (Meyer-Scott et al., 2020), β -barium borate (Kwiat et al., 1995)) and atom-like structures, such as semiconductor QDs (Kok et al., 2007) and color centers in crystals (Ivady et al., 2019).

Quantum light can be found in different forms: (1) as continuous-variable Gaussian states, which uses wave dimension of light to manipulate the quadrature of the light-field to generate coherent and squeezed states, (2) as discrete-variables, which forms highly pure, coherent, indistinguishable single-photons. The unique advantages of single-photons as qubits arise from their robustness against decoherence as they weakly interact with their environment when isolated. Consequently, they also exhibit low noise. Moreover, their spatial and temporal modes can be regulated. These features make single-photons advantageous for performing calculations reliably (though their lossy nature remains a challenge). Such single-photons emitted by a *stationary qubit* (such as quantum dot, ion traps, neutral atoms, atom-like color centers, or other confined electron systems) are called *flying qubits*. Flying qubits are the most promising candidates for the distribution of quantum information between distant nodes since they can carry states and share entanglement over long distances at the speed of light. (D. Awschalom et al., 2021; O’Brien, 2007). Single-photon sources can enable quantum network architectures by linking quantum memories (Kimble, 2008) or serving as quantum repeaters (Briegel et al., 1998; Ma et al., 2012). However, since the photon-photon interactions are weak, the entanglement generation between them can be more challenging than matter-qubit systems.

Semiconductor materials are transparent to light of certain wavelength bands, enabling the coherent transmission of single photons through them. Additionally, the mature and well-established toolkits of nanofabrication methods and the design flexibility of photonic integration platforms enable building complex circuits with high stability. We affirm these properties will lead to the robustness of on-chip logic operations required for quantum algorithms. Additionally, single-photons have multiple degrees of freedom. Quantum information can be encoded as time-bin (early/ late detection), path (propagation direction and waveguide), polarization (horizontal/ vertical), orbital angular momentum (transverse spatial distribution), energy (time-frequency), or photon number (0/1 photons). Comprehensive information on photonic qubit encoding is reviewed in the references: (D. Awschalom et al., 2021; Flamini et al., 2018; Uppu et al., 2021; J. Wang et al., 2019).

Quantum information processing requires 50 photons (and even more modes) to operate within the quantum advantage regime (Zhong et al., 2020). Realization of such large-scale qubit operations in bulk has a large footprint and difficulties with respect to stabilizing. Integrated quantum photonic platforms provide compact and stable solutions, offering deterministic, high-quality single-photons as quantum information carriers. They facilitate fast, efficient, controllable, and reconfigurable circuit operations, as well as efficient on-chip detection (Uppu et al., 2021; J. Wang et al., 2019). Consequently, integration of components for different quantum operations and increasing the component density is necessary to scale up the number of qubits and photons for large-scale quantum information processing. The required components — *quantum emitters, quantum memories, coherent linear and nonlinear operators, and single photon detectors* — have been independently established on different material platforms. However, merging different operations on a single platform is highly complex, and wafer-scale fabrication is challenging. Accordingly, methods need to be developed

to interface these platforms for hybrid integration (Kim et al., 2020), which we will discuss in the final Section (1.3). Additionally, scaling-up architectures naturally brings the need for optical interconnects to initialize the multi-qubit systems for communicating with other quantum nodes. Chip-to-chip and chip-to-fiber quantum photonic interconnects will be introduced in Section 1.4.

The existing infrastructure of integrated photonics and semiconductor nanofabrication technologies has already reached a level mature enough for developing hardware for optical quantum computing. In the past decade, academic and technical expertise have been putting effort into developing key components for quantum applications. In Figure 1.1.a we see CMOS⁽¹⁾ Si chip-based module by *PSIQuantum*, a step toward realizing a fault-tolerant error corrected universal optical quantum computer (PsiQuantum, 2021; Vigliar et al., 2020). In Figure 1.1.b, we see an artistic sketch for a photonic quantum processor based on Si_3N_4 waveguides by *QuIX* (Quix, 2021). Their work is on developing a large-scale chip for quantum interference that can operate at room temperatures. Both of these platforms are often based on heralded single-photon sources to generate photons. Figure 1.1.c shows another Si_3N_4 based chip from *Xanadu*, where squeezed states of light are used as qubits (Xanadu, 2021). Finally, progress is being made on photonic qubit generation by deterministic single-photon sources, which is the main interest of this thesis. Figure 1.1.d from *Quandela* shows the integrated micropillar photon source (Quandela, 2021) and Figure 1.1.e from *Sparrow Quantum* illustrates the single-photon source based on planar technology (Sparrow, 2021). These deterministic sources represent an early stage to turn-key solutions of plug-and-play sources for quantum information processing (Chen & Segev, 2021; Uppu, Eriksen, et al., 2020).

1.1.1 Integrated deterministic sources of single-photons

Based on photonic integration technology, single-photon sources have been constructed by interacting lasers with either nonlinear optical materials or two-level systems. Nonlinear properties of optical media (integrated resonators or waveguides) allow probabilistic generation of pairs of photons by spontaneous parametric down-conversion (SPDC) and spontaneous four-wave mixing (SFWM). The probabilistically generated single-photons can be spatially or temporally multiplexed to gain deterministic properties. Conversely, two-level systems (such as atoms, ion traps, and solid-state light emitters) inherently emit only one photon upon excitation.

Probabilistic sources of single-photons are generated and operated at room temperature. Additionally, mature CMOS processes are directly applicable for photonic integration on silicon-based platforms (silica, silicon on insulator, silicon nitride). Probabilistic sources can be built on silicon-based platforms; lithium niobate is advantageous in terms of the high refractive index contrast and low-insertion loss (Elshaari et al., 2020; Meyer-Scott et al., 2020). However, boosting their deterministic ability requires active multiplexing, which comes with the cost of setup complexity and a reduced

(1) Complementary Metal–Oxide–Semiconductor

generation rate. A detailed comparison between the state-of-the-art platforms can be found in the review article from (Elshaari et al., 2020; J. Wang et al., 2019).

Truly deterministic integrated single-photon sources are desirable for scaling up qubit generation. Many technologies are being explored and engineered, each of which develops and advances solutions for overcoming certain obstacles of quantum information processing and sensing. Compared to trapped atoms and ions, solid-state emitters benefit from being based on solid-state systems, and thus, do not require an independent system to isolate and manipulate. Within solid-state emitters, III-V semiconductor QDs integrated with photonic structures have demonstrated the best performance for many figures-of-merits. These include the efficient generation of highly indistinguishable single-photons ($> 98.5\%$) (Ding et al., 2016; Somaschi et al., 2016) with near-unity purity (99.9999%) (Schweickert et al., 2018), that can preferentially emit into the desired modes ($> 98\%$) (Arcari et al., 2014) and can hold high end-to-end extraction efficiency ($> 57\%$) (Tomm et al., 2021). Additionally, short emission lifetimes of QDs (typically ~ 100 ps) allow high single-photon emission rates. These are all favorable performance properties for on-chip integrated single-photon sources. Lastly, such quantum emitters have already moved from proof-of-principle status toward practical applications. For instance, on-chip qubit operations and entangled photon-pairs generation were realized (Salter et al., 2010) and state-of-the-art solid-state qubit encoding was demonstrated (Papon et al., 2019).

To advance quantum technologies, the non-deterministic fabrication of QDs (arbitrary spatial positioning, variation in size, and the local environment), leading to alterations of positions and emission wavelengths of the on-chip QDs, has been an ongoing challenge. However, research groups have been developing methods for deterministic integration of such emitters by spectrally preselecting the emitters before building the devices (J. Liu et al., 2018; Pregolato et al., 2020b; Schnauber et al., 2018) and for pick-and-place techniques of desirable QDs (Elshaari et al., 2017; Katsumi et al., 2020; Kim et al., 2017). Nevertheless, the relatively lossy nature of the III-V platforms' components remains a challenge and requires improvement for scaling up the operations for the advanced applications of quantum information processing and distribution (Y. Wang et al., 2021). The interested reader can find application-specific single-photon source requirements in the review on solid-state single-photon emitters: Aharonovich et al., 2016.

1.2 SEMICONDUCTOR SELF-ASSEMBLED QUANTUM DOT

In this thesis, our single-photon source is a III-V semiconductor quantum dot (QD) grown by molecular beam epitaxy (MBE), specifically indium arsenide/ gallium arsenide (InAs/GaAs) (Ihn, 2010). Figure 1.2.a shows an atomic micrograph of randomly positioned islands of InAs on GaAs, formed by Stranski-Krastanov, the most commonly used self-assembly method. As shown in Figure 1.2.b, InAs is grown on a GaAs substrate. After the growth of the first few atomic layers of InAs (called the wetting layer: WL), strain accumulates in the 2D layer due to the lattice constant mismatch

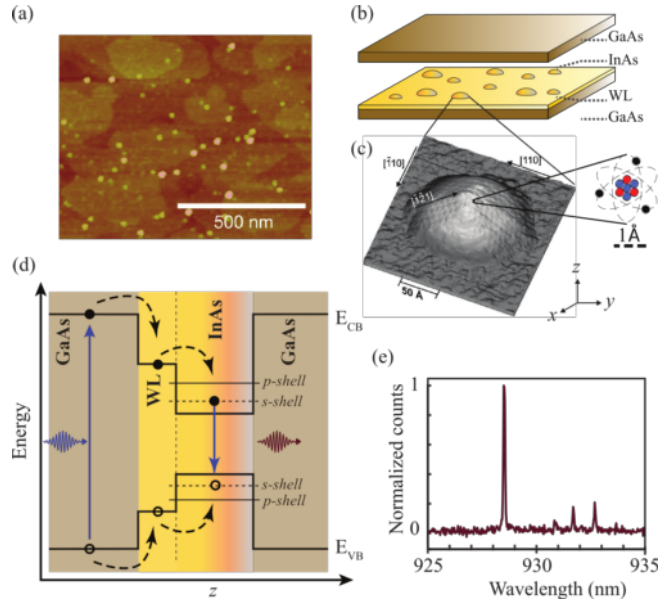


Figure 1.2: QD structural characteristics. (a) Topographical image of InAs QDs (highlighted with bright dots, representing higher regions) on GaAs matrix formed by self-assembly growth, randomly in position, size and emission wavelength. (b) Schematic of layer-by-layer structure, with grown GaAs substrate at the base, followed by the wetting layer (WL) deposition (building a quantum well), then further self-assembled InAs/GaAs QDs, and finally capped by a GaAs layer randomly grown by self-assembly method. (c) STM image of an uncapped InAs QD, with size comparison to a single atom. Adapted from (Lodahl et al., 2015). (d) Energy band diagram of InAs/GaAs QD. The discrete levels (s- and p-shells), generated by the 3D confinement are highlighted in InAs QD. The charge carriers are illustrated; an electron (solid circle) in the conduction band of InAs, and a hole (open circle) in the valence band of the InAs. (e) Typical emission spectrum from the InAs/GaAs QDs. (a) and (c) are adapted from (Lodahl et al., 2015).

between the two compounds. Consequently, the relaxation of this cumulative strain forms 3D islands of InAs QDs with random distribution and size (typically 1–10 nm lateral and 10–70 nm transverse extent). Finally, to embed the InAs islands, a capping layer of GaAs is epitaxially grown on top, resulting in a QD size on the order of 10^5 atoms (Lodahl et al., 2015) (see Fig. 1.2.c). In Chapter 3 we employed QDs with the above described layer structure. However, the QDs studied in chapter 4 are grown without a wetting layer to improve single-photon emission performance. To remove the electron wetting layer, a new method is introduced by Löbl et al., 2019, where an additional monolayer of AlAs is grown as a capping prior to the GaAs. It is important to note that self-assembled QDs have an essential advantage with their capability to integrate with photonic nanostructures, such as cavities and waveguides.

When a lower band-gap ⁽²⁾ semiconductor (e.g. InAs at 0K, $E_g = 0.42$ eV) of nanometric volume is embedded in a host semiconductor with a higher band-gap (e.g. GaAs at 0K, $E_g = 1.52$ eV), a potential trap is formed for charge carriers (electrons and holes). Consequent three-dimensional quantum confinement ⁽³⁾ of electrons and holes give rise to discretization (quantization) in the energy states of conduction and valence bands, respectively, and along the growth direction (shown in Fig. 1.2.d with s-shell and p-shell) (Hepp et al., 2019; Lodahl et al., 2015).

GaAs as a host matrix and InAs have direct band-gap configurations, where electron and hole wavefunctions (energy states) overlap in momentum space, such that valence band maxima and conduction band minima are aligned. Therefore, charge carriers moving across the band-gap do not require a change in momentum, allowing efficient optical transitions (absorption and emission). Moreover, InAs/GaAs heterostructures ⁽⁴⁾ have a type-I band alignment (also referred to as *straddling* offset), where charge carriers are confined at the band edges of the QD. This leads to strong quantum confinement for both electrons and holes, directly enhancing the intrinsic performance of the QD and light-matter interactions (C. P. Dietrich et al., 2016; Lodahl et al., 2015). Figure 1.2.d shows typical photoluminescence (PL) from a QD, where a photon is absorbed above the band gap of GaAs, the charge carriers nonradiatively relax to the lowest energy levels in the QD potential. Via exchange and Coulomb interactions, an electron in the conduction band (CB) and a hole in the valence band (VB) form a bound state referred to as an *exciton*. After an amount of time called the QD lifetime (typically ≈ 1 ns in bulk GaAs), the bound exciton radiatively recombines and a single-photon is emitted (Buckley et al., 2012; Lodahl, 2017). The spectrum in Figure 1.2.e addresses the transitions by the above band optical excitation, where the discrete nature can be observed. Accordingly, QDs as solid-state confined systems with optically active transitions are referred to as ‘artificial atoms’.

1.2.1 Performance characteristics of QD based single-photon sources

High single-photon purity, high brightness, and high indistinguishability are the key qualities of an ideal single-photon source as a building block for quantum information applications. In addition to these on-chip key performance parameters, emitted single-photons need to be efficiently out-coupled from the chip. This out-coupling efficiency is correlated with source brightness, and important for read-out scalability, and hybrid integration methods.

The solid-state environment of the QDs can be a source of decoherence, governed by lattice vibrations or defects that might effect the electrostatic environment. Excited

(2) The energy states that can not be occupied between the conduction band and valence band of semiconductor materials.

(3) Quantum confinement effects become noticeable as the system’s dimensions approach the de Broglie wavelength defined by the effective mass of the charge carriers (electrons and holes) (Patterson & Bailey, 2010)

(4) Semiconductor junction that is formed by two different semiconductor with different band-gap energy and effective mass.

state transitions tend to overlap at high temperatures, resulting in the loss of single-photon character and also phonon-induced linewidth broadening. For optimizing the single-photon emission performance, decoherence mechanisms should be controlled. To do so, QDs are operated at cryogenic temperatures, where QD linewidths can be lifetime limited, on the order of GHz. It should be also pointed out that, the thermal energy surpasses the confinement potential for many epitaxial QD systems at elevated temperatures, leading to quenching of the exciton PL (Le Ru et al., 2003). In addition, the quality of single-photon generation depends strongly on the excitation schemes (Malko et al., 2006). Also, electrical gates can be implemented around them, passivating their electrostatic environment to enhance their emission performance.

Single-photon purity is an essential measure showing how successfully the multi-photon generation probability is suppressed for each emission. The purity of a source is determined by measuring the photon statistics by photon counting experiments in a Hanbury-Brown-Twiss (HBT) setup (Brown & Twiss, 1956). Collected photon coincidences are used to evaluate the second-order correlation function at zero time delay $g^{(2)}(\tau = 0)$, which describes the probability of detecting two photons at the same time. True single-photon source purity then manifests as $g^{(2)}(\tau = 0) = 0$, i.e. there is no probability of multi-photon generation.

Brightness is another key characteristic identifying the probability of generating a single photon per excitation pulse, which is detected through the optical collection setup. The measure of brightness involves the single-photon emission efficiency into the desired mode (β -factor) and extraction efficiency at the desired port, which is commonly the first lens at the collection setup (η_{lens}).

Indistinguishability can be evaluated for separate photons that are emitted by the same emitter successively or two photons generated by separate sources to determine how well they can interfere. Perfectly indistinguishable photons are identical over all degrees of freedom (in terms of frequency, polarization, spatial and temporal modes). The degree of indistinguishability between two photons is given by the interference visibility (V) and measured with a Hong-Ou-Mandel (HOM) experiment (Hong et al., 1987). Indistinguishability measurements show how well isolated the QDs are from their environment. Also, such measurements can provide insight into the decoherence mechanisms relevant to the QD (including phonon scattering and carrier relaxation). Accordingly, indistinguishability is determined by the excitation method of the QD emitter (which will be explained in Sec. 1.2.3) and shows the best performance for resonantly excited single-photons. High-fidelity quantum operations, which are required for photonic quantum gates and quantum entanglement generation, are dependent on the generation of long strings of indistinguishable photons over large time scales.

Figure 1.3 presents four state-of-the-art approaches toward single-photon devices based on self-assembled QDs. The key figure of merits: second-order intensity correlation $g^{(2)}(\tau = 0)$, β -factor, single-photon extraction efficiency η_{lens} at the first-lens (representing how much light can propagate to the first optical component after QD is excited), single-photon indistinguishability V , and the chip-to-fiber coupling efficiency $\eta_{\text{chip-fiber}}$ denoting the fiber coupling efficiency for direct integration.

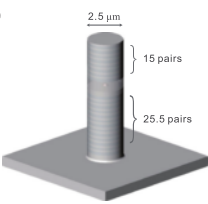
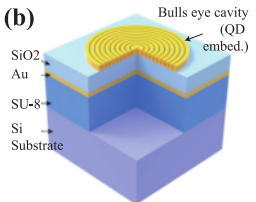
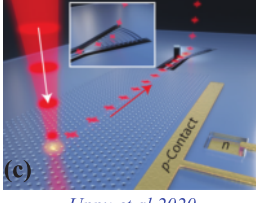
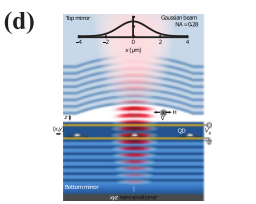
	QD SPS type	$g^2(0)$	β -factor	η_{lens}	V
<p>(a)</p>  <p><i>Ding et.al.2016</i></p>	micropillar cavity self-assembled InAs QD	0.009	N/A	66 %	98.5%
<p>(b)</p>  <p><i>Wang et.al.2019</i></p>	circular bragg grating bull's eye cavity self-assembled InGaAs QD	0.013	70%	79 %	90%
<p>(c)</p>  <p><i>Uppu et.al.2020</i></p>	photonic crystal waveguide InAs QD	0.015 ± 0.005	92 %	20 %	98.4 %
<p>(d)</p>  <p><i>Tomm et.al.2021</i></p>	Microcavity InGaAs QD	0.021	86 %	82%	97.5%

Figure 1.3: State-of-the-art single-photon sources based on self-assembled QDs, where the emitter is integrated on-chip via an (a) micropillar cavity (Ding et al., 2016), (b) circular bragg grating bull's eye cavity (H. Wang, He, Chung, Hu, Yu, Chen, Ding, Chen, Qin, Yang, et al., 2019b), (c) photonic crystal waveguide (Uppu, Pedersen, et al., 2020), (d) microcavity (Tomm et al., 2021). The quoted second-order intensity correlation $g^{(2)}(\tau = 0)$, QD single-photon emission into the desired mode β -factor, single-photon extraction efficiency η_{lens} at the first-lens, single-photon indistinguishability measured by the interference visibility V are from references.

A vertical micropillar cavity is shown in Figure 1.3.a, where the micropillar is etched from diffraction bragg grating (DBR) layers that are deposited below and above the central QD layer (Ding et al., 2016). To date, this design has achieved the best chip-to-fiber coupling efficiency with high indistinguishability and purity. Such structures are frequently preferred as single-photon sources (Ates, Ulrich, et al., 2009; Snijders et al., 2016; Somaschi et al., 2016; Unsleber et al., 2016). Alternatively circular bragg grating bulls' eye cavity is formed around QD, which is formed by ring structures in Figure 1.3.b (H. Wang, He, Chung, Hu, Yu, Chen, Ding, Chen, Qin, Yang, et al., 2019b). The rings are etched in a semiconductor membrane on silicon. Such structures are advantageous for high single-photon generation and extraction efficiencies (J. Liu et al., 2019). A photonic crystal waveguides with embedded QDs is illustrated in Figure 1.3.c (Uppu, Pedersen, et al., 2020). Photonic crystal waveguides with embedded QDs shows excellent β -factor, with high purity and indistinguishability values (Arcari et al., 2014). Finally, high efficiencies are achieved with a microcavity that is sketched in Figure 1.3.d (Tomm et al., 2021). Here, the microcavity is formed by a bottom DBR mirror similar to the micropillar, where there is no etching step. A micro-machined fused silica surface is then placed as a top mirror, increasing the emission into a Gaussian out-of-plane mode. Structures in Fig. 1.3.c:d include charge control in their heterostructures.

In the following, we present a brief overview of the fundamentals of single-photon emission from III-V QDs. A more thorough examination of excited states and single-photon emission in QDs can be found in the following review (C. P. Dietrich et al., 2016; Hepp et al., 2019; Lodahl et al., 2015; Shields, 2010).

1.2.2 Optical properties of quantum dots

Quantum dots as two-level systems

In quantum optics experiments, the complex energy levels of a homogeneous solid-state semiconductor system can be estimated by the two-band effective mass approximation,⁽⁵⁾ where only a single conduction band and single valence band are taken into account. Energy levels of the self-assembled QDs are determined by quantum confinement and interactions between the charge carriers (Coulomb and exchange interactions), which are mainly controlled by the growth of the QDs. As shown in Figure 1.2.d, upon optical excitation, an electron in the conduction band and hole in the valence band form an exciton. The creation and recombination of the exciton leads to optical transitions.

This exciton may recombine radiatively (optically) and non-radiatively, where these optical transitions are defined via selection rules. To define the quantum states of electrons (or holes) confined in a heterostructure, we use the envelope equation formalism

$$\Psi_m(r) \simeq F_m(r)u_{m0}(r). \quad (1.1)$$

⁽⁵⁾ The motion of the electron (hole) wavefunction in the conduction band (valence band) in the periodic potential is defined by the band-edge effective mass.

Here, the wave function Ψ_m of an electron (or hole) at position r and band m (can be conduction band c or valence band v) is calculated as a product of the envelope function $F_m(r)$ describing the confining potential and the Bloch function $u_{m0}(r)$ due to the lattice periodicity at $k = 0$ of the band structure. It should be noted that here we could introduce the spin components to the wave function, but they are neglected here.

Light-matter coupling between the quantized electric field of single-mode radiation and the QD is described with the dipole approximation ⁽⁶⁾, using the interaction Hamiltonian

$$\hat{H} = -\hat{d} \cdot \hat{E}. \quad (1.2)$$

Here $\hat{d} = q\hat{r}$ is the dipole moment operator (q is the elementary charge and \hat{r} position operator) and \hat{E} is the electric field operator (Lodahl et al., 2015).

Weisskopf and Wigner use a complete quantum treatment of light and matter to describe the spontaneous emission process (Weisskopf & Wigner, 1997). The electric field-dipole interaction is described by the Jaynes-Cummings Hamiltonian given by (Gerry & Knight, 2005)

$$\hat{H}_{\text{int}}(\mathbf{r}, t) = -\frac{q}{m_0} \hat{\mathbf{p}} \cdot \hat{\mathbf{A}}(\mathbf{r}, t), \quad (1.3)$$

where $\hat{\mathbf{p}}$ is the momentum operator of the QD state and $\hat{\mathbf{A}}$ is the vector potential operator of the quantized electromagnetic field, given with the Coulomb's representation (gauge). ⁽⁷⁾

The optical transition probability between the different levels of the unperturbed Hamiltonian can be evaluated by Fermi's golden rule (Novotny & Hecht, 2012). Thus, the radiative decay rate of the spontaneous emission is calculated as

$$\gamma_{\text{rad}} = \frac{2\pi}{\hbar} \sum_f |\langle f | \hat{H}_{\text{int}} | i \rangle|^2 \delta(\omega_f - \omega_i), \quad (1.4)$$

between the initial state $|i\rangle$ and set of final states $|f\rangle$ of the photon and QD system. The delta function $\delta(\omega_f - \omega_i)$ ensures the energy is conserved in the transition by fixing it such that the energy difference between two states corresponds to the frequency of the emitted photon via the decay process.

Consider spontaneous emission. The initial state of the exciton trapped in the QD $|i\rangle = |e\rangle |0\rangle$ has one exciton in the QD, i.e., in the excited state $|e\rangle$ and no photon in the field $|0\rangle$. The final state has no exciton in the QD, i.e., at the ground state, $|g\rangle$ and the photon is emitted into a certain mode indexed with μ . As such, $|f_\mu\rangle = |g\rangle |1_\mu\rangle$, where $\mu = (\mathbf{k}, s)$ has the wave vector \mathbf{k} and polarization s information. When we use the interaction Hamiltonian in Eq. 1.3 to derive the Eq. 1.4, the radiative decay rate of an

(6) QDs emit at wavelengths in the order of hundreds of nanometers, while having a size on the order of tens of nanometers, their interaction with the electromagnetic field can be described by the dipole approximation.

(7) The optical transition energies of the electron-hole pairs are considered individually.

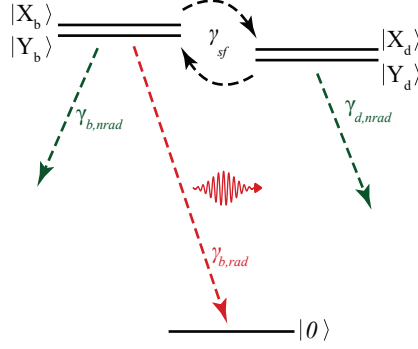


Figure 1.4: Schematic representation of the three-level scheme of a neutral exciton. Emitter ground state $|0\rangle$ is empty with no excitation. System can be populated by bright excitons ($|X_b\rangle$, $|Y_b\rangle$) that decay radiatively to $|0\rangle$ or dark excitons ($|X_d\rangle$ and $|Y_d\rangle$) that decay nonradiatively to $|0\rangle$, with decay rates γ_{rad} , $\gamma_{\text{n,rad}}$ respectively. Bright and dark states can couple via spin-flip process with rate γ_{sf} .

exciton can be rewritten as (Novotny & Hecht, 2012)

$$\gamma_{\text{rad}}(\mathbf{r}_0, \omega_0, \hat{\mathbf{e}}_d) = \frac{\pi q^2}{\hbar m_0^2 \epsilon_0} |\langle g | \hat{\mathbf{p}} | e \rangle|^2 \frac{\rho_{\text{LDOS}}(\mathbf{r}_0, \omega_0, \hat{\mathbf{e}}_d)}{\omega_0}. \quad (1.5)$$

Eq. 1.5 defines the spontaneous emission rate as a function of the position \mathbf{r}_0 , the emission frequency ω_0 and direction of the dipole emitter $\hat{\mathbf{e}}_d$. The dipole transition matrix element $p_{ge} = \langle g | \hat{\mathbf{p}} | e \rangle$ is based on a set of selection rules. Since p_{ge} is based on the overlap of ground state and excited state exciton wavefunction in the QD, it determines the optical transition strength and the QD oscillator strength (Lodahl et al., 2015). A large oscillator strength is essential for enhancing the light-matter interaction, which in turn increases the generation rate of the single-photons. The term $\rho_{\text{LDOS}}(\mathbf{r}_0, \omega_0, \hat{\mathbf{e}}_d)$ is the local density of optical states (LDOS), which sets the number of available optical modes per unit energy and volume for the radiating dipole $\hat{\mathbf{e}}_d$ at a certain frequency ω_0 and position \mathbf{r}_0 (Novotny & Hecht, 2012). The radiative decay rate also defines the radiative lifetime of the QD transition $T_1 = \gamma_{\text{rad}}^{-1}$. Typical lifetimes of the InAs/GaAs QDs are ~ 1 ns.

Decay dynamics

QDs can have many excitonic transitions (Lodahl et al., 2015) (see Fig. 1.5). The band structure can be tuned by an electric field to control the hosted charge carriers. With that, optical excitations (energy and polarization) can be fixed to target specific transitions (Dalgarno et al., 2008; Seidl et al., 2005). It is important to note that QDs can be described in terms of two-level systems (with excited and ground states) and can be treated by Eq. 1.5, even if considering multiple excitonic states and more complex optical transitions. Specifically, in this thesis we focus on the neutral exciton X^0 transition consisting of a single electron and hole pair.

Figure 1.4 shows typical transitions from a neutral exciton X^0 of a QD embedded in a homogeneous photonic media. X^0 has four possible states. Per the selection rules, two states decay radiatively based on their dipole-allowed transitions and are therefore referred to as *bright excitons*. The other two states have dipole-forbidden transitions that yield non-radiative recombination, thus they are referred to as *dark excitons*. The four-degenerate states are split by the electron-hole exchange interactions into bright ($|X_b\rangle$ and $|Y_b\rangle$) and dark energy states ($|X_d\rangle$ and $|Y_d\rangle$). The degeneracy of the two bright excitons (and two dark excitons) is lifted by the anisotropic in-plane confinement potential of the QD. Consequently, it leads to a separation in orthogonal linear polarizations of X- and Y- dipoles.

The aspect ratio of the QD introduces fine structure splitting to the orthogonally polarized dipoles. Both bright excitons can decay radiatively with rate γ_{rad} to the ground state $|0\rangle$, leading to linear polarizations. Also, bright and dark excitons can decay nonradiatively to the valence band via thermal relaxation of the charge with rate γ_{nrad} . Also, a spin-flip process can occur between the bright and dark excitons before they decay with rate γ_{sf} . This is mainly a phonon-mediated process and has been measured to be slower than the radiative and nonradiative processes. The coupling from the bright exciton to dark exciton states occurs via a spin-flip of an electron without any emission. A photon can be emitted upon a potential second spin-flip process to the bright exciton state, so-called blinking. The dynamics of this process are studied in detail in the Ref. (Johansen et al., 2010).

The probability of recombination processes resulting in single-photon emission upon optical excitation defines the quantum efficiency of the emitter, which is an important figure of merit for photonic applications, quantified by

$$QE = \frac{\gamma_{\text{b,rad}}}{\gamma_{\text{b,rad}} + \gamma_{\text{b,nrad}}}. \quad (1.6)$$

As the decay rates depend on the growth of QDs and emitter-medium interaction, QE values can vary for individual QDs on the same structure. A near-unity QE is required for many applications (Lodahl et al., 2015).

1.2.3 Excitation schemes of QDs

Optical excitation methods for single-photon generation

Single-photons can be generated via different excitation channels preparing excitons in a QD. Typically by focusing a laser beam vertically, on top of the QD, or recently by coupling the excitation laser to the propagating waveguide mode and exciting the QD, the emitter can be optically excited. An excitation laser, operating in continuous wave or pulsed modes, can be tuned to specific frequencies to match different energy bands of the QDs. The resulting single-photon emission via different channels is usually addressed by (μ -) PL spectroscopy.

A QD can be excited using a laser energy above its bandgap, as shown in Figure 1.5.a. Excitons are generated in the host semiconductor, a fraction of which are first captured

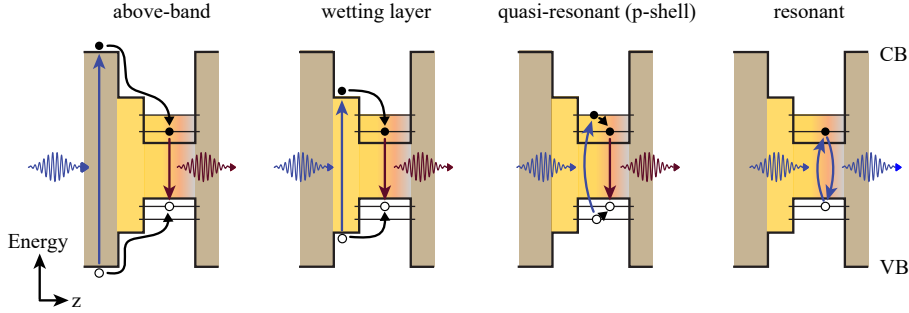


Figure 1.5: Excitation channels in QD for single-photon generation. (a) Charge carriers are excited above the band-gap of GaAs. Subsequently, the QD relaxes to the ground state. (b) Charge carriers are excited directly in the wetting layer. (c) Quasi-resonant excitation of excitons by exciting through a higher energy resonance of the QD (p-shell). (d) Resonance fluorescence when the laser frequency is tuned to the QD ground state frequency.

by the wetting layer, then relax into the excited states of the QD, and subsequently decay into the ground state via phonon-assisted relaxation (picosecond timescale), forming excitonic configurations. The PL spectrum shows several exciton lines at different frequencies, which need to be filtered to give a single photon. Above-band excitation is the most straightforward excitation scheme since it does not require a specific wavelength, and the high-power laser can be distinguished easily from the low-power single-photon signal on account of its wavelength. As another option, continuum states of the 2D wetting layer can be excited (see Figure 1.5.b), and the QD electron-hole pairs can be captured.

Quasi-resonant excitation involves absorbing a laser photon resonant with the higher excited state; p-shell as it is shown in Figure 1.5.c. Charge carriers first relax to the first excited state (s-shell) and decay to the ground state. Typically the relaxation to the s-shell of the ground state occurs rapidly with a typical lifetime of ~ 10 ps (while exciton lifetime is ~ 1 ns), in turn with a broader linewidth. Since the exciton bound is formed in the QD, dephasing mechanisms can be highly minimized comparing with the above-band excitation. As a result, it can lead to a fast generation of indistinguishable single-photons. Besides, since the multiple photon emission can be avoided, it results in higher purity single-photon generation.

Resonant excitation requires the laser frequency to be tuned to the transition connecting two s-shells in the ground and excited states, where there is no relaxation process needed to emit a single photon. Since no additional charge is created in this scheme, dephasing is minimized, and indistinguishability is maximized. However, this technique is highly challenging since it requires strong suppression of the laser with a frequency exactly matching with the QD. A broader overview of the resonant excitation scheme will be provided in Chapter 4.

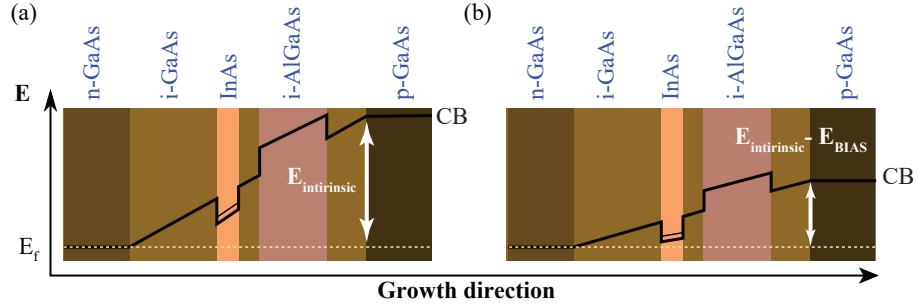


Figure 1.6: Deterministic tuning of the energy states and charge carriers in the QD. (a) QD membrane with p-i-n diode structure, where the doped layers introduce an intrinsic constant electric $E_{intrinsic}$ to shift the conduction band. (b) A bias field E_{bias} is applied to tune the conduction band slope.

Electrical tuning of QD emission

The electronic properties of each QD are greatly influenced by its semiconductor surroundings. The QD's charge carriers interact with uncontrolled elements of the environment, such as trapped charges or material strain. These uncontrolled interaction mechanisms impact optical transitions by reducing the QD states' coherence and shifting the emission wavelength (spectrum wandering). Besides, coupling to the modes of the host causes the phase information of the QD state to be lost, which is the so-called dephasing process. Here, we briefly introduce a deterministic method for manipulating QD states, where an external, constant electric field is applied to control the electron flow and uncontrolled charge noise on electrically contacted samples.

Figure 1.6.a shows an InAs QD grown in the intrinsic (i-) region of the p-i-n diode. The p- (positive) and n- (negative) doped GaAs of the heterostructure allow applying an electric field. Besides, based on the given electric potential difference between the p- and n- layers, it defines the constant intrinsic field to the InAs QD layer. Additionally, an i-AlGaAs layer is introduced as a barrier for the electric current flow in the InAs. The strength of the field determines the relative positions (slope steepness) of the electronic bands of the QD (CB and VB).

Applying an external direct current (DC) electric field (F) along the growth direction introduces an additional potential (V_F) and tunes the electron-hole bound energies to higher or lower energy states (Figure 1.6.b), following $V_F = -qF \cdot r$. By tuning the tunnel barrier, electron tunneling into the QD can be allowed or prevented. The heterostructure growth and electrical contact fabrication provide fine-tuning of the electric field of the individual QDs that can enable the manipulation of single-charge carriers. The electrons (holes) can be pulled towards the anode (cathode) or conversely according to the polarity of the applied electric field, which reconfigures the exciton transition energies and recombination rates.

Electrical contacts are fabricated on the photonic circuitry, and by applying the bias field across the QD layers, exciton transition energies are tuned. The voltage-dependent

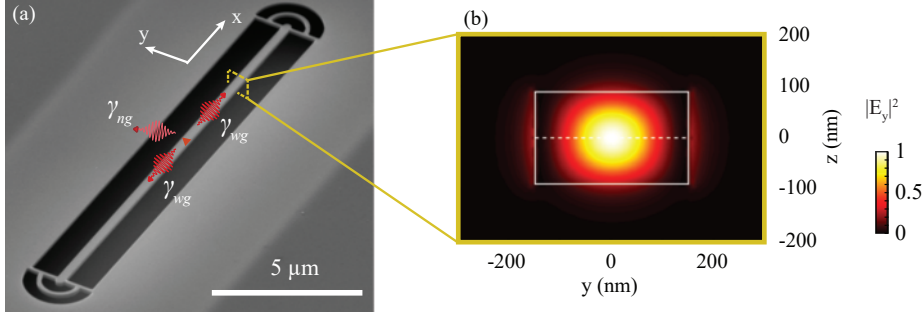


Figure 1.7: Suspended GaAs nanobeam waveguides. (a) Tilted-view SEM image of a nanobeam waveguide bridging shallowed etched grating couplers. (b) Two-dimensional finite-element-method (FEM) calculation of a single-mode waveguide. The single guided mode is confined in the nanobeam with 300 nm width and 160 nm thickness, confirms the main component of the fundamental mode (TE_{00}) in y -direction of the electric field.

change in the single-photon emission wavelength is known as the quantum-confined Stark effect. By applying a bias field to bring charge carriers in the n - and p - layers to be in the same resonance with the QD energy levels, resonant tunneling can be switched on and off for a specific QD. As a consequence, in resonance fluorescence measurements, back-ground free single-photon detection (excitation laser suppression) can be possible, which is introduced widely in Chapter 4 (Somaschi et al., 2016; Uppu, Pedersen, et al., 2020; H. Wang, He, Chung, Hu, Yu, Chen, Ding, Chen, Qin, Yang, et al., 2019a).

1.2.4 Coupling between QD emission and nanophotonic waveguides

In homogeneous media, spontaneous emission from a two-level emitter is dependent on the LDOS, as it was described by the equation of radiative decay rate of a dipole emitter (eq. 1.5). The LDOS $\rho_{LDOS}(\mathbf{r}_0, \omega_0, \hat{\mathbf{e}}_d)$ describes the density of the available optical modes, that a QD dipole radiatively decay into per certain frequency and unit volume. It is defined as (Lodahl et al., 2015)

$$\rho_{LDOS}(\mathbf{r}_0, \omega_0, \hat{\mathbf{e}}_d) = \sum_{\mathbf{k}} |\hat{\mathbf{e}}_d \cdot \mathbf{u}_{\mathbf{k}}^*(\mathbf{r}_0)|^2 \delta(\omega_0 - \omega_{\mathbf{k}}), \quad (1.7)$$

where $\mathbf{u}_{\mathbf{k}}(\mathbf{r})$ is normalized mode functions to which the electric field is coupled. Accordingly, by modifying the nanophotonic environment of the QD emitter, decay dynamics can be controlled. Several photonic nanostructures have been demonstrated (Lodahl et al., 2015), and some of them can be seen in Figure 1.3. In this work, we will focus on the QD embedded in nanobeam waveguides (see Fig. 1.7).

By controlling the QD emitter position in an engineered nanobeam waveguide (e.g. see Fig. 1.7), the coupling efficiency of the emitted single photon into the waveguide mode can be enhanced. The figure-of-merit, in this case, is the β -factor, which is defined

as the ratio between the radiative decay rate of the emitter into the waveguide mode γ_{wg} and the total decay rate of the emitter into all the available modes γ_{tot} (Javadi et al., 2018)

$$\beta = \frac{\gamma_{\text{wg}}}{\gamma_{\text{tot}}} = \frac{\gamma_{\text{wg}}}{\gamma_{\text{wg}} + \gamma_{\text{ng}} + \gamma_{\text{nrad}}}, \quad (1.8)$$

where γ_{ng} is the decay rate of the emitter into non-guided (leaky) modes, and γ_{nrad} accounts for non-radiative recombination processes in the QD (see Fig. 1.7.a). The QD dipole ($\hat{\mathbf{e}}_{\text{d}}$) is oriented in-plane, where the emission couples strictly to transverse electric field (TE) modes. Strong emission into the TE modes is a significant factor for integrated quantum photonic circuits, leading emitter to have a deterministic coupling into the engineered nanophotonic waveguides (TE modes).

Figure 1.7.a shows a suspended GaAs nanobeam waveguide, where the refractive index contrast between air and the suspended GaAs nanobeam waveguide is large ($n_{\text{Air}} = 1$, $n_{\text{GaAs}} \approx 3.47$ at 930 nm at 1.6K). Therefore, the out-of-plane radiation is suppressed by the total internal reflection. Accordingly, γ_{ng} will be strongly reduced. Figure 1.7.b shows the main electric field component of the fundamental mode in y -direction; TE_{00} (perpendicular to the propagation direction of the electric field; \hat{x}). The electric mode profile is simulated by FEM. When the QD emitter, whose dipole is oriented along the y -axis, is positioned in nanobeam center (300 nm wide) and the middle of the slab (160 nm thick), single-photon coupling into the waveguide mode is calculated to be $\beta \sim 90\%$.

The β -factor can be further improved by enhancing the decay of the emitter into the waveguide mode of interest by QDs precisely located in photonic crystal waveguides with engineered band-gap. Experimentally, near-unity coupling of quantum dots to the desired mode is achieved with $\beta \geq 98.4\%$ (Arcari et al., 2014).

1.3 HYBRID INTEGRATION OF INTEGRATED QUANTUM PHOTONICS

Advanced quantum operations for quantum information processing are influenced by the capability of the (photonic integrated circuit) PIC technologies. Great progress has been shown in building the individual hardware required for the development of quantum photonic platforms: **i.** *high-performance, deterministic sources generating high quality single photons* that can be spectrally fine-tuned and can be triggered resonantly, **ii.** fast and low-loss integrated circuits composed of *passive* (optical routing, beam splitters, optical filters, optical delays, passive interferometers) and *active* (photonic switches/ modulators, frequency converters, reconfigurable circuits) devices, **iii.** fast and highly-efficient *single-photon detectors*, **iv.** integrated fiber coupling elements and optical interfaces. (Elshaari et al., 2020; Kim et al., 2020; Kim et al., 2017; Rodt & Reitzenstein, 2021; Uppu et al., 2021; J. Wang et al., 2019). However, integrating these key units on the same quantum device is highly challenging, as each of these hardware's material platforms has different requirements. Therefore, hybrid integration methods are highly demanded to bring different modules together and fully connect different systems.

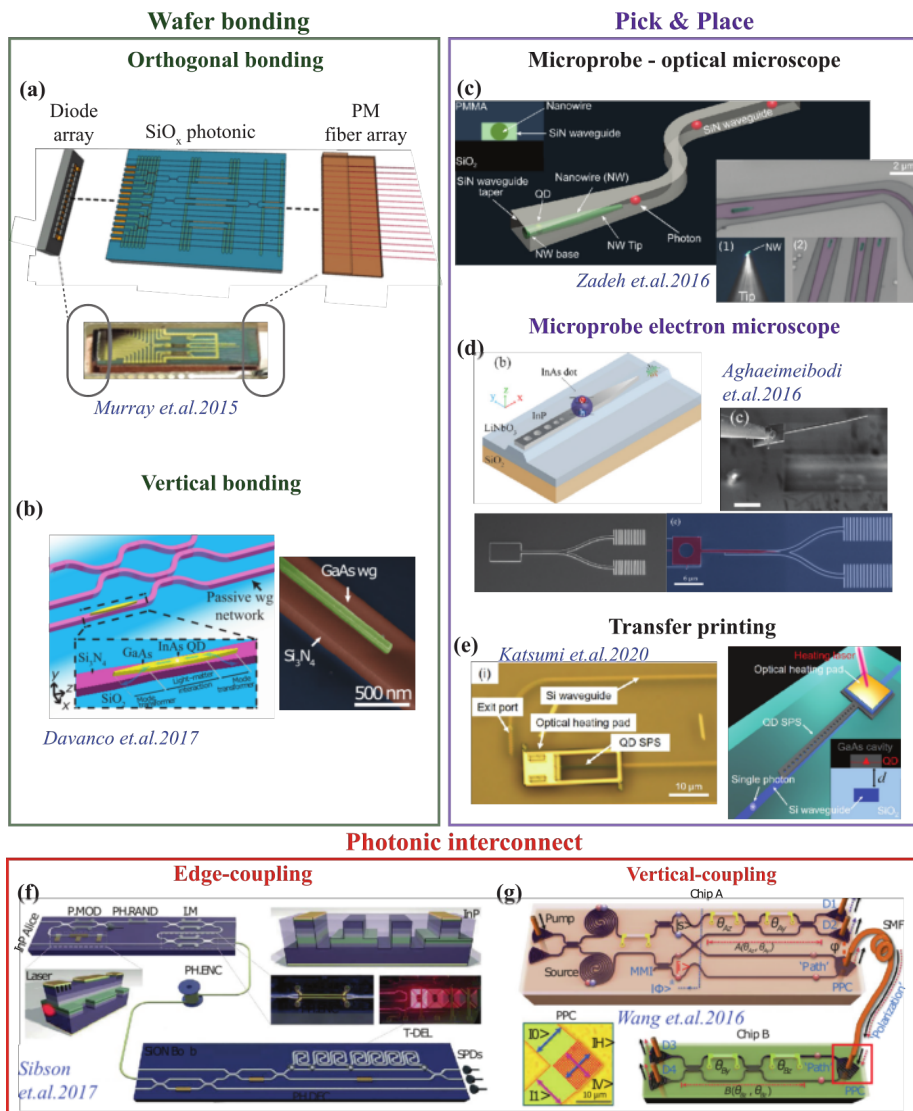


Figure 1.8: Hybrid integration techniques for scalable quantum devices. (a) III-V QD source chip is interfaced with reconfigurable Si_3N_4 photonic circuit, which is then coupled to a fiber array (Murray et al., 2015). (b) QD source embedded GaAs waveguide is vertically bonded on Si_3N_4 (Davanco et al., 2017). (c) III-V QD nanowire source is transferred on Si-based circuitry via pick-and-place method (Zadeh et al., 2016). (d) InAs/InP QD sources is integrated on Si photonic waveguide via pick-and-place technique (Aghaeimeibodi et al., 2018). (e) InAs/GaAs QD-based single-photon source waveguide is transfer printed Si CMOS chip (Katsumi et al., 2020). (f) Hybrid integration based on fiber optical coupling between the InP transmitter chip and SiO_xN_y receiver chip for quantum key distribution (Sibson et al., 2017). (g) Between two Si quantum chips communication is provided over long distance through optical fiber for entanglement distribution (J. Wang et al., 2016).

We have introduced the self-assembled III-V semiconductor QDs as an ideal source of deterministic single photons, based on their high purity, indistinguishability, brightness, and generation rate (see Sec. 1.2). On the one hand, there are inherent challenges for having sources and on-chip devices/circuits together. The inherent random spatial position of the QDs is challenging for building circuits around them and the high loss on III-V material (linear propagation loss 2 dB/cm (Smit et al., 2014)) limits the upscaling of devices.

Most of the solid-state emitters operate at short wavelengths of the visible and near-infrared regime (below 1.1 μm). Specifically, InAs/GaAs QD sources are transparent at around 930 nm. Because of their operation wavelength being lower than telecom wavelengths, they require frequency conversion to be fully adapted to the fiber networks. However, indium arsenide/ indium phosphide (InAs/InP) QDs operate at telecom wavelength as well as defect (color) centers in silicon carbide and gallium nitride microcrystals.

A requirement for using single photons as carrier of quantum information is the ability to manipulate their states and perform operations. By employing active and passive optical components, the processor hardware can be built. Integrated waveguide platforms (e.g. silicon-on-insulator, silica-on-insulator, silicon nitride Si_3N_4 , lithium niobate: LiNbO_3 , aluminum nitride: AlN) have been widely investigated for decades. In particular, Si-based photonics have well-developed fabrication methods, and their fabrication is compatible with integrating CMOS electronics (integration with millions of transistors). Furthermore, they are available for scaling up the component density based on the achieved low-optical propagation losses (Si; 2.7 dB/m (Biberman et al., 2012), SiO_2 ; 0.1 dB/cm (Fukuda et al., 2004), Si_3N_4 ; 0.1 dB/m (Bauters et al., 2011)). Si-based optics also offers a large wavelength window from 1.1 μm to $\sim 7 \mu\text{m}$, while Si_3N_4 is transparent above 400 nm. Recently, a quantum photonic reconfigurable circuitry with more than 550 optical components was demonstrated on a silicon platform (J. Wang et al., 2018). State-of-the-art photonic integrated circuitry on silicon-on-insulator scaled up the density of components to 4096 (for 64x64 phased array) (Sun et al., 2013), confirming the potential of the platform for realizing advanced quantum operations. On the one hand, in terms of electro-optic and piezoelectric properties, lithium niobate and aluminum nitride present great advantages based on the Pockels effect ⁽⁸⁾. Pockel effects, which enables ultrafast optical modulation (LN on insulator voltage-length product 2.8 V cm (C. Wang et al., 2018)) and low insertion loss (LN on insulator at telecom and visible wavelengths 2.7 dB/m (Zhang et al., 2017)) can be achieved. Besides, these material platforms have a larger transparency bandwidth (350– 4500 nm) (Kim et al., 2020).

Finally, single-photons need to be read out efficiently and fast. In terms of on-chip detection methods, superconducting nanowire single-photon detectors (SNSPDs) are the most promising in terms of very high efficiency and high-speed operation, low time-jitter, low dark-count rates in a large bandwidth (from 400 nm up to telecom

(8) An electro-optic effect can be seen on non-centrosymmetric materials, where the refractive index is modified linearly upon the induced electric field.

wavelengths). Integrated SNSPDs can be formed on various materials such as Si, Si₃N₄, GaAs, LiNbO₃, AlN, and diamond.

These hardware platforms have their own challenges and limitations for merging all required functionalities on a single monolithic chip. Therefore, methods need to be developed to bridge different technologies and form an assembly of hybrid structures. Integrating different quantum systems can allow linking single-photon emitters, coherent linear and nonlinear operations, memories, and single-photon detectors on a single platform. However, since each material has different operation bandwidth, wavelengths of emitted photons need to be efficiently converted to the telecom wavelength. Also, refractive indices and processing requirements are platform-specific. Thus, hybrid integration of quantum devices is still challenging. Various methods have been studied for interfacing different monolithic systems, such as wafer bonding, pick-and-place techniques (transfer printing and microprobes), and on-chip fiber coupling. Photonic wire bonding technique has also been demonstrated for integrating III – V InP lasers with silicon phosphide (SiP), SiO₂, Si₃N₄, and can be another potential solution for hybrid integration of photonic quantum circuits (Billah et al., 2018; P.-I. Dietrich et al., 2018).

Figure 1.8 illustrates different hybrid quantum photonic integration techniques, combining quantum light sources with the photonic integrated operational circuits and single-photon detectors. Here, hybrid integration is divided into three categories: wafer bonding, pick-and-place method, and photonic interconnects. Another method for integrating quantum sources on high-crystalline bulk is direct heterogeneous growth. Such that III-V QDs can be monolithically grown on Si platform (Heidelberger & Fitzgerald, 2018; Kim et al., 2020). However, ensuring an efficient coupling of single-photon emission and the desired mode of the photonic circuit is challenging and has a poor efficiency. Materials, hosting the single-photon sources (e.g. III – V materials), detectors (e.g. SiN_x), and photonic circuitries (e.g. Si) have incompatible properties, such as lattice dimensions, thermal expansion coefficients, and surface polarity. Accordingly, maintaining the material properties during the growth is difficult (Pan et al., 2019). Therefore, it is a naturally challenging approach.

Wafer-bonding can interface different material platforms without sacrificing material properties. In Figure 1.8.a an orthogonal bonding method is experimentally demonstrated. A diode array with individually controllable III – V QDs is butt-coupled to a reconfigurable waveguide circuit on SiO_xN_y, which is then connected to the polarization-maintaining (PM) fiber array. Fiber array is used to in-couple the excitation laser and out-couple the QD emission (Murray et al., 2015). Another wafer-to-wafer bonding approach is illustrated in Figure 1.8.b, where the InAs QD embedded GaAs waveguide (photonic crystal waveguide in the bottom figure) is bonded on Si₃N₄. The two-wafer layer is bonded via the low-temperature, oxygen plasma-activated procedure, and devices are formed by e-beam lithography (Davanco et al., 2017). The challenge with wafer bonding pertains to the random emitter position and emission wavelength. However, in-situ e-beam lithography technique and emitter-specific wavelength-tuning methods have been demonstrated to improve deterministic fabrication (Schnauber et al., 2018; Schnauber et al., 2019).

The pick-and-place technique can introduce control over the emitters by picking the pre-characterized quantum sources and placing them on the photonic integrated circuits. With this method, not only the quantum emitters but the detectors can be integrated on the same platform (Najafi et al., 2015). Figure 1.8.c shows a $III - V$ QD nanowire single-photon source integrated into the Si_3N_4 waveguide, with a microprobe (tungsten tip) under an optical microscope. Here the detachment of the source from its growth sample is due to the van der Waals forces (Zadeh et al., 2016). Besides, the encapsulation of the emitter in the Si_3N_4 waveguide is provided by the e-beam lithography. A similar technique can improve alignment accuracy in an electron microscope system, where there is even room for re-alignment. Figure 1.8.d shows an example for this approach, where an InAs QD embedded in an InP nanobeam is transferred on a LiNbO_3 waveguide (Aghaeimeibodi et al., 2018). Also, in Figure 1.8.e by utilizing a rubber stamp, the pre-characterized InAs QD source in GaAs PhC cavity is detached from the GaAs and transferred to the CMOS-processed Si circuit via optical microscope real-time alignment (Katsumi et al., 2020).

Ideally, the most practical approach is building photonic interconnects between the quantum hardware. Through integrated couplers and fiber links, single photons can be transmitted from the source chip to the quantum operation chip and the integrated detection device. Figure 1.8.f shows the integration of two separate devices by fiber coupling (Sibson et al., 2017). This hybrid integrated system experimentally realizes chip-to-chip quantum key distribution (QKD), where the two different material platforms: the transmitter (InP platform) and receiver chips (silicon oxynitride; SiO_xN_y platform) are connected via in-plane fiber coupling and edge-couplers. Chip-to-chip entanglement distribution and quantum teleportation are demonstrated in Figure 1.8.g by transmitting the generated qubit from Chip A to Chip B (both based on Si-photonics) via vertical couplers, two-dimensional grating couplers, and fiber links (J. Wang et al., 2016). On the other hand, photonic wire bonding technology has already integrated multiple monolithic photonic chips (Billah et al., 2018; P.-I. Dietrich et al., 2018; Lindenmann et al., 2015) and holds great potential for building quantum photonic systems.

In this thesis, the main aim is to develop on-chip components for achieving a scalable quantum platform. Chapter 3 highlights the importance of quantum photonic interconnects for transferring quantum information between one system to another.

1.4 SINGLE-PHOTON OUT-COUPLEDERS

Low-loss optical couplers are mandatory for out-coupling quantum information from the single-photon sources to external single-photon detectors and transmitting flying qubits in quantum networks. High efficiency and, in turn, low-loss operations are crucial figure-of-merits for quantum applications. This is a result of the single-photon count rate, a crucial figure of merit, being a direct product of (1) single-photon emission, (2) coupling to the mode of interest, and (3) *all* optical transmission efficiencies prior to even detection. A quantum state can not be amplified as a consequence of the unitary nature of quantum transformation. This is called the ‘no-cloning theorem,’ which

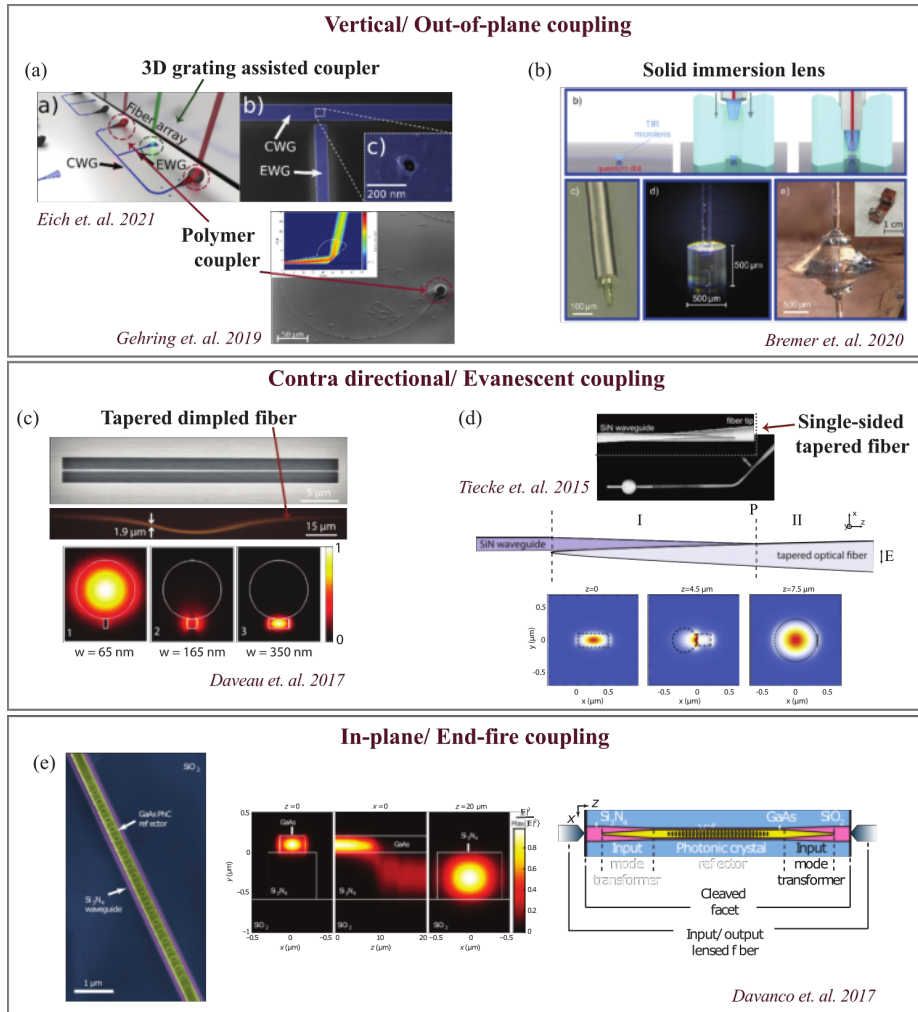


Figure 1.9: State-of-the-art optical out-coupling strategies. **Vertical/ out-of-plane coupling method** is shown in (a) between 3D grating assisted coupler and 3D polymer coupler to fiber arrays (Eich et al., 2021), in (b) by immersion lens to a lensed fiber (Bremer et al., 2020). **Contra-directional/ evanescent coupling method** is shown in (c) between a tapered waveguide and tapered dimpled fiber (Daveau et al., 2017) and in (d) between a tapered waveguide and single-sided tapered fiber (Tiecke et al., 2015). **In-plane/ end-fire coupling method** is shown in (e) by end-fire coupling between the integrated waveguide and lensed fiber (Davanco et al., 2017).

mandates that an unknown quantum state can not be perfectly and deterministically copied. Accordingly, it is critical to engineer on-chip coupling methods between the quantum circuits and fiber optics, which are efficient, robust, scalable, large-bandwidth, and cryogenic compatible.

The chip-to-fiber coupling has several challenges, which are unique to deterministic semiconductor single-photon sources. Particularly, in the case of III-V, QD sources require cryogenic temperatures (below 10 K) to suppress phonon mediated decoherence and the phonon noise influencing QDs. *The single-photon source coupler needs to be cryo-compatible.* Here, the challenge is related to the coupler's resistance to thermal stress during the cool-down and warm-up of the cryostat. Accordingly, the integrated chip-to-fiber coupling mechanism needs to be robust, reliable, and repeatable.

Realization of unity coupling efficiency between the on-chip waveguide and fiber requires complete power transfer between the two waveguides. This depends on **spatial mode-size matching** and **high alignment accuracy**. Coupling efficiency is the ratio of the guided optical power at the output and input of the coupling mechanism. It is quantified by the mode overlap between the integrated coupler and fiber. The polarization state of the out-coupled photons needs to be conserved, which requires polarization maintaining, single-mode fibers (SMF). These fibers have typical core diameters between 4 μm to 8 μm (at wavelengths 830 nm to 1064 nm), which are unfavorable for optimizing both mode-size overlap and alignment. Regarding mode size matching, the fiber core diameter is larger than the single-mode on-chip planar waveguides in deterministic platforms. For instance, the single-mode suspended GaAs waveguide is typically designed with a width of 300 nm and thickness of 160 nm at QD emission wavelength (930 nm). To overcome size mismatch, sophisticated coupler designs are required. As for the alignment, high-precision piezo-positioners in cryostats are required for fiber scanning the single-photon emission.

For scaling up the read-out operation, multiple out-couplers need to be placed, which rely on couplers' to have a small footprint. The large refractive index contrast between integrated waveguides (terminated by the couplers) and their cladding environment (air or cladding materials) leads to reduced waveguide dimensions and bending radiuses, thus allowing high component density on-chip. Last but not least, for linking different platforms with varying refractive indices by optical interconnects, large spectral bandwidth operation is another essential figure-of-merit.

State-of-the-art coupling techniques between integrated photonic devices and optical fibers are illustrated in Figure 1.9, which are listed under three categories: **i.** vertical (out-of-plane) coupling, **ii.** contra-directional (evanescent) coupling, **iii.** in-plane (end-fire) coupling. Each of these approaches operate based on different physical principles and their implementation requires various nanofabrication techniques.

Vertical coupling method allows access to the integrated circuit through the surface-normal direction. This coupling scheme is one of the solutions to increase the mode size overlap efficiency by expanding the mode field diameter by diffraction grating-based couplers. Such structures are obtained by periodically altering the waveguide refractive index profile along the propagation direction. Thereby, the phase-matching is ensured between the guided optical mode through the chip and the fiber

mode. Fibers or fiber arrays are placed with an oblique or a vertical angle for alignment to the light diffracted from the circuitry. The vertical coupling method allows access to any position on the circuit (determined by design), which has an immediate advantage for characterizing different quantum emitters. However, the coupling efficiency of the vertical scheme is in general wavelength and polarization-dependent, which limits the flexibility for the hybrid integration (Marchetti et al., 2019; Son et al., 2018).

Figure 1.9.a shows the coupling between the single-photon emission from individually accessible colloidal quantum dots embedded in a waveguide-integrated device to the fiber arrays via 3D grating-assisted and polymer couplers (Eich et al., 2021). A 3D direct laser writing technique fabricates couplers. 3D grating-assisted coupler is utilized for in-coupling with 28 % efficiency (-5.5 dB) to chip, where polymer couplers are employed for out-coupling the single-photon emission with ~ 71 % efficiency (-1.5 dB). Polymer couplers offer a broadband solution with further improved alignment tolerance compared to the grating couplers (Gehring et al., 2019).

As an alternative method, solid immersion lenses can be formed on QDs also by femtosecond two-photon 3D laser printers as it is shown in Fig. 1.9.b (Bremer et al., 2020). The fabrication process is combined with the low-temperature 3D *in situ* lithography for deterministic fabrication of the devices. Microlens expand the QD's optical mode size and couple it out orthogonally from the chip surface to the SMF. Single-photon emission from the InGaAs QD that is on GaAs substrate with a distributed Bragg-mirror reflector top-surface (below the QD layer) couples into the fiber with 22% efficiency (Sartison et al., 2017).

Evanescent coupling method is based on the power transfer from an integrated waveguide coupler (e.g. a tapered waveguide structure) to the external specialty optical fiber (or vice versa in the case of in-coupling to the chip) that are placed in close proximity. The evanescent tails of the guided modes of the waveguides are coupled to each other, and the coupled waveguides form a new hybrid optical mode. The mode propagating in the inversely tapered waveguide⁽⁹⁾ is gradually transferred to the fiber, whose diameter is increased in the propagation direction. The mode transfer happens mainly at the point where the waveguide and fiber effective refractive indices are equal to each other. Evanescent coupling can theoretically reach to near-unity coupling efficiency, whereas maximum coupling efficiency is limited in a vertical scheme. Besides, evanescent coupling offers an increased bandwidth operation and can offer smaller footprint designs. In principle, the evanescent coupling has several advantages, however, it has lower alignment tolerance. In addition, scaling up the coupling ports is practically challenging, as it is demanding robust, repeatable, cryo-compatible alignment systems and fibers (and fiber arrays).

In Figure 1.9.c single-photon emission from InAs QD is evanescently coupled from a suspended, inversely tapered GaAs to a dimpled tapered SMF (Daveau et al., 2017). Theoretical coupling efficiency between the studied chip and fiber is calculated as 95 % and experimentally 80 % is measured. Figure 1.9.d demonstrates the evanescent coupling

⁽⁹⁾ Waveguide structure, whose dimensions (or only one dimension) are reduced (tapered) along the signal propagation direction (toward the terminating end).

between a suspended tapered waveguide and a single-sided tapered fiber (Tiecke et al., 2015) with a 97 % measured coupling efficiency, while the calculated efficiency is > 99 %.

In-plane coupling method is the most straightforward technique, which can couple optical signals between two waveguides from chip-to-chip and chip-to-fiber. Also, the end-fire chip-to-fiber coupling is a very mature technique, which was first introduced in 1970s (Burns & Hocker, 1977). Usually, inverted tapers are formed at the waveguide edges for mode conversion, increasing the mode field diameter (MFD) of the optical mode of the chip. Similarly, to modify the spatial mode size of the fiber, lensed facets can be formed at the tips. The spatial overlap between the transverse fields of fiber and integrated waveguide defines the coupling efficiency. Figure 1.9.e demonstrates lensed fibers for in- and out-coupling to the waveguide, which is not tapered but cleaved (Davanco et al., 2017). This single-photon source is defined on a Si_3N_4 waveguide, and mode transfer between these two integrated waveguides is based on evanescent coupling. GaAs with the embedded QD source on the Si_3N_4 intermediate waveguide for fiber coupling is placed on a SiO_2 substrate.

On the one hand, this technique has a large operation band and low polarization sensitivity. On the other hand, it requires precise spatial alignment, as coupling tolerance to optical mode offset (between fiber and coupler) is very low, especially compared to vertical coupling (Marchetti et al., 2019). Even though, in general, end-fire coupling requires specific post-processing steps for high optical-quality end-facets at the chip-edges, such as cleaving (or dicing) and end-face coating (or polishing), such techniques are well-established. With this approach, multi-port in- and out-coupling simultaneous operations require less complex imaging systems and alignment stages than other schemes. Especially, deterministic single-photon sources built on high refractive index materials requires adiabatic inverse tapering for slowly converting the mode field diameter for an optimized overlap with the fiber mode. Since the adiabatic theorem holds for slow tapering, which results in long tapered structures or requires a cladding material, as a consequence, the footprint can limit the port numbers for in- and out-coupling. Inverted taper to lensed fiber coupling method will be introduced by providing comprehensive information in Chapter 3. An InAs QD embedded GaAs spot size converter, cladded with a polymer, shows single-photon out-coupling to a lensed fiber. Methods and results are further discussed to explain efficient mode coupling (Uğurlu et al., 2019) as a potential technique that can route photons efficiently in and out of the quantum photonic source chip.

FABRICATION OF NANOPHOTONIC DEVICES

The realization of quantum dot-based integrated photonic devices relies on top-down and bottom-up nanofabrication methods. The bottom-up process is used to form nanolayers of self-assembled InAs quantum dots grown on GaAs, which are the single-photon emitters of this thesis work. Integrated circuits containing these single-photon sources are built by means of top-down techniques such as lithography and etching processes. QDs integrated in engineered nanophotonic structures, such as nanobeam and photonic crystal waveguides, or cavities that can be controlled by an external electric field play an important role as quantum light sources. This is because the direct bandgap and high-index contrast of GaAs, in combination with sophisticated device engineering, allow deterministic generation of single photons with improved spontaneous emission rates (Hughes, 2004), improved β -factors (Javadi et al., 2018) and strong confinement of the guided mode. Furthermore, component integration allows low-loss signal transfer between different quantum nodes by direct fiber-coupling.

In this thesis, we present the study of three different devices: **i.** efficient single-photon out-coupling device, formed by free-standing optical epoxy-polymer cladded spot-size converter (SSC) for the end-face coupling from GaAs-based nanophotonic waveguides to a single-mode lensed fiber (Chapter 3), **ii.** plug-and-play device for waveguide-based in-plane resonant excitation, **iii.** proof-of-concept device for multi-port chip-to-chip and chip-to-fiber single-photon coupling. In this chapter we explain the fabrication steps of single-photon devices by focusing on the realization of epoxy-polymer SSC. The single-port SSC out-coupler is an InAs QD-based GaAs inverted taper, cladded by an optical epoxy polymer overlay. The single-port coupler and multi-port couplers are both fabricated by following similar processing steps. The realization of suspended polymer waveguides is challenging, as it requires materials that withstand the processing steps (e.g. wet etching) and cryogenic conditions. The multi-port couplers require additional micro-deposited glue channels and optical adhesives for

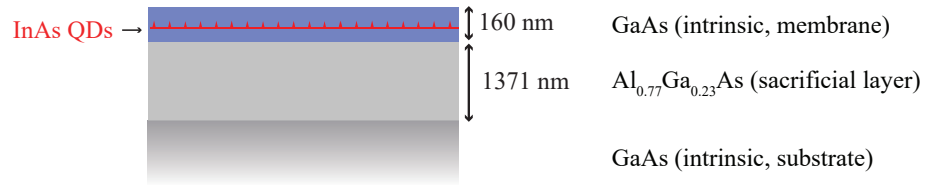


Figure 2.1: Layout of the quantum dot wafer. The quantum dot layer, grown with substrate rotation, is embedded in a 160 nm-thick layer of GaAs, constituting the membrane. The AlGaAs, named as sacrificial layer is removed to suspend photonic structures.

coupling permanently to fiber arrays. The fabrication process steps of the plug-and-play device can be found in (Y. Wang, 2021).

Initially, a brief description of the epitaxially grown InAs/GaAs QDs is given followed by the step-by-step description of the nanophotonic circuit fabrication process. Then, the dry etching method is explained, which is used for transferring the patterned e-beam soft-mask to the substrate. Following that, wet etching technique is presented that is employed to form free-standing circuitry on the GaAs membrane. The latter part represents the optimized fabrication method for forming the suspended epoxy based polymer waveguide claddings. The experimental study of such devices will be introduced in Chapter 3. The relevant fabrication protocols are presented in Appendix A tables step-by-step with details.

2.1 EPITAXIALLY SELF-ASSEMBLED QUANTUM DOTS

A self-assembly technique during semiconductor epitaxial growth process is used to form three-dimensional nanometer-sized islands of QDs by means of elastic strain relaxation. These nanostructures are fabricated by molecular beam epitaxy (MBE), offering a precise control on the crystal growth in Stranski-Krastanov (SK) mode. Following the layer-by-layer semiconductor epitaxial growth (of GaAs), SK growth mode induces spontaneous formation of three-dimensional clusters of QDs (e.g. InAs or InGaAs). The three-dimensional island formation is a result of compressive strain between the epitaxial layer (QD) on substrate (GaAs) led by the lattice mismatch of 7% between InAs on GaAs. By tuning the growth conditions while increasing the deposition thickness (such as deposition rate, growth temperature, flux, diffusion rate), the strain-driven change in the surface structure influences the QD size and, accordingly, the emission wavelength. In comparison to other solid-state systems, epitaxially grown semiconductor QDs demonstrate high optical stability. They have the advantage of integrability with other semiconductor structures and fabrication techniques, such as electrical gates and optical cavities.

Figure 2.1 illustrates a sketch of the GaAs undoped wafer layer structure, containing a self-assembled InAs QD layer in the GaAs membrane. The density of the QDs are

observed to be as high as $1\text{--}10/\mu\text{m}^2$, with a central emission wavelength of ~ 920 nm. Samples investigated in this work, InAs/GaAs QD epitaxial layer stacks are provided by the research group (Dr. Arne Ludwig, Dr. Sven Scholz, Dr. Rüdiger Schott) at the Ruhr-University of Bochum, Germany, which is led by Prof. Andreas Wieck. The complete description of the growth process can be found in the reference (Ludwig et al., 2017).

2.2 ELECTRON-BEAM LITHOGRAPHY

Lithography is a fabrication process that consists in the transferring of designed geometrical patterns onto the surface of a sample. To do so, a thin layer of organic film (resist) coating the substrate is exposed by beams of different nature (e.g. electron, or e-beam, or UV photons) either through a mask or by direct writing.

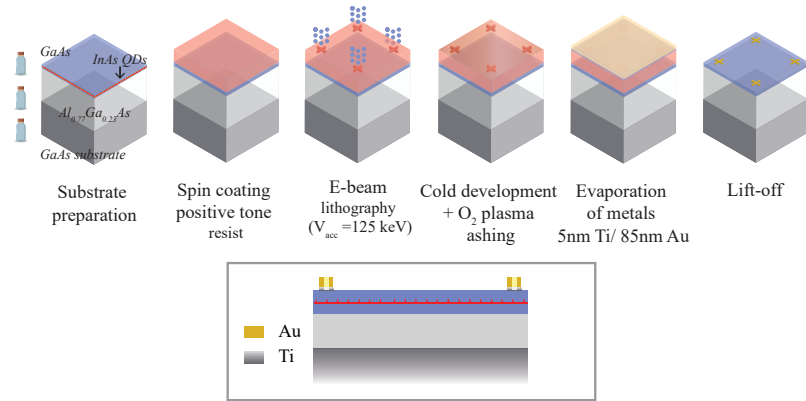
Direct-write e-beam lithography (EBL) technique has been widely applied as a direct method of writing structures down to nanometer scale without using any physical mask. In this thesis work, we also use EBL method to pattern the GaAs and the polymer waveguides. Our e-beam lithography tool is **Elionix ELS-F125**, which has an acceleration voltage of $V_{acc} = 125$ keV, which leads to smaller feature sizes (high resolution patterning). Initially, alignment markers are patterned on the GaAs substrate by EBL and defined by the e-beam evaporation and lift off (see Fig. 2.2.a). Subsequently, the GaAs waveguide circuit is written by EBL. The nanocircuitry is fabricated on the substrate by dry etching: reactive ion etching (RIE) and wet etching (resist strip)(see Fig. 2.2.b). Finally, an epoxy polymer resin is spin-coated on the substrate and exposed by e-beams to form the overlay cladding around GaAs device components and support structures and post processed to make the three dimensional permanent structures on the GaAs substrate. Finally, the chip is cleaved and the devices are suspended by HF liquid undercut (see Fig. 2.2.c).

This section illustrates the EBL method optimized and developed for building suspended spot size converters with epoxy polymer cladding for lensed fiber coupling and multiport fiber array coupling. We address important performance parameters influencing the EBL: the substrate quality, sample preparation (resist choice and spin-coating), mask design, exposure file preparation, choice of right exposure variables, resist development, and, depending on the resist mask, physical or chemical stabilization (e.g. by baking for thermally cross-linking).

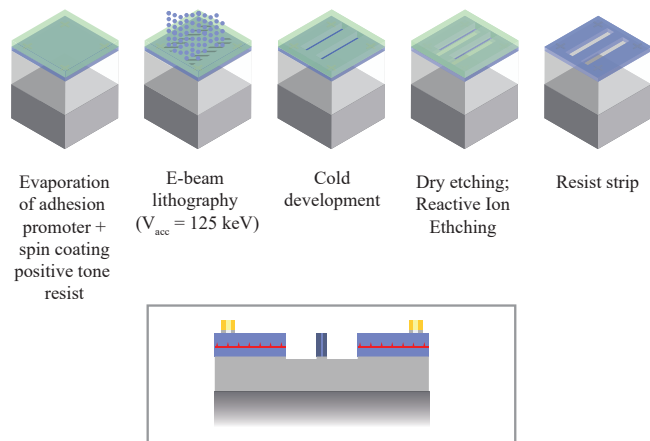
2.2.1 Sample preparation

To generate a soft-mask for transferring the circuit pattern onto the GaAs layer, initially we need to coat the substrate (see Fig. 2.2.a 2nd step, b and c initial steps) with an electron beam sensitive polymer film (e-beam resist). While exposing the resist, upon electron irradiation, a fraction of the electron beam energy is used to modify the chemical properties of the resists, by breaking the molecules or by generating longer polymeric chains. In the first case (positive tone), the exposed areas of the resist become more soluble and get completely dissolved when dipped in a particular solution after

(a) 1st step: Fabrication of alignment markers



(b) 2nd step: Fabrication of GaAs nanostructures



(c) 3rd step: Fabrication of epoxy polymer cladding

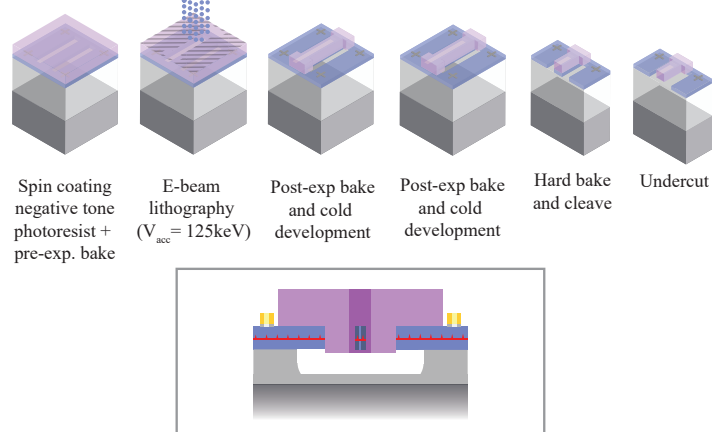


Figure 2.2: Fabrication process flow. (a) Alignment markers are written by EBL and Ti/Au layers are e-beam evaporated. Consequently, cross marks are defined by the lift-off process. (b) GaAs nanostructures (inverted tapers, nanobeam waveguides, circular grating couplers, loop mirrors) are formed on the membrane by EBL patterning followed by dry etching: reactive ion etching (RIE). (c) Substrate is spin-coated by an epoxy polymer resin in order to form the overlay cladding for the GaAs inverted tapers and support structures by means of EBL. Post-processing steps ensure permanent three dimensional structures and HF undercut suspends the devices.

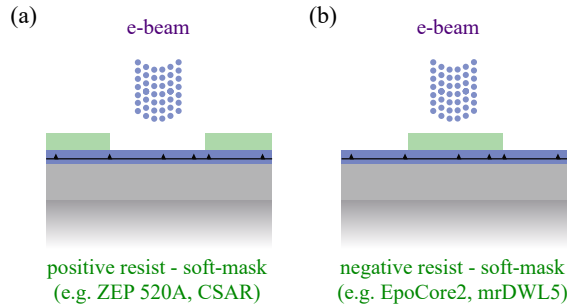


Figure 2.3: Illustration of e-beam patterning (soft-mask formation) mechanisms. (a) Positive and (b) negative tone resists.

exposure (development). On the contrary, the exposed areas of a negative tone resist (see Fig. 1.3.b) cross-link and become insoluble inside the developing solution. The design to be exposed dictates the choice of which type of resist should be preferred.

Before depositing the resist on the sample surface, a pre-cleaning and dehydration procedures are necessary in order to eliminate any potential trace of contamination and adhesion failures (respectively). Accordingly, in the first fabrication step (see Fig. 2.2.a), substrate is cleaned and baked before spin coating ZEP520A (Zeon Europe GmbH), a positive tone e-beam resist. ZEP520A has high sensitivity against e-beam, which leads to high resolution features. In the 2nd fabrication step (see Fig. 2.2.b), we used additionally pre-resist priming by evaporating a thin layer of Ti (2 nm) to enhance the substrate adhesion. Here we form inverted tapers where the waveguide width is reduced from 200 nm to 60 nm along 11 μm . The defined structure has a large thickness/width ratio, which reduces the adhesion between polymer resist and substrate. Additionally, GaAs already has low adhesion properties, necessitating an adhesion promoter. In this step we used a ZEP520A alternative, CSAR (Allresist GmbH), which also shows high contrast and high stability under etching process.

2.2.2 Mask design and exposure preparation

The optimized nanophotonic device geometries (see numerical simulations in Chapter 3) are used for designing integrated circuit masks. Circuit masks are drawn by utilizing a MATLAB written code. Different device components (metal alignment markers, GaAs circuits, epoxy-polymer cladding structures) that need a different post exposure processing are designed at separate circuit layers. The nanofabrication work flow is described in Figure 2.2 and involves three EBL steps for processing different lithography layers.

Before the e-beam patterning, an exposure file needs to be prepared to apply a series of corrections on the mask file and appropriately adjust exposure conditions.

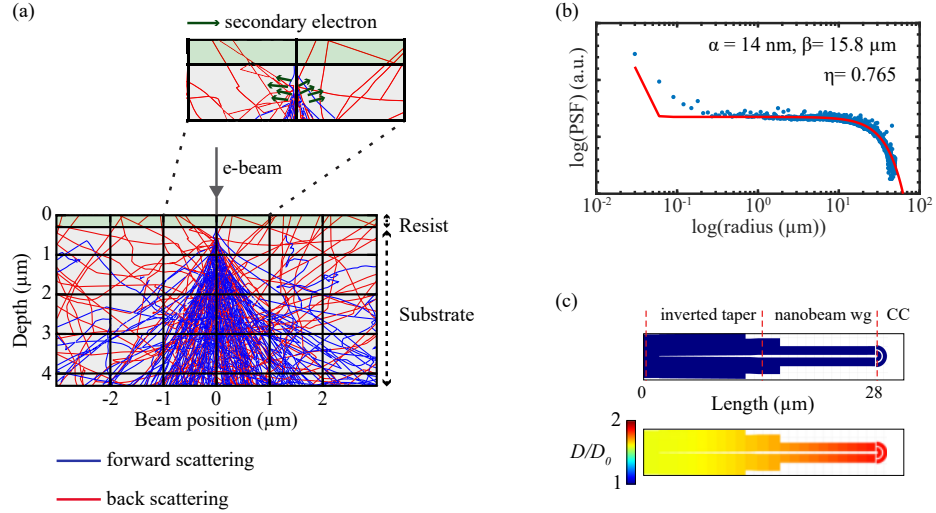


Figure 2.4: Proximity effect correction (PEC). (a) Monte Carlo simulation of the electron trajectories in both resist and substrate showing primary (forward) and back-scattered electrons. Also the low-energy secondary electrons are shown in the inset. The simulation is done for the positive tone ebeam resist: ZEP520A with 550 nm thickness (green highlighted) that is spin coated on a substrate of GaAs (grey highlighted). The acceleration voltage for electrons in the beam is set to 125 keV. (b) Point spread function (PSF) that is acquired from Monte Carlo simulation in (a), shown with blue dots. PSF described by the fit using two Gaussian functions (that are described by their FWHM parameters), shown with red line. The fit parameters α , β , η describe respectively forward scattering of electrons penetrating into the material, backscattering and the ratio of the back-scattered to forward scattered energy. (c) Top image; Nanophotonic structure combining an inverted tapered and a nanobeam waveguide (wg) with a circular grating coupler (cc). Here the material stacks are 200 nm thick CSAR 9 resist, that is spin-coated on GaAs. Bottom image: Pattern with PEC.

Corrections are made to get the ideal pattern from the exposure process and to avoid potential writing errors based on **i.** misalignment, **ii.** stitching, **iii.** proximity effect.

Misalignment errors are controlled by designing metal marks on the mask, which is then exported to the exposure file. We use cross local marks on our chips for correcting the displacement in position and rotation. Consequently, marker positions can be controlled for alignment by the EBL system's stage interferometer. In pre-exposure settings, alignment can be improved further by choosing the optimal detector (between secondary electron and back scattered electron detectors) based on the marker material that is exposed and the thickness of it. The alignment markers at the first mask layer can assure an accurate pattern overlay between the subsequent exposure layers.

Stitching errors can occur when the design of the circuit pattern is larger than the write field of the e-beam ⁽ⁱ⁾ (max. size is 500 μm^2 at V_{Acc} 125 keV). To avoid the stitching field position error, the layout should be designed accordingly. The critical exposure

(i) The exposed area without moving the stage. Only the e-beam is deflected to expose the individual patterns inside the field area.

areas involving the entire device should be fragmented carefully to fit completely inside a single writing field or to position it by considering the stitching tolerance of the EBL system (20 nm error for the max. write field size).

Proximity effect occurs due to the electron scattering effects in the resist layer and substrate during the exposure process. Regardless of how precisely the e-beam can focus on the resist, such scattering events are unavoidable in electron-matter interactions, resulting in beam broadening. Consequently, to have uniform exposure and obtain accurate and reproducible patterns structures, pre-exposure corrections are necessary. The acceleration voltage of the EBL systems are typically between 10-125 keV. Higher V_{acc} results in large penetration depth that is at least an order of magnitude more than the thickness of the resist. As a result, electrons penetrate through the resist layer into the GaAs substrate. Additionally, beam diffusion is larger, leading to a more sparse back scattered electron errors (see Fig. 2.4).

Although the electron beam has a certain beam diameter, three dimensional deposition of the beam energy distribution in the resist layer and the penetration depth of the electrons lead to scattering events. Consequently, the applied effective exposure dose increases and geometrical dimensions of fabricated device diverges from the design parameters, resulting in a reduced resolution. Different exposure correction methods can be applied to avoid proximity effects, which are background correction exposure, shape modification and dose modification.

We use dose modification for each pixel to achieve spatial dose uniformity during the exposure as a proximity effect correction (PEC) method. Typically the exposure dose (or area dose) D is dependent on the beam current I , dwelling time at each pixel τ , and the exposure grid spacing (or pitch between the pixels) P , and can be calculated as $D = I\tau/P^2$. At a pixel (point) exposure, energy density profile of the e-beam can be modeled on the resist layer by the so-called point spread function (PSF). The e-beam interaction with the resist and substrate and scattering probabilities are schematically represented in Figure 2.4.a, where we see the generated forward and backward scattered electrons. Secondary electrons (see inset) are formed as a result of the energy dissipation from the primary electrons and they have low energy (a few eV). To simplify the non-trivial form of the PSF, the energy distribution can be approximated by several methods. Commonly, the PSF is approximated by the sum of two Gaussian distributions. It is obtained by Fourier transforming and normalizing the energy density profile:

$$\text{PSF}(r) \approx \frac{1}{\pi(\eta+1)} \left[\frac{1}{\alpha^2} \exp\left(-\frac{r^2}{\alpha^2}\right) + \frac{\eta}{\beta^2} \exp\left(-\frac{r^2}{\beta^2}\right) \right]. \quad (2.1)$$

where, r is the radial distance from the e-beam spot, α and β are the FWHM of the Gaussian curve correlated with forward scattering (low-range scattered) and back scattering (long-range scattered), respectively. The ratio of backscattering to forward scattering is given by the coefficient η . Proximity effect coefficients are calculated by a Monte Carlo technique, which simulates the random trajectories of electrons to calculate the spatial dependence of the exposed e-beam energy upon each scattering event. We use a commercially available software package, which can simulate the proximity effect

and can fit the PSF for different material layer structures: BeamFox Technologies ApS⁽²⁾. This software gives the exposure energy estimations by performing a 2D convolution of the fitted PSF with the geometries in the mask. Consequently, mask's exposure profile containing multiple fractured subfields in form of polygons is calculated. For each fractured polygon the dwelling time is calculated for PEC compensation. Figure 2.4.b represents the normalized PSF, which is obtained from the Monte Carlo simulation (see Fig. 2.4.a) for 125 keV incident electrons. The fit shows that the proximity effect has the dominant contribution from the backscattered electrons ($\beta \gg \alpha$) and the resulting energy is diffused to a distance of $\beta \approx 16 \mu\text{m}$.

Figure 2.4.c top shows the pattern that is designed at the second layer fabrication of our device (see Fig. 2.2.b), where the material layer structure is formed by 200 nm thick CSAR9 on GaAs substrate. Here, we see the design of the inverted taper structure linked to a circular grating coupler through a nanobeam waveguide. Figure 2.4.c bottom structure represents consequent compensation for proximity effects with a color map showing the dwell time (exposure dose coefficient) profile. For each fractured polygon on the pattern, the estimated exposure dose D is normalized to the the clearing dose D_0 , which is the minimum dose required to completely open the large area. Based on the denser existence of the proximity effect from the the neighboring structures, central area shows a decreased value of D/D_0 compared to the edges of the device.

2.2.3 Exposure and Development

After spin-coating and preparing the mask files, the samples are loaded in the chamber of an *Elionix* F125 and exposed with the appropriate dosage. For CSAR resist, a 'cold development' process with n-Amyl acetate at -5°C can be used to improve resist contrast and reduce edge roughness (Hu et al., 2004; Ocola & Stein, 2006). This improvement is typically skipped when defining alignment markers, but incorporated when patterning the shallow-etch grating and the GaAs circuit features. For the step-by-step process flow, see Appendix A.1, and for discussion of relevant modifications for the negative epoxy polymers, see Section 2.4.

Minimum achievable feature size is defined by the minimum spot diameter of the EBL machine. It is determined by the system's de Broglie wavelength $\lambda = h/p$, where h and p are the Planck constant and momentum, respectively. The momentum is defined by $p = 2m_0eV$, where m_0 the mass of the electron at rest, e charge of the electron, V the acceleration voltage of the electron potential. Our e-beam lithography tool is with $V_{acc} = 125 \text{ keV}$ and its de Broglie wavelength of 0.029 \AA . Since the electron wavelength is sufficiently small, the resolution is not diffraction limited. The resolution of the EBL is dependent on the electron optical aberrations of the system and electron scattering events during the exposure. Our EBL system can achieve a minimum beam diameter of 1.7 nm and pattern structures with the minimum linewidth of 5 nm at its highest V_{acc} .

(2) <https://www.beamfox.dk>

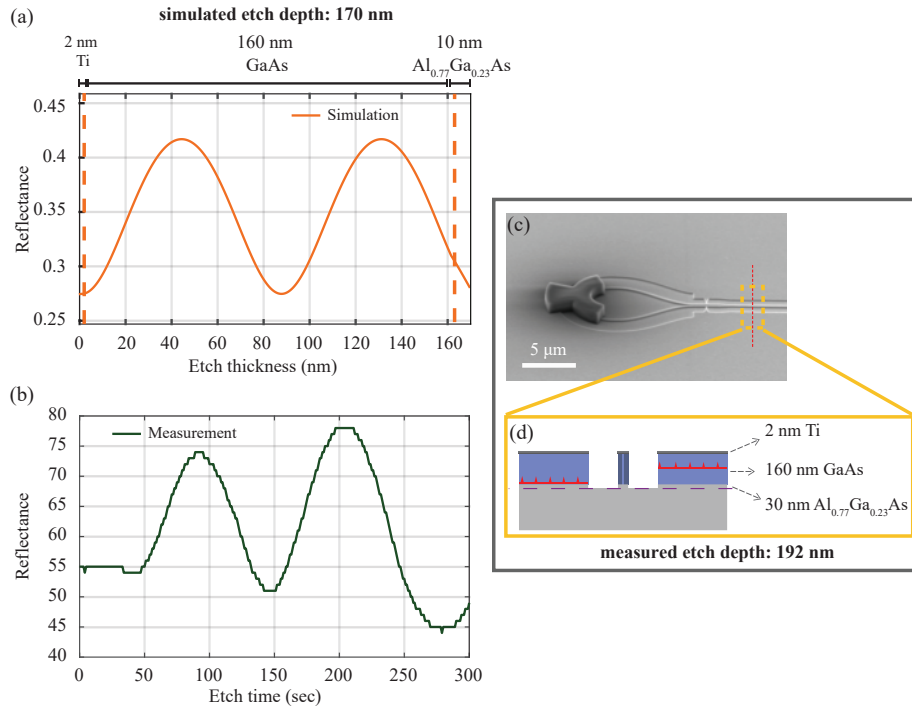


Figure 2.5: Endpoint detection technique used to control the reactive ion etching (RIE) process, used for forming GaAs nanophotonic circuitry. (a) Calculated end point detection signal is shown as a function of material thickness. (b) Measured endpoint detection intensity is plotted as a function of etch time. Etching process is controlled by tracking the change in the optical emission intensity. (c) Tilted scanning electron microscope (SEM) of the etched GaAs circuitry, specifically zoomed-in to the loop mirror reflector device. (d) Sketch of the cross section of the waveguide after the etch process to illustrate the layers etched through (2 nm Ti, 160 nm GaAs, 30 nm AlGaAs after cold development).

2.3 ETCHING

Both dry and wet etching processes are utilized in this work. Standard dry etching techniques are used to anisotropically remove material when defining all planar features during the processing. Wet etching is only used at the end to create suspended structures by removing AlGaAs from beneath GaAs with high selectivity.

2.3.1 Dry etching

To isotropically etch vertical features, dry etch processes are performed with an Oxford Plasmalab 100 system equipped with $\text{BCl}_3/\text{Cl}_2/\text{Ar}$ chemistry, which maintains good selectivity with respect to chosen photoresists. Obtaining the correct etch depth is

of critical importance to yield the desired structures. To this end, basic reactive ion etching is used ⁽³⁾ with calibrated laser-based etch monitoring.

The laser etch monitoring was calibrated through comparison of measured reflectance profiles to calculations based on layer indices and wavelength of the sensing laser (Fig. 2.5), and confirmed by mechanical profile measurements (KLA Tencor Profilometer). Initially, this etch monitoring technique produced inconsistent results when using Ti as an adhesion promoting layer. However, this issue seems to have been resolved by switching to AR-30080 (Allresist).

For more detailed information on the optimized RIE processes, see the thesis of Tommaso Pregmolata (Pregmolato, 2019).

2.3.2 Wet etching

Liquid HF (5%) is used to isotropically remove the sacrificial AlGaAs layer, releasing the fabricated GaAs device with polymer layer cladding. As shown in Fig. 2.7.b, polymer residues are typically present after the HF release. These can be removed with a special cleaning step involving H₂O₂ and HCl (Midolo et al., 2015), the specific details of which can be found in Appendix A.2.

In principle, most photoresists are able to mask against HF etching. However, dissociated fluorine ions F⁻ are able to penetrate photoresist and attack the surfaces intended to be masked. This leads to a reduction in adhesion and ultimately delamination of the photoresist layer. This suggests that thicker photoresist claddings are more robust with respect to this process step.

2.4 PROCESS MODIFICATIONS FOR OPTICAL POLYMERS

We use an epoxy polymer resin, EpoCore2 (Micro resist technology GmbH), to form the cladding waveguides around the inverted tapers and support structures to avoid bending or collapsing (see Fig. 2.7a) in the third lithography step (see Fig. 2.4.c). EpoCore2 is a negative tone resist with sensitivity to both ultra-violet light (i-line) and electron beams. EpoCore2 was chosen based on its refractive index ($n \approx 1.45$ at 930-940 nm), thickness ($t \sim 1.15 \mu\text{m}$), chemical stability (to undercut chemicals) and cryogenic temperature compatibility (operation $T \leq 10 \text{ K}$). Although EpoCore2 is not designed for EBL (as it is a highly sensitive material), it can be patterned by e-beam exposure. After several iterations, our fabrication method is optimized for EpoCore2 processing.

This section focuses on EpoCore2-specific processing procedures, along with their motivations.

Pre-exposure processing of epoxy polymer

⁽³⁾ The tool has the option to activate an inductively coupled plasma (ICP) source to achieve deep and vertical etching of small features (e.g. photonic crystal holes). However, this does not allow good control of etching depth.

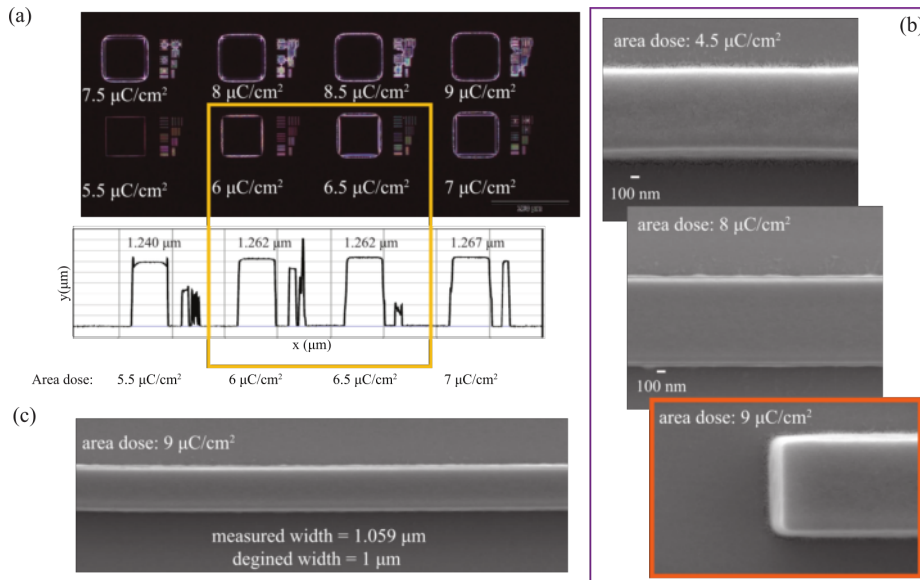


Figure 2.6: Electron beam dose optimization. (a) The optical microscope image of the developed sample along with (b) SEM images of the fabricated structures, where we observed the least resist residues adjoined the exposed patterns for 9 $\mu\text{C}/\text{cm}^2$ clearance dose. (c) confirms the best agreement between the designed and fabricated dimensions of the epoxy polymer rectangles.

Nominally, spin-coating EpoCore2 at 3000rpm results in a 2 μm thick resist layer. To obtain a reduced thickness of $\sim 1.15 \mu\text{m}$, an initial high speed spin rate is applied for a short time before spin-coating. The subsequent spin coating time is adjusted to optimize coating uniformity over the entire sample surface.

Exposure file preparation of epoxy polymers

When the resist thickness becomes too large, the forward electron scattering starts to play a more relevant role in the final exposure resolution. In order to take this into account, the exposure files are prepared by only the fracturing of the geometries and not the PEC. To control the pattern size and prevent resist residues, we optimized the exposure parameters by exposing the patterns at different pitches and exposure doses (dwell times).

E-beam processing of the negative tone epoxy polymer resist

Figure 2.6 shows the electron beam dose optimization that is performed by tuning the area dose on the test arrays (composed of 100 $\mu\text{m} \times 100 \mu\text{m}$ squares and rectangles with varying widths). The minimal dose is determined as 6 $\mu\text{C}/\text{cm}^2$, also indicating the resist sensitivity (as no increase is observed in the exposed resist thickness). The least resist

residues were observed for a clearance dose of $9 \mu\text{C}/\text{cm}^2$, which also produced sufficient pattern reproduction for a rectangular structure representing a critical dimension of $1 \mu\text{m}$.

Post e-beam processing of epoxy polymer

As EpoCore2 is a negative-tone resist, it requires a post-exposure bake (PEB) to cross-link the polymers of exposed regions. Specifically, EpoCore2 requires a temperature-ramped PEB with a programmable hotplate, ending with a 3 min bake at 85°C . Afterwards, the sample must cool down for 40 minutes prior to development.

A development process is also used for the EpoCore2, but with mr-Dev 600 developer (Microresist) at -5°C instead of n-Amyl acetate. It was found that increasing the development time from 40 s to 60 s reduced residues without leading to critical issues from over-developing. Immediately after development, the remaining resist residues are removed using O_2 plasma in a barrel etcher for 10 minutes.

2.5 SAMPLE POST-PROCESSING

Although the previous fabrication steps inherently complete the structures, each sample piece needs to be appropriately fractured to realize functional devices capable of launching photons off the substrate edge. This is accomplished with high-resolution cleaving, followed by a critical point dry to avoid exposing the delicate structures to relatively strong capillary forces (Midolo et al., 2015). This would be the final step for a functional device. However, a sample to be imaged by SEM requires further deposition of a conductive layer (typically gold) to avoid charge build-up within the epoxy material. While this produces successful images (Fig. 2.7.d and e.), the imaged device is unfortunately unusable for experiments.

Cleaving

Samples are cleaved prior the HF wet etch step, which removes the sacrificial AlGaAs layer and releases the structures. To achieve proper cleaving of the sample with suspended edge tips, the wafers are designed with inverted tapers facing each other and connected by a long epoxy waveguides. The samples are cleaved before undercut to avoid tearing apart the fragile structures. Care had to be taken to handle the sample during the undercut as the epoxy tips can be ruined by tweezers.

Critical-point drying

Immediately following the wet etching process (Sec. 2.3.2), this final step is used to prevent the effects of stiction from causing structural deformation or collapsing of the released structures, which can occur when removing the sample from the the IPA at the end of the previous processing step. By using a a standard critical point dryer (CPD) tool (Leica EM CPD300), we prevent the exposure of the sample to a liquid/air interface, where surface tension can lead to relatively large forces on the sample

structures. Instead, the sample arrives in a completely gaseous state by transversing around the phase transition line on water's pressure-temperature phase diagram. The final results are shown in Figure 2.7.d and e, exhibiting the successfully suspended epoxy-polymer cladded GaAs inverted tapers. The smooth polymer structures highlight the optimization of the EBL process, while the apparent cleanliness demonstrates the effectiveness of the post-processing optimization.

Figure 2.7.d is the SEM of the epoxy polymer cladding with polymer tethers that are patterned perpendicular to the light propagation direction without adding significant loss (-0.025 dB) as confirmed by numerical simulations. Such support tethers are formed to prevent bending or collapsing of the overlay cladding onto the substrate after the undercut process due to capillary forces. When the polymer structure is patterned longer, a small bending can be observed, caused by the strain relaxation. This specific device design is studied in Chapter 3. Figure 2.7.e shows the device built with GaAs tethers for the same reason. The insets show the tilted images, where the residue free devices components (loop mirror reflector and polymer cladded inverted taper) are fabricated by controlling the bending of the devices.

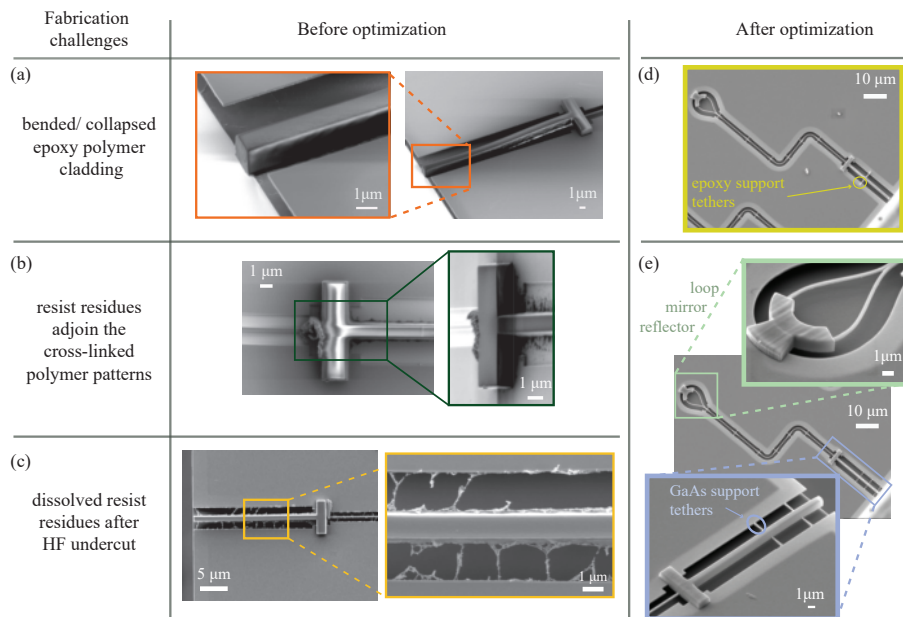


Figure 2.7: Fabrication challenges and optimized results. (a) SEM images of the polymer overlay cladding, formed around the GaAs inverted taper is collapsed after the HF undercut process (zoomed-in image confirms the completely collapsed endface). (b) SEM image shows the remaining the resist residues around the exposed polymer patterns, after the hardbake process. Zoomed-in, tilted image highlights the adjoining residues. (c) SEM images show the dissolved residual resist after HF undercut process. Remaining resists showed in (b) are suspected to be the source of sprinkled polymers around the polymer patterns. (d) SEM image represents the fabricated SSC where the overlay polymer is supported by polymer tethers preventing the bending. (e) SEM image illustrates the polymer cladded SSC with GaAs tethers and insets are the zoomed in images of the tilted images of the loop mirror reflector and the out-coupler.

CHAPTER
3**REALIZATION OF SUSPENDED SPOT-SIZE
CONVERTERS**

This chapter focuses on efficient end-face out-coupling of single photons from a GaAs-based nanophotonic waveguide with embedded quantum dots based on an optical spot-size converter. The converter is realized using an inverted taper and an epoxy polymer overlay providing a $1.3\ \mu\text{m}$ output mode field diameter. We demonstrate the collection of single photons from a quantum dot into a lensed fiber with a rate of 5.84 ± 0.01 MHz and estimate a chip-to-fiber coupling efficiency of $\sim 48\%$. The stability and compatibility with cryogenic temperatures make the epoxy waveguides a promising material to realize efficient and scalable interconnects between heterogeneous quantum photonic integrated circuits. The work represented in this chapter closely follows Ref. (Uğurlu et al., 2019).

Single-photon devices such as emitters, routers, and detectors have been recently developed worldwide to extend the functionality of classical photonic integrated circuits towards on-chip quantum information processing (C. P. Dietrich et al., 2016). Chip-scale integration enables scaling up these devices to achieve multi-photon operation required for simulation and computing (O’Brien et al., 2009; Rudolph, 2017). To this end, quantum dots (QDs) in gallium arsenide (GaAs) waveguides (Lodahl et al., 2015) provide an excellent platform for generating photons with high indistinguishability and efficiency (Ding et al., 2016). However, despite the excellent progress in routing and detecting photons on this platform, (Papon et al., 2019; Sprengers et al., 2011) scaling quantum optics experiments with integrated circuits based exclusively on GaAs is rather challenging due to propagation loss. Interfacing QDs to a different material system could enable a whole new range of applications for ultra-fast switching, low-loss routing, and filtering. For example, in Refs. (Elshaari et al., 2017; Mnaymneh et al., n.d.) a nanowire QD single-photon source was integrated with silicon nitride waveguides enabling filtering and routing operation. Alternatively, GaAs waveguides have been

epitaxially lifted-off, transferred to a SiN substrate and processed in-situ (Bovington et al., 2014; Bowers et al., 2016; Davanco et al., 2017). These approaches are challenging as they require compatible substrate materials (such as SiN) and introduce additional fabrication complexity when building electrical gates to QDs, which are essential to control charge noise of the emitter (Kuhlmann et al., 2013). Modern three-dimensional nanofabrication techniques such as photonic bonding (Billah et al., 2018) have also been proposed for interfacing photonic circuits and constitute a potentially scalable approach to multi-chip photonics.

3.1 END-FIRE COUPLING BETWEEN OPTICAL WAVEGUIDES

It is possible to exploit an optical device in such a way that allows end-fire coupling of single photons from the cleaved edge of a GaAs chip to another optical chip or into an optical fiber. Figure 3.1 (top panel) illustrates a dielectric waveguide and a step-index optical fiber (with a large refractive index contrast between the core and cladding $n_1 > n_2$). Side-coupling from an on-chip waveguide requires suppressing back-reflections at the cleaved waveguide edge and, most importantly, enlarging the mode size to avoid field mismatch at the interface. While back-reflection can be controlled using anti-reflection coatings, angled cleaving, or by introducing inverted tapers, (Cohen et al., 2013; Galán et al., 2007; Kiršanskė et al., 2017) the mode matching requires designing spot-size converters (SSC) to expand the optical mode profile. Figure 3.1 (middle panel), shows a tapered waveguide, where the taper profile is calculated by straight waveguide sections (see the taper waveguide section) allowing to evaluate mode solutions locally. Inverted tapers with an overlay polymer (see Fig. 3.1 (bottom panel)) are often adopted in silicon-on-insulator technology (Almeida et al., 2003; Fan & Hooker, 1999; McNab et al., 2003; Roelkens et al., 2006) to perform this task. However, the fabrication process requires a low-index substrate (silica), which can physically support the polymer structure without introducing additional loss. Planar GaAs devices with deterministic photon-emitter coupling, on the contrary, are fabricated on a high-index sacrificial layer ($\text{Al}_x\text{Ga}_{1-x}\text{As}$) which is subsequently removed to form suspended waveguides (Midolo et al., 2015). A cladded inverted taper for this platform has not yet been demonstrated. Although near-unity coupling efficiency has been achieved using tapered fibers directly in contact with the waveguide, (Burek et al., 2017; Daveau et al., 2017) such evanescent coupling scheme suffer from mechanical failures, and are difficult to scale.

3.2 SUSPENDED SPOT-SIZE CONVERTERS FOR LENSED FIBER COUPLING

Following the fabrication method (introduced in in Chapter 2), we built the suspended converters, which can expand the optical spot size of a single-mode GaAs waveguide (refractive index $n = 3.48$ and width 300 nm) to a Gaussian mode with 1.3 μm field diameter, which can be expanded further by increasing the converter length. The materials and processes used ensure vacuum and cryogenic compatibility and sufficient

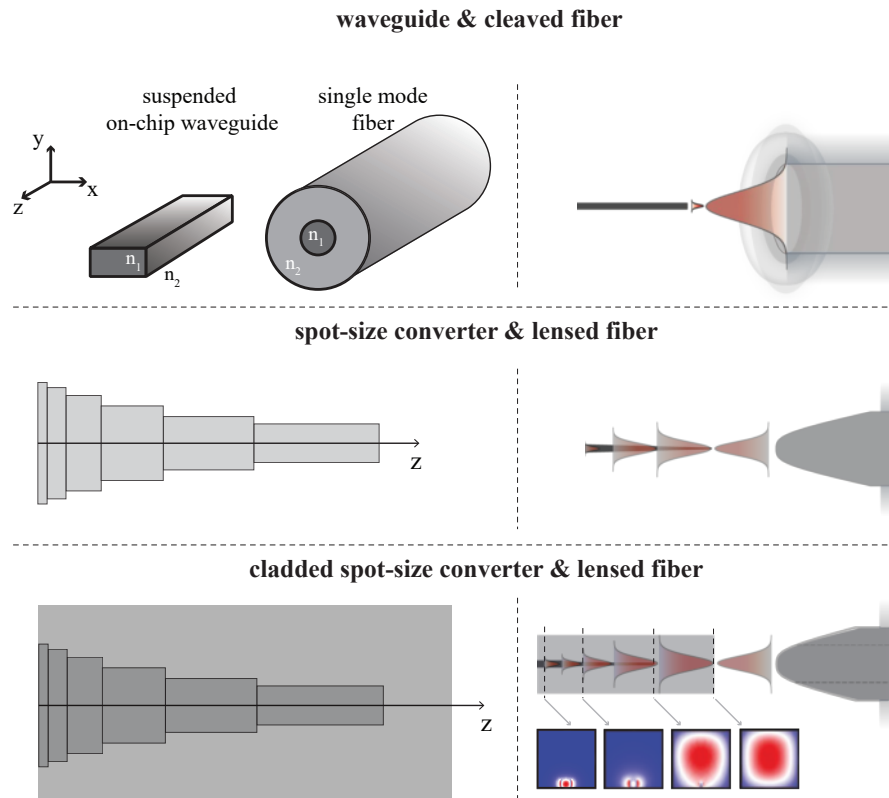


Figure 3.1: End-fire mode coupling between facing waveguides. (a) Coupling between a typical single-mode on-chip slot waveguide with a sub-micron width (for single mode GaAs waveguide; $w_{\text{GaAs}} = 300 \text{ nm}$) and a cleaved single-mode fiber with $5 \mu\text{m}$ core diameter, which defines its mode field diameter at 930 nm . Mode size mismatch between the waveguides limits the coupling efficiency. (b) Tapering the nanophotonic waveguide along its propagation direction and employing a lensed fiber enable the optimal mode-matching. Total power transfer can be achieved by overcoming the mode size mismatch between the waveguide and fiber modes. (c) To further improve the coupling efficiency towards unity and eliminating the scattering losses during the mode transfer from the taper to fiber, tapered waveguide can be encapsulated by an overlay polymer waveguide (with a high refractive index contrast).

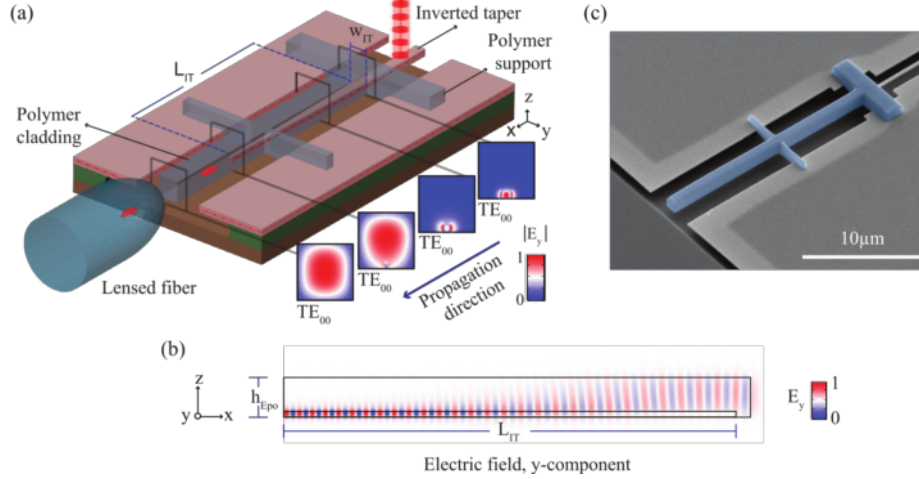


Figure 3.2: Schematic representation of the suspended spot-size converter device with embedded semiconductor QDs. The spot-size converter is composed by a suspended inverse tapered nanobeam waveguide and an epoxy polymer cladding. The nominal width of the waveguide decreases adiabatically from 200 nm to 60 nm over a distance 11 μm . The overlay polymer cladding is formed by two sections, perpendicular to each other, which one of is built along the propagation direction to encapsulate the inverse taper (that is 20 μm long and has equal cross section width and height of 1.15 μm). The vertical epoxy polymer parts are shaped to prevent potential structural collapse (with 2 μm and 0.5 μm wide along the propagation direction, respectively). The lensed fiber is brought close to the output facet of the out-coupler at the edge of the chip. The train of single photon pulses (red pulses) are generated by exciting the embedded QDs in GaAs free standing waveguide by pulsed laser excitation. The insets depict the evolution of the fundamental transverse electric (TE) mode's, which is the simulated mode field profile cross-sections as it propagates along the SSC. (b) The cut-view of the SSC showing the 3D optical simulation showing electric field propagation towards the waveguide tip. (c) A tilted side view SEM image (tilting angle of 45°) of the SSC.

stability during cool-down and operation. The converter has an estimated efficiency of $\sim 48\%$, resulting in up to 5.84 ± 0.01 MHz single-photon rates into a lensed optical fiber. In the present work a single lensed fiber is used for characterization, but the developed SSC enables interfacing, e.g., multiple photonic chips as well, and can readily be scaled-up to multiple channels. As a further benefit of the fabricated device, it has been proposed that the polymer cladding may serve the dual purpose of efficiently suppressing limiting phonon decoherence processes (Dreeßen et al., 2018). This paves the way for an on-demand fiber-coupled single-photon source with simultaneously near-unity degree of indistinguishability of the photons and near-unity coupling efficiency.

3.3 NUMERICAL ANALYSIS OF THE SPOT-SIZE CONVERTER

The SSC presented here consists of a GaAs waveguide and an epoxy-based optical polymer cladding waveguide depicted schematically in Figure 3.2a. The width of the GaAs waveguide (w_{IT}) is gradually reduced to enlarge the area of its fundamental transverse electric (TE_{00}) mode [see inset of Figure 3.2a], which is transferred to the

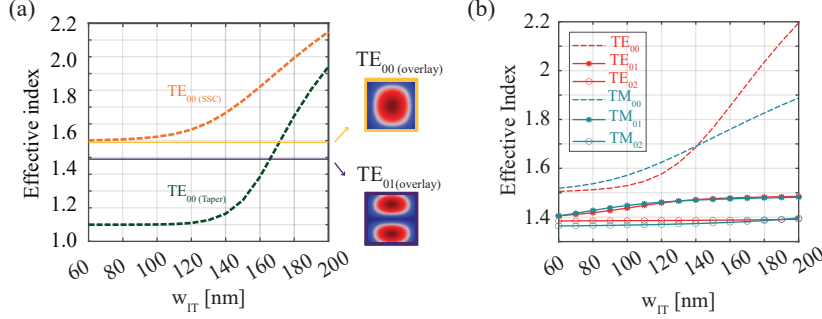


Figure 3.3: Effective refractive index calculation. (a) Calculated effective refractive index of the fundamental TE modes of the GaAs inverted taper $TE_{00}(IT)$ (green dotted lines) and the SSC (orange dotted lines) as a function of the taper width (w_{IT}). The yellow and purple solid lines are effective indices of the fundamental and first order TE modes of the polymer cladding waveguide ($TE_{00}(SSC)$), respectively. Corresponding mode profiles are shown in the insets. (b) Evolution of the effective refractive index of SSC TE and TM modes (fundamental, 1st and second order modes) as a function of waveguide taper width (increasing, inverse to propagation direction)

overlay polymer waveguide with a size matched to the focal spot of a lensed fiber. Unlike tapers without polymers, (Cohen et al., 2013; Galán et al., 2007; Kiršanské et al., 2017) the adiabatic condition is easier to fulfill, resulting in virtually perfect spot-size conversion. Here we focus on the TE modes only, since the QD dipole is exclusively in-plane and thus does not couple to transverse magnetic modes. (Lodahl et al., 2015) The taper angle θ_t is designed to achieve an adiabatic transition into the fundamental mode of the cladding, according to $\theta_t \ll \Delta n_{\text{eff}}$, where Δn_{eff} is the difference between the effective indices between the first two modes of the cladding polymer. The adiabatic taper ensures a gradual decrease of the effective refractive index of TE_{00} to match the low-index overlay epoxy polymer ($n_{Epo} = 1.52$) and suppressing back-reflections in the taper. Figure 3.3a shows the calculated effective index change in the fundamental modes of the SSC (red dotted line) and GaAs inverted taper (blue dotted line) as a function of the taper width (w_{IT}). The two horizontal lines indicate the effective indices of the fundamental and second-order (odd) mode, whose profiles are shown in the inset. The calculated difference $\Delta n_{\text{eff}} \approx 0.1$ requires a maximum taper angle well below 5° . It should be noted that larger mode diameters are in principle achievable with wider polymer waveguides, provided that smaller angles and longer tapers can be accurately patterned and fabricated. In the present work, we have chosen an angle below 1° (taper length L_{IT} around $10 \mu\text{m}$), which is achievable with electron beam lithography and fulfills the adiabatic condition.

The design of the SSC is optimized by three-dimensional (3D) finite-element calculations. Figure 3.2b shows the distribution of the simulated y -component of the fundamental TE mode (E_y) plotted on the central cross-section of the device, and at a wavelength of 930 nm. The power transmitted over the SSC is evaluated using a scattering matrix (S-matrix) formalism to estimate the transmission efficiency of the

SSC η_{SSC} . The efficiency depends on the length of the linear inverted taper L_{IT} and the width of the waveguide at the tip. As mentioned above, the smallest achievable tip in the fabrication process has a width of 60 nm, which is sufficient to achieve negligible mode mismatch (cf. the last two mode profiles in the inset of Figure 3.2a). The transmission efficiency η_{SSC} is plotted in Figure 3.4a as a function of the taper length. Near-unity ($\eta_{SSC} = 98.9\%$) is predicted when $L_{IT} = 15 \mu\text{m}$. Figure 3.4b shows the calculated efficiency for $L_{IT} = 15 \mu\text{m}$ as a function of wavelength at room and cryogenic temperature. No significant deviation from the optimal coupling is observed over a 50 nm bandwidth, indicating that the coupler is very broadband. To avoid excessive bending of the structures after undercut, the samples are designed with $11 \mu\text{m}$ taper length, which results in slightly lower efficiency of $\eta_{SSC} = 94.6\%$.

The SSC transmission efficiency η_{SSC} is the theoretical maximum power transfer that the device would achieve in case of direct face-to-face coupling to a waveguide of same refractive index and mode profile (i.e., neglecting any additional index or mode mismatch related to the coupling). In this work, we have calculated the coupling efficiency for a lensed fiber with $1.3 \mu\text{m}$ mode-field diameter (MFD), which is positioned at a working distance of $4.5 \mu\text{m}$ from the end face of the chip. Such characterization method utilizing lensed fibers introduces additional loss related to the polymer-air-glass interfaces and to the alignment (displacement and angle) of the lensed fiber [the alignment scheme is illustrated in Figure 3.5a]. The plots in Figure 3.5b and 3.5c show the calculated far-field distribution (two-dimensional map and cross-sections, respectively) of the optical mode emerging from the end face of the polymer, which appears nearly Gaussian.

We estimated the mode overlap by a normalized overlap integral between the complex electric field of the waveguide out-coupler ($E_{y,OC}$) and the fiber ($E_{y, \text{fiber}}$) as follows: (Kataoka, 2010; Orobtcouk, 2006; Snyder & Love, 2012)

$$\eta_{\text{Overlap}} = \frac{|\iint E_{y,oc}^* E_{y, \text{fiber}} dy dz|^2}{\iint |E_{y,oc}|^2 dy dz \cdot \iint |E_{y, \text{fiber}}|^2 dy dz}, \quad (3.1)$$

where the fundamental TE mode of the out-coupler ($E_{y,oc}$) is computed numerically and the circular Gaussian mode of the single mode lensed fiber ($E_{y, \text{fiber}}$) is approximated by a perfect Gaussian profile with an MFD of $1.3 \mu\text{m}$. When the SSC is perfectly aligned to the focal plane of the lensed fiber the theoretical overlap efficiency is found to be 80.4%, indicating that the square profile of the epoxy waveguide introduces diffraction that is not captured by an ideal lensed fiber. Making wider polymer waveguides and considering the overlap to a size-matched Gaussian profile is expected to mitigate this issue as confirmed by numerical simulations ($> 97\%$ mode overlap for $3 \mu\text{m}$ -wide polymers).

The overlap integral of Equation 3.1 allows us to estimate the alignment tolerance between the out-coupler and the lensed fiber. Figure 3.5d and Figure 3.5e show the coupling efficiency as a function of the lateral and angular fiber offset, respectively. We identify a 3 dB loss in the coupling efficiency for a lateral misalignment exceeding $0.5 \mu\text{m}$ or angular deviations around 25° . In our experiments, the fiber is mounted

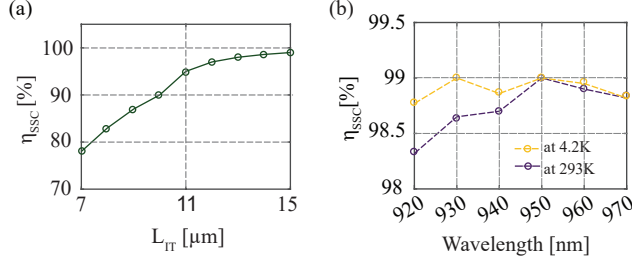


Figure 3.4: Numerical analysis of the SSC efficiency and its bandwidth. (a) The transmission efficiency η_{SSC} is calculated as a function of taper length by 3D FEM simulations. The transmitted power is calculated at the output port of the coupler. (b) Comparison between the simulated transmission efficiencies are at 4.2 K and 293 K over 50 nm wavelength window.

on nano-positioners with a sub-nm positioning resolution and 5 nm repeatability, which suggests that the lateral misalignment is not an issue (see Figure 3.7). Angular deviations, however, are much more difficult to control as they require stages with rotational degrees of freedom. Additionally, the taper itself can slightly bend during cool-down due to thermal stress. We estimate that our total angle misalignment does not exceed 10° by inspecting the setup with an optical microscope.

An additional loss term is caused by the reflection at the facet of the epoxy polymer out-coupler. We estimate them using the Fresnel coefficient for a polymer-air interface at normal incidence, resulting in approximately 4% loss ($R_{\text{polymer}} = 4\%$). In summary, the theoretical chip-to-fiber coupling efficiency of the SSC has been estimated numerically to be 73% and is given by the product of the taper transmission efficiency $\eta_{SSC} \simeq 94.6\%$, the transmission across polymer-air interface $T_{\text{polymer}} = 1 - R_{\text{polymer}}$ (96%), and the mode matching to a fiber, which in the ideal case is $\eta_{\text{Overlap}} = 80.4\%$.

3.4 CHARACTERIZATION OF COUPLING EFFICIENCY

The sample is mounted on a piezo stack and cooled down to 4.2 K in a bath cryostat. A lensed fiber is mounted next to the sample on a separate piezo stack, fed through the cryostat using a hermetic sealing, and finally spliced to another single-mode fiber and interfaced to the detection setup (see Figure 3.6). A microscope objective is used to excite the QDs from the top, and the photoluminescence (PL) is collected on the fiber by manually optimizing its alignment. We investigated a QD placed in a nanobeam waveguide, as shown in Figure 3.8a, terminated by an out-coupler. The QD line is pumped via above-band excitation using an 810 nm pulsed laser source with a repetition rate of 76 MHz. The QD integrated intensity as a function of the excitation power (from $0.2 \mu\text{W}$ to $40 \mu\text{W}$) is shown in Figure 3.8b. The saturation power $P_{\text{sat}} = 1.78 \pm 0.25 \mu\text{W}$ is extracted at a 95% confidence interval by fitting the peak counts of the QD with the function $I = I_{\text{max}}(1 - \exp(-P/P_{\text{sat}}))$ (solid red line). The spectrum of the QD is

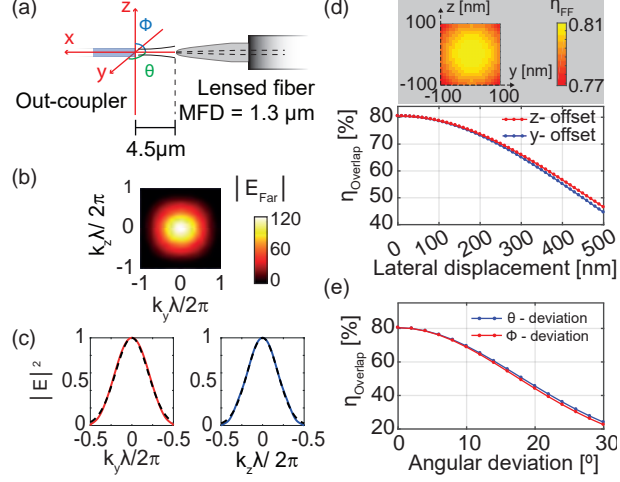


Figure 3.5: Calculated mode overlap efficiency between the out-coupler and a lensed fiber. (a) Schematic of the optimal lateral alignment ($\Delta x = 0$, $\Delta y = 0$) and angular adjustment ($\Delta \theta = 0$, $\Delta \phi = 0$) between the lensed fiber (MFD of 1.3 μm , measured at $1/e^2$ at a working distance of 4.5 μm) and the out-coupler. (b) Simulated far-field radiation pattern of the end-fire out-coupler. (c) Electric field distribution calculated along y-cut (red) and z-cut (blue) of (b), where the black dotted lines are the fitted Gaussian distributions of the lensed fiber in the focal plane. (d) Mode overlap efficiency η_{Overlap} as a function of lensed fiber lateral displacement in the y-direction (red) and z-direction (blue), when the out-coupler is positioned at the working distance of the fiber. The top inset shows the overlapping electric field map in the far field, where the facet of the out-coupler is scanned (± 100 nm from the center in x and y) by the lensed fiber. (e) η_{Overlap} as a function of angular deviation (θ between x and y-axes, ϕ between x and z-axes) in the lensed fiber arrangement.

successively recorded by a cooled CCD camera (spectral resolution ~ 20 pm). Figure 3.8c shows the excitonic line of the QD for an excitation power $P = 1 \mu\text{W}$.

In order to characterize the single-photon nature of the light emitted by the QD, we carried out an auto-correlation measurement using a Hanbury Brown-Twiss setup (Figure 3.9a). The QD is pumped at $0.56xP_{\text{sat}}$ and subsequently filtered with a grating setup (300 pm spectral bandwidth). The filtered signal is split by a 50:50 fiber beam-splitter whose outputs are connected to two fiber-coupled silicon avalanche photodiodes (APDs). A time-tagging module (PicoHarp 300) is used to record correlation events between the two detectors. The result of the auto-correlation experiment is shown in Figure 3.9b, where the coincident counts are plotted as a function of the delay time between the two APDs. The plot reveals a strong anti-bunching at zero time delay, $g^{(2)}(0) = 0.015 \pm 0.002$, confirming the single-photon nature of the QD emission. Figure 3.9c shows the auto-correlation experiment at $1.68xP_{\text{sat}}$ ($3 \mu\text{W}$), where the source generates single photons with a probability of multiphoton emission of $11 \pm 0.3\%$. The data are fitted with two-sided exponentials and the $g^{(2)}$ value is obtained by dividing the area of the central peak to the peak around a time delay of 250 ns on account of blinking over short timescales. The purity of the source could be improved even further by fabricating the structures on a sample with lower QD density or by

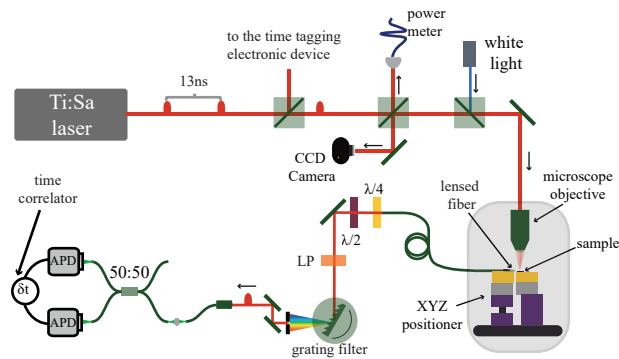


Figure 3.6: Experimental setup. (a) Schematic illustration of the optical setup containing the excitation laser. The laser (mode-locked Ti:Sa pulsed laser source) is split to different paths via a combination of half-wave plates (HWP) and polarizing beam splitters (PBS). For time-resolved measurements, the trigger photo-diode (PD) records the arrival time of the excitation pulse. The laser is coupled to a polarization-maintaining fiber and sent to the cryostat. (b) On top of the cryostat, a breadboard bears the necessary optics to align and control the laser to excite and image the sample. (c) Inside view of the spectrometer. A flip mirror directs the diffracted signal either to a CCD for spectral measurement or a slit + APD for time-resolved measurement. (d) Home-built filtering setup. The signal is diffracted by a grating and coupled to a fiber which gives a filter bandwidth of 300 pm. The signal is split by a 50:50 fiber beam splitter and sent onto two fiber-coupled APDs for auto-correlation measurement. (e) Efficiency of the detection setup in the first generation of measurement. (f) Efficiency of the detection setup in the second generation of measurement with optimized components.

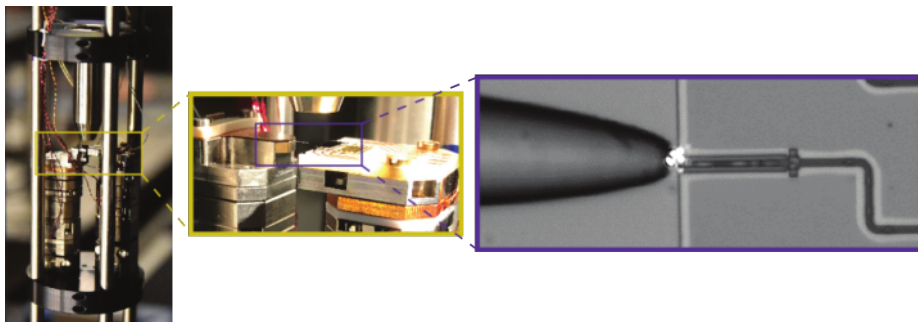


Figure 3.7: Cryostat Layout. (a) The sample and fiber are mounted on nano-positioners with sub-nm positioning resolution. (b) Close up of the sample-fiber mounting stage. (c) Optical micrograph of the device with a 11 μm -long taper with 16 μm -long overlay polymer cladding.

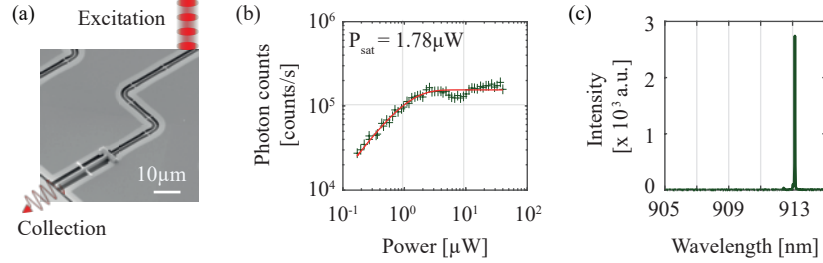


Figure 3.8: Single-photon photoluminescence measurements. (a) Scanning electron microscope image of the nanobeam waveguide terminated by the SSC. The QD coupled to the waveguide is excited vertically by the pump laser while photons are collected horizontally from the SSC at the edge of the sample. (b) The saturation power of the QD is characterized by the same excitation scheme leading to a saturation power of $1.78 \mu\text{W}$. (c) Photoluminescence of a QD emitting at 913.1 nm under above-band excitation with a pulsed laser. The inset shows the SEM image of the structure.

adopting different excitation schemes such as p-shell or resonant excitation (Somaschi et al., 2016; Thyrrstrup et al., 2018).

3.4.1 Single-photon out-coupling efficiency from the device

The recorded single-photon emission rate from the QD can be further scrutinized in order to experimentally extract the efficiency of the SSC. We record in total a single-photon count rate of 167 kHz on the APD at the saturation. Based on this number we can extract the photon rate inside the fiber to be $5.84 \pm 0.01 \text{ MHz}$ by accounting for the measured transmission efficiency of the various components of the detection setup: fiber splicing and mating sleeves: $T = 32 \pm 2 \%$, grating setup efficiency: $\eta_F = 30 \pm 1 \%$ and, detector quantum efficiency $\eta_{\text{APD}} = 30 \%$. Consequently, the overall setup efficiency is $2.9 \pm 0.3 \%$. Since the QD is triggered at a repetition rate of 76 MHz the overall source efficiency is found to be $7.7 \pm 0.08 \%$, which is defined as the probability that a photon is collected by the fiber given that a QD is triggered. All on-chip and off-chip efficiencies are summarized in the Table (3.1).

To get to the chip-to-fiber efficiency of the SSC we estimate the rate of single photons present inside the GaAs waveguide and compare that to the above measured value of single photons in the fiber. Furthermore, since above-band excitation is applied, also additional exciton levels are occupied during excitation notably the nonradiative dark excitons leading to an effective preparation efficiency of the bright radiative exciton of $\eta_{\text{QD}} \sim 50 \%$ (Johansen et al., 2010). Furthermore, since the waveguide is two-sided only half of the coupled photons are collected leading to $\beta_{\text{directional}} \sim 40 \%$ based on the calculated β -factor (Dreeßen et al., 2018). Finally propagation loss in the $117 \mu\text{m}$ -long nanobeam waveguide amounts to $\eta_{\text{nb}} = 81 \pm 2 \%$ (Papon et al., 2019), leading to an overall photon rate at the entrance of the SSC of $5.84 \pm 0.01 \text{ MHz}$.

Based on the above analysis, we can quantify the overall efficiency of the fiber-coupling comprising of both the SSC and the aligned tapered fiber. We estimate the

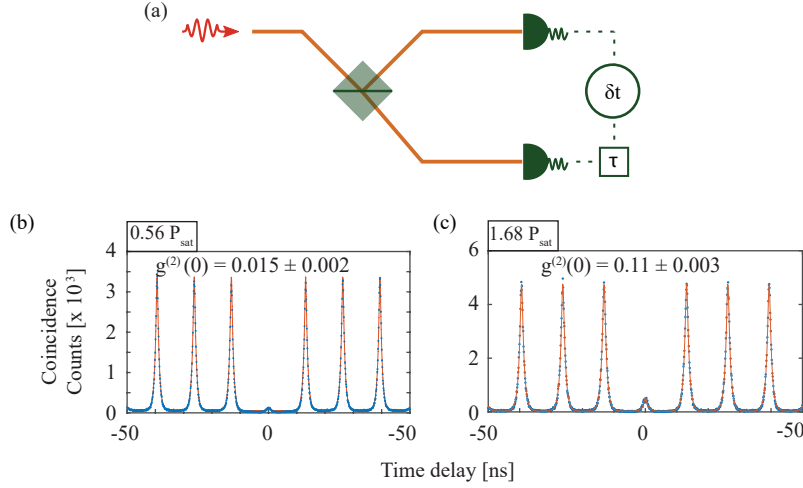


Figure 3.9: Measuring the single-photon purity of the out-coupled light. (a) Experimental setup for measuring the auto-correlation with. Hanbury Brown Twiss (HBT) setup shows photon being detected after passing through the 50 : 50 beam splitter (BS). (b) Auto-correlation measurement for the QD emission line in (Fig. 3.8.c) is taken at $1 \mu\text{W}$ ($0.56 P_{\text{sat}}$). The coincidence counts histograms are fitted with exponential decays in order to extract $g^{(2)}(0) = 0.015 \pm 0.002$. (c) Auto-correlation measurement for the QD emission line in (Fig. 3.8.c) is taken at $3 \mu\text{W}$ ($1.68 P_{\text{sat}}$). The coincidence counts histograms are fitted with exponential decays in order to extract $g^{(2)}(0) = 0.11 \pm 0.003$.

chip-to-fiber coupling efficiency to be $\sim 48\%$. This value should be compared to the theoretically calculated coupling efficiency of 73% in order to extract the coupling efficiency of the SSC. The minor discrepancy between experimental estimate and theory can likely be attributed to the angular deviations in the alignment of the fiber or fabrication imperfections influencing the taper tip.

* * *

We reported the design, fabrication, and characterization of a suspended spot-size converter for the end-face coupling of single photons from QDs. The device holds great promise as a building block for scalable quantum information processing and for the realization of photonic quantum networks. The measured efficiency of $\sim 48\%$ is currently limited by the characterization method, which is based on a lensed fiber. Direct coupling to a second chip could lead to better alignment and would increase the single-photon rate further. Moreover, the design allows for the straightforward scaling of the number of couplers to multiple ports, thereby enabling multi-photon protocols. The efficiency of the device could readily be improved further by: (i) the termination of the waveguide on one side with a mirror will double the photon collection efficiency; (ii) integrating quantum dot embedded photonic crystal waveguides with the presented spot-size converter can boost the single-photon generation efficiency

I	
Theoretical transmission efficiency η_{SSC}	94.6 %
Theoretical polymer transmittance T_{polymer}	96 %
Theoretical mode overlap efficiency η_{Overlap}	80.4 %
Theoretical coupling efficiency	73 %
II	
APD count rate	0.167 MHz
Detector efficiency η_{APD}	30 %
Spectral filter efficiency η_{F}	30 ± 1 %
Collection optics efficiency T	32 ± 2 %
Single-photon rate at the lensed fiber	5.84 ± 0.01 MHz
III	
Laser repetition rate	76 MHz
Preparation efficiency η_{QD}	~ 50 %
Waveguide $\beta_{\text{directional}}$	~ 40 %
Nanobeam transmission efficiency η_{nb}	81 ± 2 %
Single-photon rate at the SSC input	~ 12 MHz
IV	
Chip-to-fiber coupling efficiency	~ 48 %

Table 3.1: Transmission efficiencies and performances of the single-photon source out-coupled to a lensed fiber via the SSC. Part I: theoretical coupling efficiency of the spot-size converter is a product of the SSC transmission efficiency (based on 3D FEM simulations), transmission efficiency of the polymer overlay waveguide as a result of reflection losses due to the Fresnel reflectivity at the cladding facet, mode overlap efficiency at far-field. Part II: off-chip efficiencies for detecting, filtering, collection optics. Part III: on-chip efficiencies of the QD excitation and single-photon transmission. Part IV: experimentally calculated chip-to-fiber coupling efficiency.

to near-unity; (Arcari et al., 2014) (iii) resonant excitation of the QD could improve the preparation efficiency to unity; (iv) developing longer tapers on the waveguide and performing direct end-face coupling to a cleaved fiber with matched mode-field diameter would increase the SSC efficiency further up to $> 95\%$. It is expected that any alignment imperfections of the fiber could be overcome chip-to-chip or chip-to-fiber coupling using the SSCs. For instance the SSC is readily applicable in a hybrid approach to quantum-information processing using two different photonic chips, where one is a source chip delivering deterministic photonic qubits and the other is a processing chip implementing, e.g., a complex quantum algorithm.

CHAPTER



IN-PLANE RESONANT EXCITATION FOR PLUG-AND-PLAY SINGLE-PHOTON DEVICES

The work presented in this chapter demonstrates a tailored, planar nanophotonic circuitry that enables in-plane, waveguide-based, deterministic pulsed resonant optical excitation of QDs. The introduced single-photon source device enables the generation of highly pure and indistinguishable single photons with a stable performance over long operation times. Key factors for enabling the waveguide-assisted resonant excitation are explained. Next, the important figures-of-merit that characterize the performance of the single-photon source device are introduced. Part of the results presented in this chapter are published in Uppu, Eriksen, et al., 2020.

4.1 WAVEGUIDE ASSISTED QD EXCITATION AND EFFICIENT EMISSION COLLECTION

The use of quantum dots embedded in the nanophotonic waveguide to realize scalable and deterministic single-photon sources was previously introduced in Chapter 1 and 3 (Lodahl et al., 2015). To perform on-chip scalable quantum experiments, coherent single-photon emission from a bright source is a requirement (Kim et al., 2020). For preventing decoherence processes, the following three primary figures-of-merit have been improved: **(1)** the purity of the single-photon emission (for non-resonant excitation $> 99.5\%$ and for resonant excitation 98.5%) (Kiršanskė et al., 2017; Uppu, Pedersen, et al., 2020), **(2)** the coupling efficiency of the single-photon emission into the desired propagation mode ($\geq 98.4\%$) (Arcari et al., 2014) and **(3)** the degree of the single-photon indistinguishability of subsequently emitted photons from the QD ($\leq 98.4\%$) (Pedersen, 2020; Uppu, Eriksen, et al., 2020; Uppu, Pedersen, et al., 2020). Moreover, transform limited optical single-photon emission have been presented in diode structures (with linewidth $\geq 2 \mu\text{eV}$) (Löbl et al., 2017) and integrated with the nanophotonic structures with electrical gating (where the linewidth is reduced to 460 GHz) (F. Liu et al., 2018;

Pedersen et al., 2020; Thyrrstrup et al., 2018), such that a QD can emit a long string of indistinguishable single photons (Uppu, Eriksen, et al., 2020; Uppu, Pedersen, et al., 2020).

Another requisite is the efficient implementation of resonant excitation of optical transition. However, this is particularly challenging as it requires strong suppression of the residual laser pump. Often the quantum dot is excited out-of-plane, directly above the QD and this approach has been used for quasi-resonant excitation, which is a scheme that limits the photon indistinguishability. Such schemes result in employing the same spatial mode for exciting the QD and collecting the single-photon emission. The out-of-plane excitation has limitations as it requires the excitation laser background to be suppressed while realizing efficient collection of the single-photon emission. In order to overcome this constraint, methods have been developed to suppress the residual pump laser, such as collecting the emitted photons in an orthogonal polarization state to the excitation polarization, commonly used for the resonant excitation of QDs embedded in microcavities and micro pillars. (F. Liu et al., 2018; Loredó et al., 2016; Somaschi et al., 2016; H. Wang et al., 2016). However, such a cross-polarization excitation-collection method reduces the brightness of the extracted photons to $\sim 50\%$, the excitation polarization is maximally oriented 45 degree to the dipole, and the collection polarization is cross-polarized to the excitation. Recent works with elliptical micropillars achieved high laser suppression without polarization filtering, but have the drawback of demanding very high excitation power (H. Wang, He, Chung, Hu, Yu, Chen, Ding, Chen, Qin, Yang, et al., 2019a). Alternatively, to eliminate collected scattered laser light, QDs embedded in planar nanostructures can be excited from the top through out-of-plane weak radiation modes and single photons collected through the waveguide mode (Ates, Ulrich, et al., 2009; Ates, Ulrich, et al., 2009; Huber et al., 2020; Melet et al., 2008; Monniello et al., 2014; Thyrrstrup et al., 2018). However, this scheme already requires strong excitation pulses that may induce decoherence and noise from residual background leakage. Furthermore, the top resonant excitation of QDs in such devices will limit scalability with respect to building a circuitry that excites multiple QDs in parallel for performing larger scale experiments. The reason being that the excitation scheme of pumping multiple identical QD simultaneously requires many finely aligned, polarization-controlled, free-space laser beams.

In this chapter, we introduce a scheme for the pulsed excitation of a QD by directly injecting laser light through the waveguide modes in the nanostructure, which allows tailoring the excitation process by spatially separating the collection and excitation modes.

4.1.1 Working Principle of the Device

The basic principle of the device for waveguide-based resonant excitation of the QD emission is illustrated in Figure 4.1.

An SEM image of the fabricated nanophotonic circuit (Fig. 4.1.a.) studied in this chapter presents the device components. The structure is formed by multiple essential components: **(1)** three high-efficiency shallow etched grating couplers with a reported

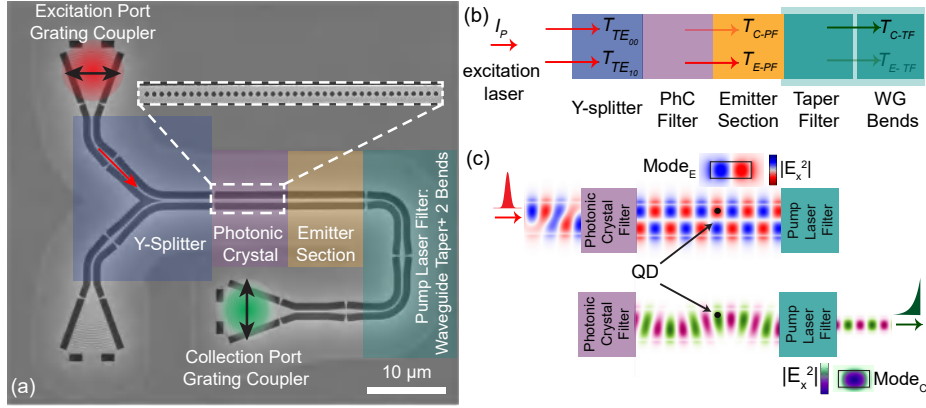


Figure 4.1: Waveguide-assisted excitation of a QD showing the operational principle of the device. (a) Scanning electron micrograph of the fabricated single-photon-source structure. The red spot highlights the excitation port, where the pump laser in-couples through to the shallow etched grating couplers. Light propagates through the symmetric Y-splitter and generates the orthogonal modes (TE_{00} and TE_{10}). A nanobeam photonic crystal (the inset is the zoomed-in image to show the lattice of 40 air holes) filters out the even modes and transmits predominantly the odd mode (TE_{10} , excitation mode) into the emitter section. The combination of tapered waveguide and waveguide bendings act as the pump laser filter, which further suppresses the odd mode of the pump. The bottom-left grating assists fine alignment of in-coupling the laser beam by monitoring the out-coupled light reflected back from the photonic crystal. (b) The schematic shows the essential operational sub-components of the nanophotonic circuit. The transmission of the input laser across the operational sections coupled into the two waveguide modes TE_{10} (for excitation; mode E) and TE_{00} (for collection; mode C) are highlighted. The transparency of the arrows shows the transmission efficiency of the modes, where the brighter stands for more efficient transmittance. (c) Top: Y-splitter prepares the excitation pulse as a superposition of the two orthogonal spatial waveguide modes. Modes C is subsequently filtered away by PhC filter and mode E is used to excite a QD positioned off-center in the emitter section. Bottom: The QD emits into the waveguide by exciting the superposition of modes E and C . The subsequent mode filter rejects emission into mode E and single-photon emission coupled to the mode C exits the device.

efficiency of $> 65\%$ (Zhou et al., 2018) for in-, out-coupling and for fine alignment of the laser, (2) Y-splitter for launching the excitation laser, (3) photonic crystal (PhC) filter for selectively transmitting the QD excitation mode, (4) dual-mode waveguide for accommodating the emitters (QDs) for efficient excitation and collection, (5) adiabatically tapered waveguide section, followed by 90° waveguide bends for extinguishing the laser pump. The fundamental goal of tailoring such a device is to selectively choose the mode for QD resonant excitation, which leads to the generation of highly coherent and indistinguishable single-photon emission, and to suppress the residual laser light in the collection.

Figure 4.1b. explains the schematic principle of the device without including the grating couplers. Laser light is injected from one of the symmetric output branches of the Y-splitter (see Fig. 4.1a., where in-coupling happens from the top-left branch) that is a 250 nm wide single-mode waveguide. The Y-splitter is designed to be a 50/50 power divider. Due to the reciprocity principle, the in-coupled light generates the

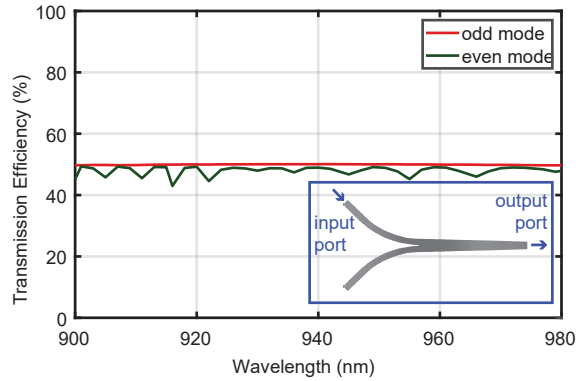


Figure 4.2: Y splitter FEM model. (a) Simulated transmission efficiency as a function of wavelength for the Y splitter, where input and output ports are shown in the inset. One of the symmetric branches is used to feed the excitation laser and the excitation laser is prepared at the output waveguide. The input branches are formed with an 95° splitting angle and are identical with a width of 250 nm. The output waveguide width is 500 nm and tapered to 450 nm over $5\ \mu\text{m}$.

superposition of two orthogonal spatial modes with even symmetry; TE_{00} and odd symmetry; TE_{10} in the dual-mode waveguide section. The dual-mode waveguide branch is tapered from 500 nm to 450 nm. Finite-element-method simulation of the Y-splitter (see Fig. 4.2.) indicates that 50% of the light is transmitted into the odd mode, and 47% is transmitted into the even mode (average transmission efficiency between 900-980nm wavelength band). The remaining 3% is reflected back to the symmetric branch of the Y-splitter and losses due to the scattered light.

The next element in this design is the PhC mode filter, which selectively transmits the odd mode into the waveguide region, labeled as emitter section in Figure 4.1. As the allowed odd mode is prepared for exciting the QDs, we name the excitation mode as mode E in this chapter. Ideally, when the PhC filter is lossless and built by an infinite amount of holes, the even mode propagation is rejected. Accordingly, the odd mode for exciting the QDs (mode E) is generated with an excellent mode purity, which is then theoretically improving the laser extinction in the collection.

The band diagram of the designed nanobeam PhC of holes is plotted in Figure 4.3.a., where k_z is the projected wavevector for propagation direction of the nanobeam waveguide with 170 nm GaAs slab thickness, 70 nm hole radius (r), 210 nm lattice constant (a) of 20 photonic crystal of holes. The solid curves below the light line (gray area) constitute the propagating modes confined to the PhC nanobeam waveguide and are color-coded according to their transverse spatial symmetry (insets show the electric field mode profile). The gray shaded wavelength region (900 nm to 1025 nm) shows the stop gap of the PhC for even modes, where only a partial transmission of the mode of interest with odd mode symmetry is allowed. The effective refractive index n_{eff} of the first two guided modes of the filter are plotted in Figure 4.3.b.. for the mode C (TE_{00})

and mode E (TE_{10}) with green and red respectively as a function of the waveguide width.

Figure 4.3.c, is the finite-difference-time-domain (FDTD) simulation results showing the transmission property of QD excitation showing that the PhC filter transmits a fraction T_E of the mode E and T_C of the mode C . It is seen that the transmission into the excitation mode (mode E) is around 50% within the desired wavelength region between 920 to 960 nm. Mode C is only evanescently coupled through the PhC at this stop band. Close to the stop gap center, the transmittance of mode E is remarkably stronger than mode C . The mode C is extinguished by more than a factor of 10^4 , which ensures dominantly the odd mode propagation to the QD position. Due to the reproducibility limit and imperfections in the fabrication process of the photonic crystal nanobeam, the even mode suppression can be limited. To avoid that, the designed nanobeam is fabricated by placing 40 holes instead.

Besides the efficient preparation of the laser excitation, another important factor for achieving the optimum operation condition for resonant excitation is the QD position in the dual-mode waveguide, which affects the coupling of the QD to the waveguide mode (that is quantified through the β -factor). At the emitter section, the quantum dot is located off-axis in the dual-mode waveguide as it is illustrated at the emitters section of the Figure 4.1c. Here, the model counts on a long emitter section with a high density of QDs. The dual-mode waveguide can host two guided modes (mode E and mode C), which are exhibiting transverse even and odd symmetry, respectively as it is shown at the inset in Figure 4.3.. As the two spatial modes at the emitter section are orthogonal to each other, we can excite the quantum dot via mode E and collect the single-photon emission in mode C . Mode E propagates unperturbed until the input of the tapered filter section. The QD emission is unidirectional and propagates in the mode C given that the photonic crystal is a nearly perfect mirror ($>99.99\%$ reflectivity) for single photons coupled to the mode C .

Eventually, before the collection of the single photons, the final filtering operation (pump laser filtering in Fig. 4.1.b.) ensures to extinguish the incident laser (mode E) before collection. The dual-mode waveguide with 450 nm width is adiabatically tapered over a $5\ \mu\text{m}$ length into a single-mode waveguide with 200 nm width for efficient propagation of the single-photon emission (mode C). Mode E becomes leaky at the taper filter section and can be extinguished. The transmission of modes E and C in the taper section are presented by T_{E-Tf} and T_{C-Tf} , respectively. To avoid a potential non-adiabatic scattering, two consecutive sharp waveguide 90° bends (with $3.5\ \mu\text{m}$ of radius) assure suppression of the excitation pump laser in the collection. Subsequently by employing the out-coupling grating coupler at the bottom right in Figure 4.1.a. the single-photon emission is collected and then coupled into an optical fiber.

To sum up the operational characteristics, the shown model optimizes the PhC filter to predominantly transmit the excitation mode (T_{E-Pf}). Besides, the taper filter section (with bendings) is designed to boost the transmittance of the collection mode (T_{C-Tf}) to near-unity with 99.85% calculated efficiency. Despite that, to allow the extinction of the laser excitation mode, the QD position at the emitter section plays an important role in terms of efficient pumping of the QD and collecting of the single-photon emission.

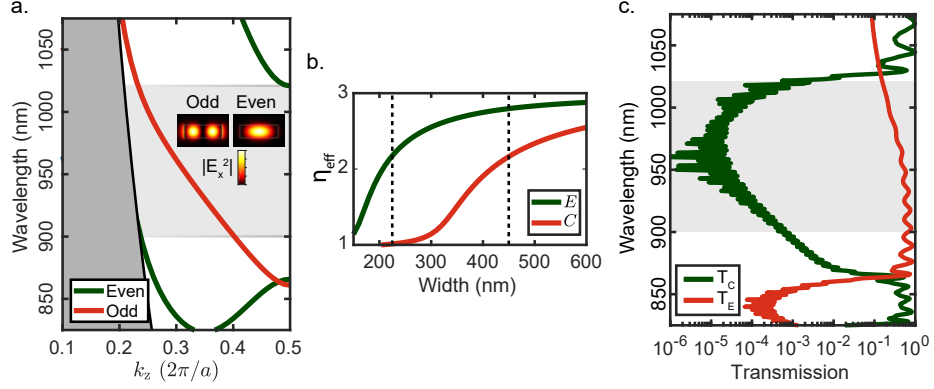


Figure 4.3: Photonic crystal and nanobeam waveguide simulations. (a) Band structure of the photonic crystal waveguide with $r = 70$ nm, $a = 210$ nm and $w = 70$ nm where the guided modes below the light cone (gray area) are shown as solid lines. The photonic crystal forms a bandgap for even modes (indicated by the light shaded gray region). (b) The effective refractive index n_{eff} as function of width for the guided modes; mode C (TE_{00}) and mode E (TE_{10}). The dashed line indicates the two widths used for excitation (450 nm) and in the collection waveguide (200 nm). (c) Calculated transmission coefficients through the 20 holes photonic-crystal section between even/odd modes. Within the bandgap, the transmission of mode C is strongly suppressed whereas mode E is transmitted.

We will have a closer look on that subject in Section 4.2.2. In addition, density of the QDs in the wafer and correspondingly at the emitter section plays an important role in terms of device operation. The sample is fabricated on a wafer with a QD density of $\approx 10/\mu\text{m}^2$ and the dual-mode waveguide has a length (width) of $40 \mu\text{m}$ ($0.45 \mu\text{m}$) forming the emitter section.

The device is designed to be formed on an air-suspended GaAs membrane (180 nm thick), containing a self-assembled InAs QD layer. The QDs are grown with a tailored molecular beam epitaxy method, eliminating the electron wetting layer states (Löbl et al., 2019), embedded in a p - i - n diode. The solid-state environment around the QD is regulated by applying an electric field on our sample via electrodes in this diode structure, to reduce the charge noise, controlling the charge state, and Stark tuning of the emitter that are required for the resonance fluorescence performance. In parallel, a high-quality single-photon emission can be achieved in terms of high level of indistinguishability, as have employed a p - i - n diode heterostructure for building the device. The device under investigation is fabricated by our co-researcher Ying Wang. The outline and the fabrication of the gated nanostructure is explained in Appendix B.

4.2 PERFORMANCE FIGURE OF MERITS OF THE DEVICE

4.2.1 Laser Suppression

In this section, the device performance is investigated in terms of single-photon emission probability and single-photon coupling efficiency. While the goal of the studied

device is to implement the waveguide assisted (in-plane) resonant excitation on the electrically contacted QD with a pulsed laser, the excitation laser suppression (T_p) is a significant parameter to inspect. It is of importance because the collection of resonance fluorescence with a high purity level depends on how well the resonant laser light can be suppressed, so that the single-photon stream does not get polluted with laser photons.

The residual excitation laser suppression performance is evaluated by comparing the transmitted laser intensity $T_p(\lambda)$ through two identical devices, one of which is fabricated with the PhC mode filter and the other one is formed as a reference device without the filter section.

$$T_p(\lambda) = \frac{I_{\text{Filter}}(\lambda)}{I_{\text{Ref}}(\lambda)}. \quad (4.1)$$

The other on-chip components (grating in- and out-couplers, Y-splitter, waveguide tapers, waveguide bends) are designed with identical parameters and fabricated together on the same chip.

The continuous wave (CW) laser with tunable wavelength is in-coupled through the excitation grating (see in Fig. 4.1.a.) and after passing through the device, transmitted laser is out-coupled through the collection grating. While tuning the laser wavelength from 914 nm to 965 nm (with 0.05 nm step size), the photon counts are recorded directly at the fiber-coupled SNSPD. To avoid any charge state population, the QDs is turned off by applying a gate voltage of 1 V during the wavelength scan. The transmittance of the laser excitation is characterized on 20 different devices with PhC filter. The suppression of the laser mode is measured as $T_p < 10^{-4}$ at each device for approximately 5 nm wavelength window. Here, a full-scale experimental investigation is provided focusing on one specific device. Figure 4.4.a plots the detected intensity (violet line) as a function of wavelength for the device under study. The intensity spectrum of the the reference sample (circuit without a PhC filter) is plotted in yellow for comparison. To assure an adequate dynamic range for the transmitted laser signal, the transmission spectra are recorded at two laser powers (at 50 nW and 10 nW) for the device with the PhC filter and the reference device.

The measured laser suppression is compared to the ideal device performance in Figure 4.4.b. The $T_p(\lambda)$ is calculated with FDTD methods by applying a wavelength sweep for a device with 20-hole PhC nanobeam with a finite length. The simulated transmission spectrum is plotted with green. The extracted transmittance of the excitation laser $T_p(\lambda)$ is plotted with red in Fig 4.4.b. The experimental transmission scan shows two sharp transmission dips at 948 nm and 964 nm. The measured $T_p \sim 10^{-5}$, which is the ratio between the counts normalized to the power of the laser. The typical QD emission band of this sample is 940 – 950 nm, and we therefore continue our further study of the device at the 948 nm transmission dip. The deviations between the simulated and measured device performance are due to the fabrication imperfections of a periodic array of holes and (detailed information on the fabrication imperfections can be found in Chapter 2). Nonetheless, we can see that in certain wavelength bands measured device performance is consistent with the ideal device. To achieve

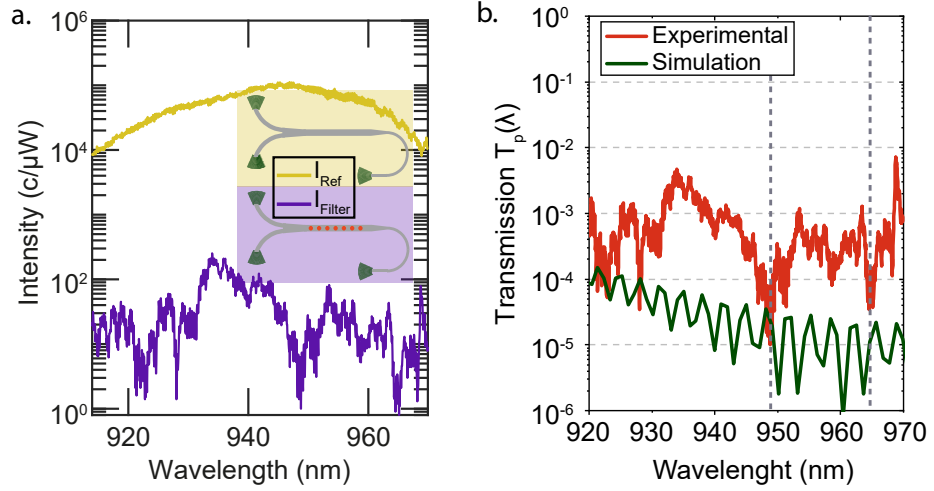


Figure 4.4: Intensity transmission measurements and the laser suppression performance. (a) The measured transmitted laser intensity spectrum is compared for two nominally identical devices, one of them is preparing the in-plane excitation laser by selective transmission through the PhC filter and the second one transmitting the dual-mode waveguide modes in the absence of the PhC filter (violet and yellow highlighted insets showing the simple sketches respectively). The measured counts are normalized to the same power and time and plotted as a function of the excitation laser wavelength. At both devices excitation and collection gratings (shown in Fig. 4.1a.) are used for in- and out-coupling, respectively. (b) The simulated (green plot) and measured (red plot) laser suppression performances are shown on the transmission spectrum. The calculated laser suppression of the simulated device is shown with green.

high performance over a broader wavelength range, we can improve the design and accordingly the fabrication yield, which will be introduced in the Chapter 5.

4.2.2 Single-Photon Impurity

The resonant excitation of the QD is performed with a broadband pulsed laser with ~ 100 GHz bandwidth. A pulse stretcher is used to reduce the spectral bandwidth of the laser to ~ 22 GHz by in turn stretching the pulse in time, as it is described in Section 4.3. With laser bandwidth engineering, the QD transition can be excited more efficiently, as the fraction of the excitation laser resonant with the QD transition is increased. At the collection path, a temperature-tunable Fabry-Perot etalon with a bandwidth of 3.5 GHz (at FWHM) is employed for spectral filtering. Accordingly, the single-photon emission bandwidth is cut down to 50 pm (at FWHM) that gives a transform limited Gaussian pulse with 26 ps duration. Still, the collected mode from the detection grating consists of a fraction of the residual laser background besides the single-photon emission, due to the laser suppression performance of the device. Accordingly, an essential figure-of-merit is the single-photon impurity (ξ), which is the ratio of the intensity of the residual photons from the excitation laser (I_{rp}) to the

intensity of the emitted single photon (I_{sp});

$$\xi = \frac{I_{\text{rp}}}{I_{\text{sp}}}. \quad (4.2)$$

The residual laser intensity at the collection grating coupler is defined as

$$I_{\text{rp}} = \frac{I_{\text{p}}}{2} (T_{\text{E-PF}}T_{\text{E-TF}} + T_{\text{C-PF}}T_{\text{C-TF}}) \equiv I_{\text{p}}T_{\text{p}}, \quad (4.3)$$

where I_{p} is the input laser intensity. We defined the transmittance of the excitation and collection modes through the photonic crystal and taper filters as $T_{\text{E-PF}}$, $T_{\text{C-PF}}$ (respectively). Likewise, the transmission efficiency of the mode E and mode C through the photonic crystal and taper filters are denoted by $T_{\text{E-TF}}$, $T_{\text{C-TF}}$. Figure 4.1.b. describes schematically the modes' propagation. At the input of the PhC filter, the excitation laser is coupled to the modes E (QD excitation mode) and C (single-photon collection mode) nearly equally with ($T_{\text{TE}_{10}} \approx T_{\text{TE}_{00}}$) based on the design of the Y-splitter around the operation wavelength (947 nm) described in Section 4.1. The photonic crystal filter allows the propagation of the mode E with $T_{\text{E}} \approx 1$ transmission efficiency and strongly suppresses coupling to the mode C ($T_{\text{C}} \approx 10^{-5}$ - 10^{-6}). The excitation mode E is transmitted until the input of the taper filter section without any perturbation. Likewise, the emitted single photon that are coupled to the mode C propagates unperturbed until the taper. The taper filter extinguishes the mode E $T_{\text{E-f}} \approx 10^{-6}$ - 10^{-7} and transmits the mode C $T_{\text{C-f}} \approx 1$.

When the QD is excited below its saturation power and when the dephasing effects are disregarded, the intensity of the single-photon emission is proportional to the intensity of the excitation laser; $I_{\text{sp}} \propto I_{\text{p}}$. Accordingly, under the weak excitation I_{sp} is expressed as

$$I_{\text{sp}} = \left(\frac{I_{\text{p}}}{2}\right)T_{\text{E-PF}}\beta_{\text{E}} (\beta_{\text{C}}T_{\text{C-TF}} + \beta_{\text{E}}T_{\text{E-TF}}) + \left(\frac{I_{\text{p}}}{2}\right)T_{\text{C-PF}}\beta_{\text{C}} (\beta_{\text{C}}T_{\text{C-TF}} + \beta_{\text{E}}T_{\text{E-TF}}), \quad (4.4)$$

where β_{E} and β_{C} are the photon β -factors (Arcari et al., 2014). β_{E} is the coupling probability of the excitation mode (mode E) to the emitter and it defines the probability of the QD to interact with a pump photon. Besides, the probability of the QD single-photon emission coupling into the waveguide collection mode (mode C) is expressed by β_{C} . The $T_{\text{E-PF}}$ and $T_{\text{C-TF}}$ are assumed to be 1. Since the $T_{\text{E-f}}$, $T_{\text{C}} \ll 1$, the last three terms are not included in the calculation. Accordingly, the resulting collected intensity of the single-photon is

$$I_{\text{sp}} = \frac{I_{\text{p}}}{2}\beta_{\text{C}}\beta_{\text{E}}. \quad (4.5)$$

Now, we can rewrite the impurity ($\xi = I_{\text{rp}}/I_{\text{sp}}$) as in the following

$$\xi \approx \frac{2T_{\text{p}}}{\beta_{\text{E}}\beta_{\text{C}}}. \quad (4.6)$$

Further section on resonance fluorescence (Sec. 4.4), we will evaluate an exact description for the measured ξ .

By definition the collected single-photon impurity ξ can be then directly related to the single-photon purity. The impurity can be written as $\xi = N_{rp}/N_{sp}$, where the detected photon number of the laser background per pulse (N_{rp}) is compared to the number single photons per pulse (N_{sp}). The single-photon purity is evaluated by the measured degree of the second-order coherence $g^{(2)}(\tau = 0) = 2(N_p/N_{sp}) - (N_p/N_{sp})^2$ (Kako et al., 2006). Accordingly, measuring ξ provides a lower bound on the $g^{(2)}(\tau = 0)$;

$$g^{(2)}(\tau = 0) = 2\xi - \xi^2. \quad (4.7)$$

By calculating the characteristics of the device in terms of QD β -factors (β_E and β_C) and T_p , we can predict the device performance based on the expected ξ and $g^{(2)}(\tau = 0)$. The β_E and β_C are highly dependent on the QD position within the waveguide modes, which impacts the ξ value. Figure 4.5.a. illustrates the modes of the emitter section, where the QD embedded on the dual-mode waveguide is excited by the first-order mode (mode E) and strongly coupled to the fundamental mode (mode C), while having a weak coupling to the mode E . The simulated values of β -factors are plotted as a function of QD position offset from the waveguide center in propagation direction is shown in Figure 4.5.b.. To achieve the optimal coupling to both waveguide modes for the excitation and emission, we need to make a compromise. For maximum coupling to β_C , QD location is calculated to be at the waveguide center, however, at this position $\beta_E \sim 0$ which means that the QD can not be pumped by the excitation laser in the mode E .

In Figure 4.5.c. the impurity is plotted at different QD locations in the waveguide, for the device with a measured laser suppression of $T_p = 2 \cdot 10^{-5}$. From the explained analysis for the optimal performance based on the β -factors and T_p , we can choose the optimal QD position that minimizes the photon impurity ξ and maintains a high β_C and allows QD to be pumped with an adequate β_E , simultaneously. When the QD is located with $< 10\text{nm}$ offset from the waveguide center, we can see that single-photon can couple to the mode C with a high coupling efficiency of $\beta_C > 0.9$ (where $\beta_E < 0.08$), which results in an impurity of $\xi \simeq 5 \cdot 10^{-4}$. Accordingly, a highly pure single-photon emission is predicted $g^{(2)}(0) \simeq 10^{-3}$. For higher-level single-photon purity, we need more efficient QD excitation mode preparation and single-photon collection. To do that, we need a more optimal device design that can allow further suppression of the collected laser, which is presented in Chapter 5.

Moreover, by including deterministic fabrication techniques to form the nanophotonic circuit around the emitter (Pregolato et al., 2020a) and improving the fabrication imperfections (to improve in-/out-coupling efficiency and PhC filter), a higher fidelity device performance can be achieved.

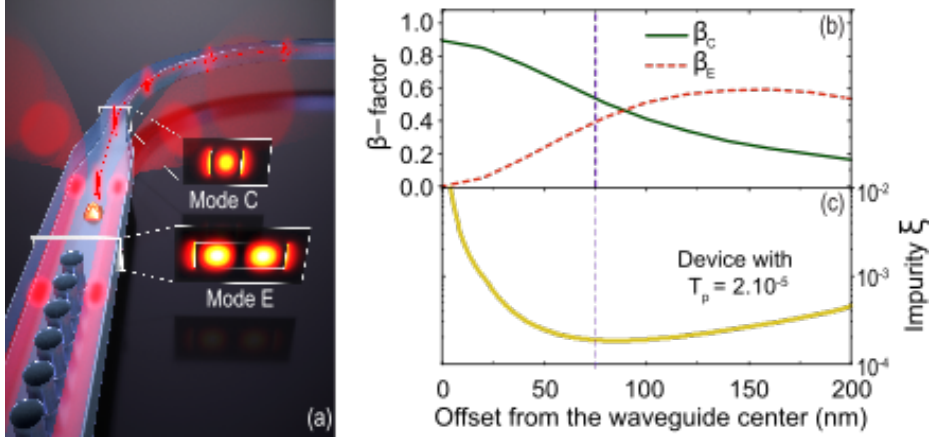


Figure 4.5: Single-photon device performance prediction. (a) Illustration of the modes at the emitter section, where laser pump photons are propagating in mode *E* and single-photon emission is collected in mode *C*. (b) Simulated β -factors for the QD *x*- oriented dipole coupling into the two guided modes (mode *E* and mode *C* plotted) as a function of the position of the QD, where the dashed line with the violet color indicates the ideal device performance case. (c) Calculated simple photon impurity ξ with an experimentally established laser suppression (T_p) of $2 \cdot 10^{-5}$. Figure is adapted from the Ref. (Uppu, Eriksen, et al., 2020).

4.3 OPTIMIZED EXPERIMENTAL SETUP

In the previous sections, we explained the concept of a tailored device for waveguide assisted excitation of a QD and we pointed out its performance figures of merit for high-purity single-photon generation. By optimizing the design and fabrication methods, we have demonstrated that we can minimize the losses associated with the nanophotonic device and suppress the residual excitation laser. Optimization of the device leads to an enhanced single-photon coupling efficiency, along with higher values of single-photon purity and degree of photon indistinguishability. As much as the nanophotonic circuit, the optical experimental setup plays a significant role for realization of the plug-and-play source. We need to optimize the experimental setup to avoid losses and any additional noise that can affect the single-photon collection and its long-term stability. The optical components used in excitation and collection require a careful characterization and the setup needs to be optimized, for best performance.

Figure 4.6 shows a sketch of the optical setup, used for excitation of the QD and collection of the single-photon emission. The sample is mounted on nanopositioners (XYZ) at the bottom of a dipstick. The dipstick is immersed in a closed-cycle cryostat that operates at 1.6K. Liquid helium cryogenic temperatures are required to damp phonon noise, influencing the single-photon emission (Tighineanu et al., 2018). The cryostat has both electrical and optical access to allow electrical tuning and optical manipulation of the QDs.

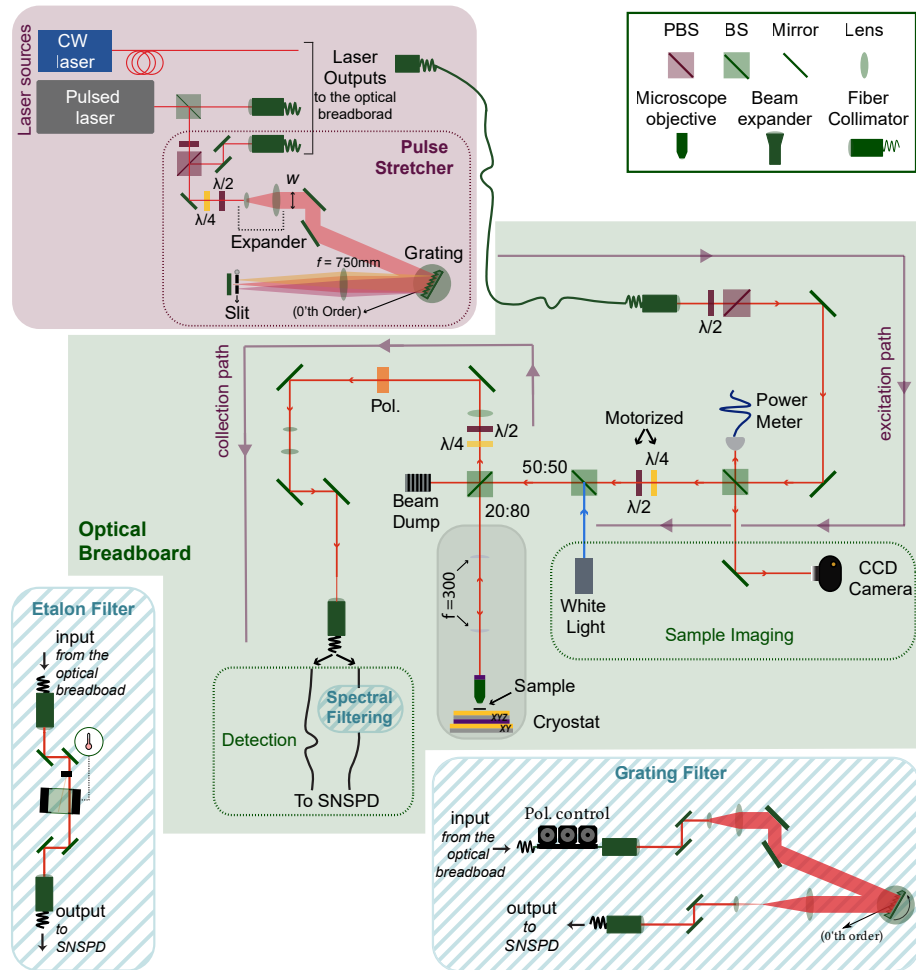


Figure 4.6: Schematic image of the optical setup. Upper-left, framed area showing the pulse stretcher in combination with the components mounted on the excitation path, until the sample stage in the cryostat are formed for directing the laser onto sample to excite embedded QDs in the nanophotonic device. The optical components presented on the sample XYZ stage and are shown following the collection path in combination with the etalon filter and / or grating filter is used for detecting the single-photon emission. The closed-cycle cryostat operates at 1.6 K.

The electrical contacts on the sample are wire-bonded to a single layer printed circuit board and connected to a low-noise voltage source. A high-resolution DC voltage source (Keithley 2450) is used to apply the gate voltage across the QDs on the sample. The voltage source operating with a low RMS noise $V_{\text{rms}} < 50 \mu\text{V}$ allows obtaining a stable charge environment. In order to further reduce V_{rms} , the output of the DC source is sent through an ultra-low noise low-pass filter (Keysight N1294A-021) before connecting to the sample. The voltage source is also used to measure current-voltage $I-V$ characteristics confirming proper electrical performance of the electrically contacted sample.

Two laser sources are employed: one of them a CW diode laser (Toptica DLC CTL 950) and the other a mode-locked Ti-Sapph laser (Coherent MIRA). The CW diode laser is tunable (50 nm wavelength band centered at 940 nm) and has a narrow bandwidth ($< 1\text{MHz}$). We lock the CW laser frequency by employing a wavemeter (with 50 MHz resolution). Due to its narrow bandwidth and continuous wavelength scan possibility, we employed the CW laser for spectral scanning of QD resonance fluorescence and for extracting the linewidth of the quantum dot transitions in resonance transmission. The optical transition linewidth of the QD is measured as $1.97 \pm 0.18\text{GHz}$. Besides, by using this laser the device performance characterization is performed by evaluating laser suppression (T_p).

Deterministic generation of the single-photon emission from the QDs can be realized by the resonant excitation of short laser pulses. Upon purely resonant excitation of the QD by a pulsed laser with an ideal pulse shape and π -pulse area, an electron-hole pair (forming an exciton) is deterministically created, which then decays to the ground state and emits ideally a single-photon. Therefore, ideally a single-photon is generated for each laser pulse with a rate that is given by the repetition of the laser pulse. In this way, we trigger single-photon emission by the mode-locked Ti-Sapph laser that creates ($\sim 3\text{ps}$ long) laser pulses, with a repetition rate of 76 MHz.

As mentioned in Section 4.2.2, the pulse bandwidth (FWHM= $\sim 100\text{GHz}$) is much broader than the typical QD transition linewidth (FWHM= $> 2\text{GHz}$), therefore, only a very small portion of the laser pulse is resonant with the QDs. That is why, we utilize a pulse stretcher to reduce the frequency bandwidth which in turn stretches the laser pulse in time. However, the temporal length of the pulse influences the single-photon purity. The purity of the QD transition degrades for very long pulse durations (Ollivier et al., 2021). Although, in principal, we would like to excite with an ultra-short and ultra-narrow pulse, by employing a pulse stretcher we can find a compromise between spectral and temporal lengths of the pulse. Here, we use a single diffraction grating based pulse stretcher setup, which is shown in the Figure 4.6 (upper-left frame). The pulse laser is split on a 50 : 50 beam splitter (BS), where the ratio $R : T$ denotes the ratio of reflected and transmitted power. While the transmitted light is directly connected to the optical breadboard, the reflected arm goes to the pulse stretcher setup. A half-wave plate ($\lambda/2$) and a polarizing beam splitter (PBS) is used for separating input from output of the stretcher. The beam is expanded before it is diffracted on a grating (groove density of 1200 lines/mm). Further, the beam is focused on a slit with a mechanically tunable width, which allows us to vary the bandwidth of the pulse stretcher. To compensate

dispersion, the beam is reflected back through the whole setup, by a mirror behind the slit. By optimizing the polarization with the $\lambda/4$ and $\lambda/2$ waveplates, the reflected beam can be separated from the input on the reflection port of the PBS, where it is then coupled by the single-mode fiber going to the optical breadboard.

The laser light is connected to the optical breadboard (highlighted with the green shaded area on the Figure 4.6) by a polarization maintaining single-mode fiber and propagates in the setup following the excitation path. After the laser polarization is controlled by the $\lambda/2$ and PBS, the input power is monitored using a photodiode power sensor for reference. The measured power is fed back to a power control unit, which allows the laser power stabilization and computer control. Meanwhile, a white light source and a CCD (charge-coupled device) camera are placed on the excitation path to illuminate and image the sample. We use this setup to monitor the device and for alignment process. The excitation laser propagates through a set of motorized waveplates ($\lambda/4$ and $\lambda/2$) for precisely adjusting the excitation polarization. The prepared excitation is reflected into the cryostat through its optical access by a BS (20 : 80). The $4f$ is imaging the collimated laser beam from somewhere ($1f$ from the lens with 300 mm focal length) on the breadboard to the back focal plane of the objective (with an NA= 0.81). Then the objective focuses the beam to the sample.

The emitted single photons are transmitted through the 20 : 80 BS to the collection path of the breadboard. Despite the spatial separation between the input path and collection path, some fraction of the reflected input beam can couple to the collection fiber. To avoid this, we have polarization control of the collection path as well (a $\lambda/4$, a $\lambda/2$ and a linear polarizer), which can be aligned to only collect the polarization of the collection grating (which is orthogonally polarized to the input grating). Subsequently, the light coupled to the single-mode fiber can be directly sent to a superconducting nano-wire single-photon detector (SNSPD). For spectral filtering, the collected light is sent to etalon and/or grating filters before being sent to the SNSPD. The choice of different detection configurations with and without spectral filters will be explained in the next sections.

A sketch of the etalon filter is shown on Figure 4.6, lower-left panel (highlighted with blue lines). The etalon has a resolution (FWHM) of ~ 3 GHz and ~ 100 GHz free spectral range. The etalon filter is formed by a Fabry P erot cavity using coated end faces of the silica block, where the cavity resonance is regulated by temperature tuning. For the separation of the reflected signal, we place the etalon with an angle, where the reflected light is then blocked. The transmission efficiency is defined by the end facets reflectivity and losses in the silica, which is evaluated as 92 %. However, the measured efficiency of the etalon filter is lower and recorded as 87 %, due to the losses at the fiber coupler.

The grating filter has a band width of 22 GHz and it is illustrated at the lower-right area of the Figure 4.6. The grating filter operates similarly to the pulse stretcher, but without the backreflection, for optimized efficiency. After controlling the polarization of the collected light via the fiber polarization paddles, we can couple the collimated light into a fiber. In this case, the NA of the fiber coupler ($\text{NA}_{\text{fiber}} = 0.13$) is employed to filter out a range of wavelength components (instead of the slit in the stretcher). The

efficiency of the grating, components on the optical setup and fiber coupling determines the grating filter efficiency as $\approx 65\%$. However, the measured efficiency is 58% , where the deviation is due to the coupling losses of the fiber.

4.4 RESONANCE FLUORESCENCE

There are different methods to optically excite a QD by employing different excitation processes for creating an exciton in a QD. In chapter 1 we described the states of the QD, the excitation and single-photon emission schemes. In this chapter, the center of our study is the realization of resonant excitation of QDs with fluorescence detection. The resonant optical excitation is specially desirable for QD investigation. With resonant pi-pulse excitation, it is possible to reach full population inversion, maximizing the probability of emitting single-photon (Tomm et al., 2021; H. Wang, He, Chung, Hu, Yu, Chen, Ding, Chen, Qin, Yang, et al., 2019a). On the other hand, the resonant excitation in opposite to the above band or quasideviant excitation does not involve random phonon relaxation process which is detrimental for the indistinguishability (Kiršanskė et al., 2017; Somaschi et al., 2016).

The resonance fluorescence technique involves tuning the excitation laser frequency to the QD resonance. In order to do that, we need to extinguish the laser excitation and detect single-photon emission. Here, since the laser background and the quantum dot emission are at the same frequency, suppressing the residual laser light is vital to perform RF measurements. Precisely for this purpose we tailored the waveguide-assisted resonant excitation device, which is introduced in Section 4.1 as an enabling method. The concept of the resonance fluorescence from a QD through the Rabi model can be found in the Appendix C. Now, we are going to experimentally investigate the waveguide assisted in-plane resonance fluorescence on the device we explained in Section 4.1 by using the above described setup in Section 4.3.

4.4.1 Resonant Spectroscopy

Continuous Wave

We perform the resonance spectroscopy by initially investigating the laser excitation suppression, previously discussed in Section 4.2.1 (see Fig. 4.4). After studying excitation laser transmittance through an array of structures for waveguide-based QD excitation on the same sample (on 20 different devices), we confirmed that each device shows the laser suppression (T_p) value less than 10^{-4} for a spectral range of ≈ 5 nm. For this characterization, we used the tunable CW laser (with narrow FWHM < 1 MHz) as an excitation source. It is important to note that meanwhile, we have not employed any spectral filtering.

We made broad range wavelength-voltage scanning on seven different devices for mapping QDs that are coupled to the waveguide. Using the tunable narrow band laser, we performed a broad spectral scan, where the applied gate voltage is swept simultaneously. Typically, the wavelength scans are chosen for spectral bands around

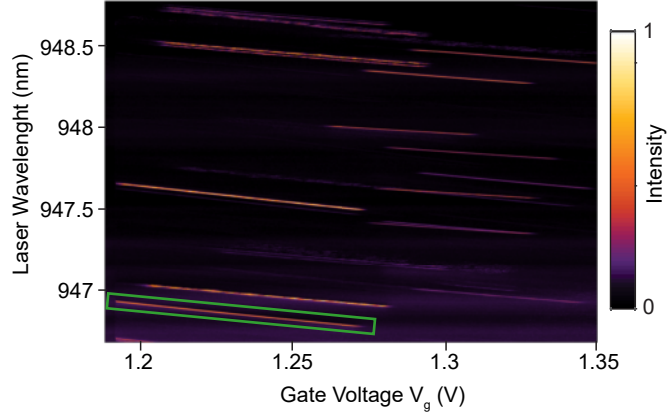


Figure 4.7: Resonance fluorescence scan through the waveguide-based QD excitation device with the laser suppression performance presented in Fig. 4.4. (a) The broad wavelength-voltage scan (center λ at 947.2 nm, V_g from 1.19 V to 1.35 V) spots several excitonic states from different QDs. The collected distinct, bright fluorescence lines confirm the strong excitation laser extinction. Green highlighted charge plateau indicates the brightest QD.

the optimum laser suppression value (centering around $T_p < 10^{-4}$). We show the wavelength-voltage scan of a device with the optimum performance (in terms of QD transition intensity, T_p and ξ) in Figure 4.7., where distinct emission for different quantum dots are visible. Here, transmitted intensity counts are recorded directly by the SNSPD, while tuning the CW laser (center wavelength at 947.2 nm, with 1.5 pm step sizes). For each excitation wavelength the gate voltage (V_g) is swept from 1.19 V to 1.35 V with 0.2 mV. The scan is performed at $1 \mu\text{W}$ laser power to be in the weak excitation limit (at $\approx 1\%$ of the saturation power) to avoid power broadening. Consequently, each individual bright line (plotted with high intensity values) indicate the resonance fluorescence from QDs. Based on our previous photoluminescence characterizations on several QDs from this sample, we can identify the QD resonances from neutral excitons between 1.2 V and 1.28 V and the negatively charged excitons at higher voltages. Typically on this wafer, the difference between the binding energy of the neutral and singly-charged exciton was measured ≈ 4 nm. Accordingly, in this voltage-wavelength scan for 2 nm spectral band, plotted neutral and charged excitons are from different QDs. From this resonance fluorescence map, we show 15 QDs that are coupled to the waveguide with a strong coupling efficiency (β_C) and reduced single-photon impurity ξ . Since we want to investigate the neutral excitons with linear dipoles, 5 QDs can be candidate as a single-photon source.

From the wide spectral mapping for ≈ 2 nm, the brightest QD transition is identified with the most distinct Coulomb charge plateau (green box in Fig. 4.7.). Figure 4.8.a. shows high resolution scan of the QD transition, studied in this chapter. By Stark tuning, the resonance fluorescence wavelength of the dot can be tuned over 0.2 nm (48 GHz), which is extracted from the charge plateau of the neutral exciton. From the

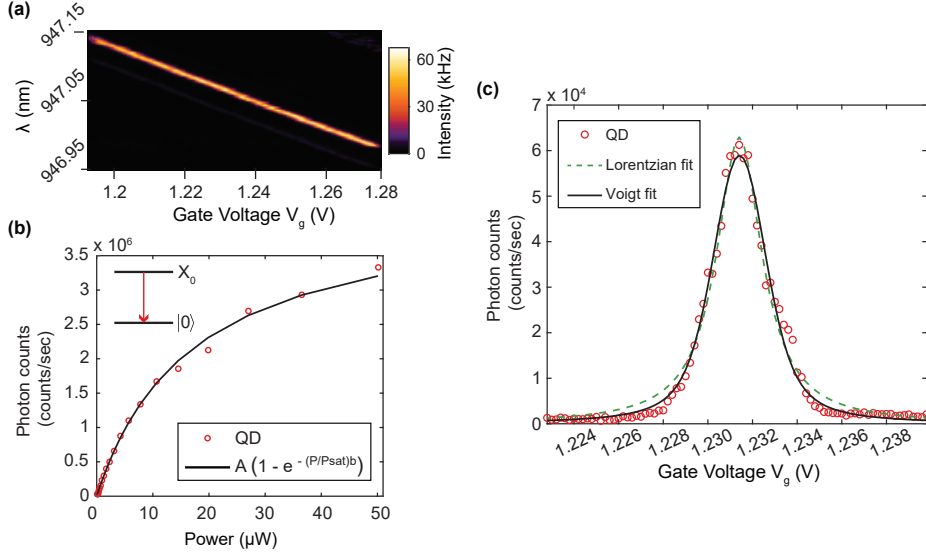


Figure 4.8: Spectral characterization of the brightest QD under CW laser excitation. (a) The resonance fluorescence of the QD neutral exciton is the zoomed view showing the distinct Coulomb charge plateau of the QD with the highest brightness, which is marked with green in the broad wavelength-voltage scan in Fig. 4.7. The dot tunes 0.2 nm from edge-to-edge of the charge plateau under CW excitation at $P = 0.01 \cdot P_{sat}$. (b) Saturation curve of the neutral quantum dot emission at $\lambda=947.05$ nm and 1.231 V. (c) The line shape of the resonance fluorescence as a function of gate voltage. The green dashed and black lines are Lorentzian and Voigt fits, respectively.

slope of this tuning curve, the Stark parameter for this QD is extracted as 0.68 GHz/mV. Throughout the entire tuning range, the quantum dot peak is clearly visible above the background owing to strongly suppressed laser background and low electrical noise provided by the high quality pin diode.

By increasing the power of the CW laser, the QD exciton emission shows saturation, as seen in Figure 4.8.b. The expected behavior of power dependent resonance fluorescence is described by a steady state saturation model (Meystre & Sargent, 2007). The power dependent QD emission intensity exhibits $I_{max}(1 - e^{P/P_{sat}})$, where P is the excitation laser power, and P_{sat} is its saturation power of the QD, and I_{max} is the saturated maximum counts. The curve can be used to identify the neutral QD exciton emission.

Figure 4.8.c. plots the emitted photon counts around the central wavelength of the charge plateau ($\lambda \approx 947.07$ nm) with red circles in the low power limit ($P \approx 0.01 \cdot P_{sat}$). From this, we can extract the linewidth of the QD neutral exciton. The steady state model predicts a Lorentzian lineshape with $FWHM = \Gamma + 2\Gamma_{dp}$ for the emission line (see Appendix C.), where Γ and Γ_{dp} stand for radiative decay rate and dephasing rate respectively. However, as we can see in Figure 4.8.c., a Lorentzian fit (shown with dashed lines) with the emission peak shows deviations. This deviation can be explained

by the spectral diffusion (Kuhlmann et al., 2013; Matthiesen et al., 2014; Stanley et al., 2014).

Charge noise in the solid state environment affecting the local electric field around the QD induces Gaussian broadening of the emission (Kuhlmann et al., 2013). Here, we measure the convolution of the Lorentzian and the Gaussian noise resulting in a Voigt lineshape. In Figure. 4.8.c., we can see the FWHM of both Lorentzian ($FWHM_L$) and Voigt models ($FWHM_V$);

$$FWHM_L = (2.47 \pm 0.06) \text{ mV} = (1.68 \pm 0.06) \text{ GHz} \quad (4.8)$$

$$FWHM_V = (2.90 \pm 0.18) \text{ mV} = (1.97 \pm 0.18) \text{ GHz}. \quad (4.9)$$

We see that a Voigt profile with the black solid curve can model the lineshape of the peak more accurately. Since the spectral characteristics of the QDs on this wafer were previously determined, these fitted linewidths seems not be immediately relevant to the expected value $FWHM = \Gamma + 2\Gamma_{dp}$. To identify the transform limited lifetime, we can perform the time-resolved resonant measurements with pulsed resonant excitation, which is the topic of next section.

Pulsed Resonant Excitation of a QD

To enable pulsed resonant excitation, we employ the mode-locked Ti-Sapph laser and the center frequency is tuned to QD resonance (315.485 THz). The etalon filter and the pulse stretcher (where the bandwidth is cut down to ~ 50 pm) are used for excitation. By using the SNSPD, we detected a transform limited Gaussian pulse with ~ 26 ps duration. A power scan is plotted in Figure 4.9 to show the pulsed resonance fluorescence intensity. By increasing the pulsed resonant laser excitation, we can see the Rabi oscillations. Towards reaching the π -pulse excitation, we see that the QD transition saturates. We fit the data with the Rabi model from the master equation (see Appendix C), where we also included the dephasing. Furthermore, we probe the emitted single-photon impurity ξ simultaneously as a function of excitation power. To do that, we recorded the emitted single-photon emission intensity when the QD is electrically tuned to be in and out of resonance. The single-photon impurity ξ is experimentally evaluated as

$$\xi = \frac{I_{\text{QD,off}}}{I_{\text{QD,on}} - I_{\text{QD,off}}}, \quad (4.10)$$

where $I_{\text{QD,on}}$ and $I_{\text{QD,off}}$ are the single-photon emission from the QD when the gate voltage is tuned in and out of resonance, respectively. Here, the excitation power dependence of the ξ highlights the importance of the laser suppression characteristic of the device (see Fig. 4.9). Since, we can see that with the increased laser pump power, laser background is intensified.

In the low power limit, we measure the single-photon impurity $\xi(P \rightarrow 0) = 1.7 \cdot 10^{-3}$. In Section 4.2.2, we defined single-photon impurity as $\xi \approx 2T_p / \beta_E \beta_C$ and laser suppression as $T_p = 2 \cdot 10^{-5}$. Consequently, we can evaluate the coupling efficiency of the single

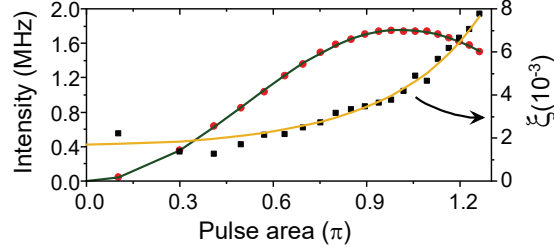


Figure 4.9: Intensity of resonance fluorescence and the single-photon impurity ξ as a function of pulsed excitation power. The measured intensity data (blue dots) is fitted to the Rabi model (red curve), where the pure dephasing rate ($\gamma_d = 0.2/n$ sec) is taken into account. The single-photon impurity is characterized by using the equation 4.2 with employing the measured raw counts and the background.

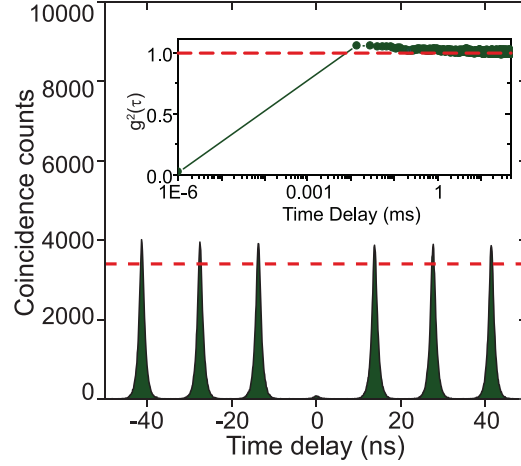


Figure 4.10: The auto-correlation histogram from the Hanbury Brown and Twiss experiment under π -pulse laser excitation using the stretched pulses (bin size or time span is ~ 100 ps) and the etalon is utilized for spectral filtering. $g^{(2)}(0) = 0.02 \pm 0.005$ is extracted from the by comparing the fitted amplitude of the central peak to the fitted amplitude for peaks at a time delay of $\sim 50 \mu\text{s}$, shown by the red dashed plot. At the inset shows again the second-order intensity correlation, where this time $g^{(2)}(\tau)$ is extracted by integrating the coincidences under the peak over the $50 \mu\text{s}$ bin size.

photon emission into the waveguide collection mode $\beta_C = 0.8$, which determines the QD position. From Figure 4.5., we can see that the QD position is at ≈ 20 nm off-center in the dual-mode waveguide. For deterministic QD preparation (at π -pulse excitation), we measure the impurity as $\xi(P \rightarrow P_{pi}) = 0.004$ and accordingly.

4.5 DEMONSTRATION OF HIGH PURITY SINGLE PHOTONS

The impurity, or the leakage of the resonant laser used to excite the QD, eventually limits the single photon purity of QD emission. The most common method to characterize the single photon purity is based on Hanbury Brown Twiss (HBT) experiment (Brown & Twiss, 1956) schematically depicted in the previous Chapter (Reference will be added). Also the general principle of evaluating second order correlation function $g^{(2)}(\tau)$ was expressed, utilizing intensity correlation measurement between two detectors at the outputs of the 50 : 50 beam splitter. The result of this correlation function as a function of the delay between two detectors measured for the QD under study is shown on Figure 4.10. The measurement is performed using pulsed excitation laser explained previously using optical π -pulse excitation (Figure 4.9). The intensity of the central bin gives the value of the $g^{(2)}(\tau = 0) = 0.020 \pm 0.005$, indicating high purity single photon emission.

The contribution to the $g^{(2)}(0)$ from the impurity can be estimated by Eq. 4.7 and bounds the $g^{(2)}(\tau = 0)$ to 0.008. The characterization of the current structure gives the indication that this contribution can be as small as 10^{-4} , which is close to the best reported value in the community (Schweickert et al., 2018), where in contrast to our experiment a nonresonant excitation scheme was used.

The second contribution reducing the single photon purity can be attributed to the re-excitation errors. In our experiment, the excitation pulse of ~ 26 ps was used which is only 25 time shorter than the QD decay time (~ 640 ps). This leads to nonzero probability of re-exciting the QD during the excitation pulse leading to two-photon emission (Fischer et al., 2017). The trade off between these contributions requires optimization of the experiment to improve the single photon purity even further. By improving the design and imperfections of the fabricated device, we can decrease the T_p value for a broad wavelength range to achieve even higher performance.

4.6 PHOTON INDISTINGUISHABILITY

The ability to produce indistinguishable single photons is crucial for most of the quantum information applications. Figure 4.11.(a) shows a scheme of the Hong-Ou-Mandel (HOM) experiment (Hong et al., 1987) to evaluate the two photon interference visibility and measure the indistinguishability. The setup is based on the unbalanced Mach-Zender interferometer with a path difference matching the period of the excitation laser, such that two photons emitted in the neighboring pulses will interfere with each other on the output fiber-based 50:50 beam splitter. The resulting two-photon intensity correlations between two detectors are shown on the Figure 4.11.(b).

To evaluate the quality of the interference the motorized $\lambda/2$ waveplate is used. It allows one to perform two experiments corresponding to the case of distinguishable and indistinguishable photons with parallel and perpendicular polarizations, respectively. This results in raw visibility of $V_{\text{raw}} = (91 \pm 2)\%$, directly indicating well suppressed dephasing processes during the emission. We estimate the contribution to this visibility V from the photon statistics using measured $g^{(2)}(0)$, and from the interferometer

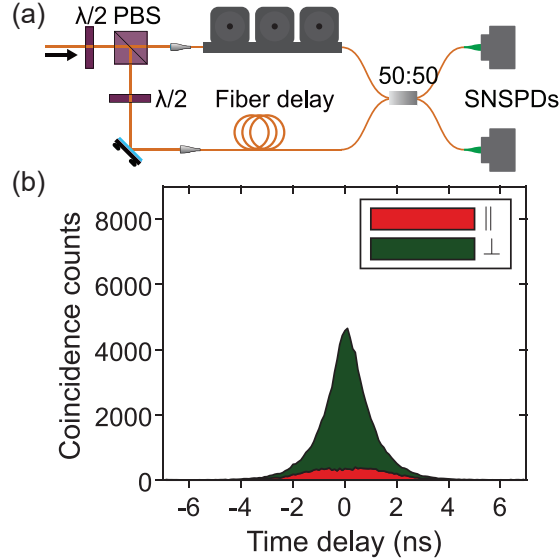


Figure 4.11: Photon indistinguishability measurements. (a) Illustration of the Hong-Ou-Mandel experiment, where the two subsequent photons interfere in a Mach-Zender interferometer for measuring indistinguishability. Lower arm shows the delay given by the laser pulse separation of 13.7 ns. (e) Indistinguishability by the HOM visibility. Detected coincidence counts are plotted to illustrate the contrast between the copolarized (red) and cross-polarized (green) input photons.

imperfections, and end up with the value of $V = (96 \pm 2)\%$. This value is comparable with the state-of-the-art experiments based on QDs (He et al., 2019; H. Wang et al., 2016; Wei et al., 2014).

* * *

In this chapter, we introduced a novel device based on dual-mode waveguides to achieve in-plane pulsed resonant excitation of QDs. The working principle of the device was explained, and we presented main performance figures-of-merit, such as the laser suppression and single-photon impurity. Resonant excitation was then performed on several QDs, and outstanding performances were demonstrated, in terms of purity of the single photons collected and their indistinguishability. With figures-of-merits on par with previous experiments, waveguide-assisted resonant excitation represents a promising way to produce single photons with high purity, efficiency, and indistinguishability, which are the resources necessary for realizing on-chip scalable quantum experiments. One additional requirement to quantum devices is the reproducibility of the performances between devices with the exact same nominal parameters, in the same fabrication run and from different chips. Higher yield is then achievable, but more importantly, a quantum circuit containing devices in parallel can then be developed. The performance parameters of the device presented in this chapter rely strongly on

the filtering of the first order mode of the pump laser, which is linked to photonic crystal filter performance. It is therefore critical to characterize the reproducibility of the photonic crystal, which are known to be sensitive to fabrication imperfections, and to propose a filtering method with a robust geometry. Finally, to give the best performance for any QD wavelength, the device should be optimized to demonstrate a high laser suppression for a broad wavelength range.

IMPROVED DESIGN OF WAVEGUIDE INTEGRATED SINGLE-PHOTON SOURCES

Plug-and-play single-photon source with a scaled-up architecture requires a wideband operation, where multiple QDs can emit coherent single photons with high purity and indistinguishability simultaneously. To acquire high purity single photons, resonance fluorescence should be collected by strongly suppressing the background laser signal. To resonantly pump multiple QDs by the in-plane method, simultaneously, we need to build a nanophotonic circuit where detection channels of single photons can have a robust laser suppression performance. The waveguide-assisted resonant excitation (in-plane RF) device which has been explained in the previous sections of this chapter can drive the excitation laser on a QD by suppressing the laser with T_p of $\sim 10^{-5} < 2nm$ spectral window, while the QD single-photon coupling efficiency is $> 80\%$ (see Fig4.5). The investigated in-plane RF device achieves the coherent single-photon emission from a QD with high purity ($g^{(2)}(\tau = 0) = 0.020 \pm 0.005$) and indistinguishability ($V = (96 \pm 2)\%$). However, the inherent boundaries of this device, such as its narrow bandwidth, limited room for improving the single-photon purity based on fabrication-induced imperfections, and challenging reproducibility, lead us to investigate an alternative design. In this section, the current limitations will be explained, and a different device design will be introduced, which can overcome the challenges.

5.1 LIMITATIONS ON THE LASER EXTINCTION

The fraction of the excitation signal to the noise defines the laser extinction at the emitter section (ζ). Our target is to generate highly pure odd mode for QD excitation and avoid any noise at the emitter region. We can evaluate the laser extinction in terms of transmission efficiencies of the excitation mode (mode E with odd symmetry, T_{odd})

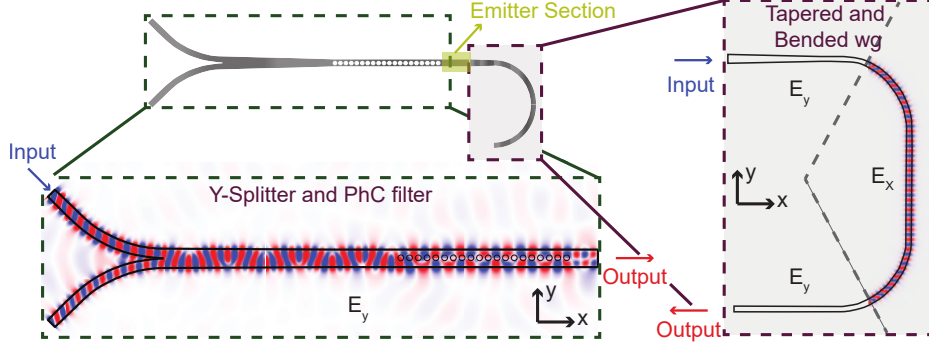


Figure 5.1: Schematic of the entire 3D in-plane resonance fluorescence device model (based on the Y-splitter, PhC filter, tapered, and two-fold bended waveguide) showing the propagating electric field component in the direction of QD dipole. In-plane RF device geometry is modeled with the photonic crystal waveguide section with 20-hole with 72 nm radius, 220 nm lattice constant, and 450 nm width on a 170 nm thick GaAs at 1.6 K. Y-splitter branches are split by 90° angle, and the symmetric branches are single-mode waveguides with 257 nm width. Before the PhC filter section 514 nm wide waveguide is tapered down to form the dual-mode waveguide (nm width) over 5 μm . After the emitter section (1 μm long), the waveguide is tapered to 200 nm over 5 μm and two 90° waveguide bend is introduced.

and the collection mode (mode C with even symmetry, T_{even});

$$\zeta = \frac{T_{\text{odd}}}{T_{\text{even}}}. \quad (5.1)$$

Figure 5.1 shows the electric field propagated through the in-plane RF device, confirming that the mainly odd mode is excited in the emitter section. However, to address the influence of laser extinction, which impacts laser suppression (and by turns, single-photon purity), we analyzed the transverse electric field in the device.

We calculate the transmitted fraction of the excitation and collection modes for the in-plane RF device (based on the Y-splitter, PhC mode filter with unperturbed geometry, tapered and two-fold bended waveguide) for the full 3D structure (where Section 4.1.1 evaluates sub-components of the device individually). Besides, we evaluate the mode transmittance for the reference structure in the absence of a PhC filter section (which is designed for generating the mode for resonant excitation). Transferred power fractions are shown in Figure 5.2, bottom plot and on top, the consequent laser suppression performance is calculated.

The simulation results show that the laser extinction value is limited to -20 dB, though calculated to be ~ -14 dB in the wavelength region of interest (935 \pm 5 nm). (Fig. 5.3)

5.1.1 Discussion on the device imperfections

Based on structural characterization of the single-photon devices (Pregolato, 2019), we know that some circuit components may not be robust to the fabrication-induced

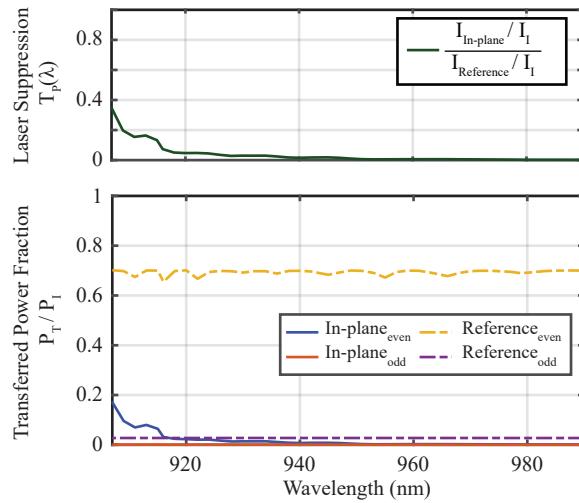


Figure 5.2: Calculated laser suppression based on the 3D FEM models of complete device considering unity in and out-coupling efficiency to the nanophotonic circuit(top), evaluated by the power transmission efficiencies of the even and odd modes (bottom). The geometrical parameters of the in-plane RF are identical to Fig. 5.1, in which the reference structure is designed without the PhC filter.

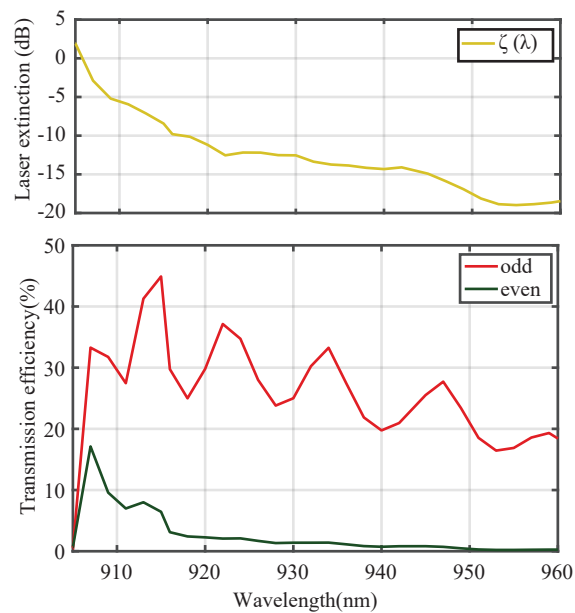


Figure 5.3: Laser extinction and transmission efficiencies as a function of wavelength. Data is calculated at the emitter section for the model, combining the Y-splitter and PhC filter components (structural parameters are same as in Fig. 5.1)

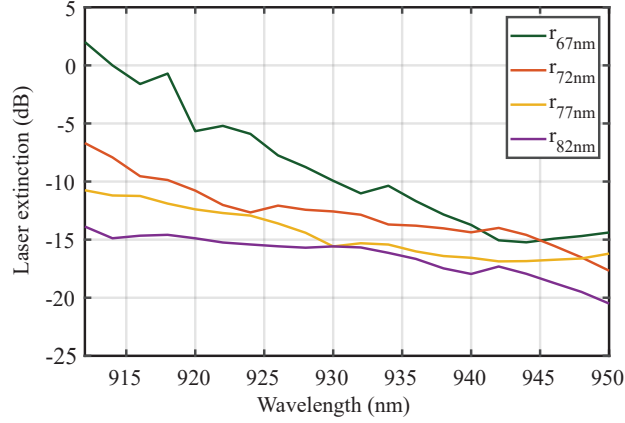


Figure 5.4: Effect of the fabrication imperfection on the essential figure-of-merit: laser suppression. Laser extinction are calculated for two different models (at their emitter sections), where the PhC is designed with varying hole radius (the rest of the geometrical parameters are identical).

imperfections. For example, fabricating PhC of holes without any feature size variation compared to the designed values is highly challenging. Usually, we expect an enlargement in hole size radius by $\approx 5 - 10$ nm (Pregolato, 2019). In turn, this increases the low refractive index region volume and blue-shifts the PhC bands resulting in a shifted transmission spectrum of the filter. As a result, waveguide mode frequencies at the band edge can be pushed out from the PhC filter bandgap by the growth in the hole radius. Consequently, by shifting the mode frequencies, the transmission is shifted, as shown in Figure 5.4. Besides, with the difficulty of reproducibility, it is challenging to control the laser extinction and, accordingly, the suppression and impurity.

5.1.2 Asymmetric Directional Coupler for In-plane RF

Figure 5.5 shows the optical circuitry based on the coupled-line asymmetric-directional coupler, which is the proposed design with a significantly improved laser suppression performance and wide spectral-bandwidth. The proposed nanophotonic circuit integrates rectangular and bended waveguides, which are more robust features to fabrication imperfections with higher yield and reproducibility.

As it is depicted in the Figure 5.5., we feed the excitation laser through a single-mode waveguide ($w_{SM} = 208$ nm). The propagating mode with the even symmetry (TE_{00}) is guided through the waveguide bend and coupled evanescently to the dual-mode waveguide. The excitation mode is designed to be prepared in the odd mode (TE_{01}) dominantly at the emitter section of dual-mode waveguide ($w_{DM} = 404$ nm). Coupling occurs by leaking the evanescent field of the excitation laser mode energy (or power) slowly from the single-mode waveguide to the adjacent dual-mode waveguide, which is then exchanged between the two waveguides along the coupling length. The inset in

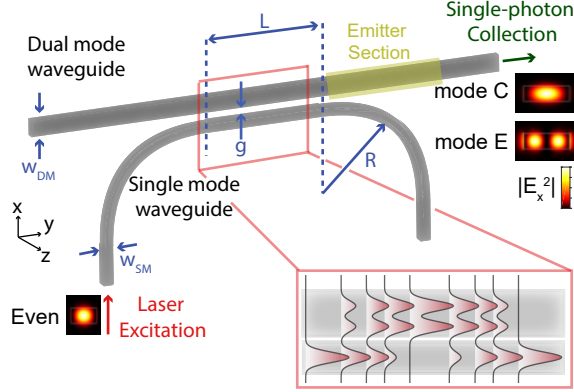


Figure 5.5: Coupled line asymmetric-directional coupler device enabling in-plane, resonant excitation of a quantum dot directly through a waveguide. The excitation pulse is pumped through one of the u-bend branches and coupled into the fundamental even mode of the single-mode GaAs waveguide, as it is depicted in the figure. Subsequently, the propagating even mode is evanescently coupled to the dual mode waveguide. At the emitter section predominantly the odd mode (mode E) is generated for triggering the QDs, which are off-centered in the waveguide. The evanescent transmission efficiency into the dual mode waveguide is optimized by tuning the geometrical parameters (w_{SM} : single-mode waveguide, w_{DM} : dual-mode waveguide, g : gap between dual-mode and single-mode waveguides, L : coupling length, R : symmetric u-bend waveguide radius).

the red frame sketches the power transfer between two waveguides, ideally a periodic oscillation of their supermodes (even and odd).

In the illustration, we show the device component responsible for preparing the in-plane excitation laser for the QD. Our design can easily adapt fiber coupling via spot-size converters (Uğurlu et al., 2019), which can theoretically reach the unity coupling efficiency required for scalability. To ensure uni-directional propagation of the single-photons in the dual-mode waveguide, increasing the the single-photon collection efficiency, we can plug a PhC mirror for the mode C (even mode) at the opposite side of the collection port. Besides, the symmetric branch of the U -waveguide can be used to assure alignment to the circuitry.

The transmission spectrum of the full device is calculated by employing 3D FEM simulations by considering the potential fabrication imperfections. The impact of tuning the width of single-mode and dual-mode waveguides (while we keep the other structural parameters constant) on the laser extinction is shown in Figure 5.6.a,c. Waveguides are robust to fabrication-induced effects since we can controllably apply the correction factors and we observe the width shrinking $\sim 3.5\%$ on average (Pregolato, 2019). When the designed dual-mode waveguide width, $w_{DM} \approx 404$ nm, the laser extinction can be tuned by ~ 14 dB (Fig. 5.6.a). The impact of the single-mode waveguide width is higher, as shown in Fig. 5.6.b. When the designed width is 208 nm, the fabricated waveguide width is shrunk to 203 nm and the laser extinction is tuned by ~ 20 dB. Figure 5.6.b and d. show the effective refractive index of the modes as a function of

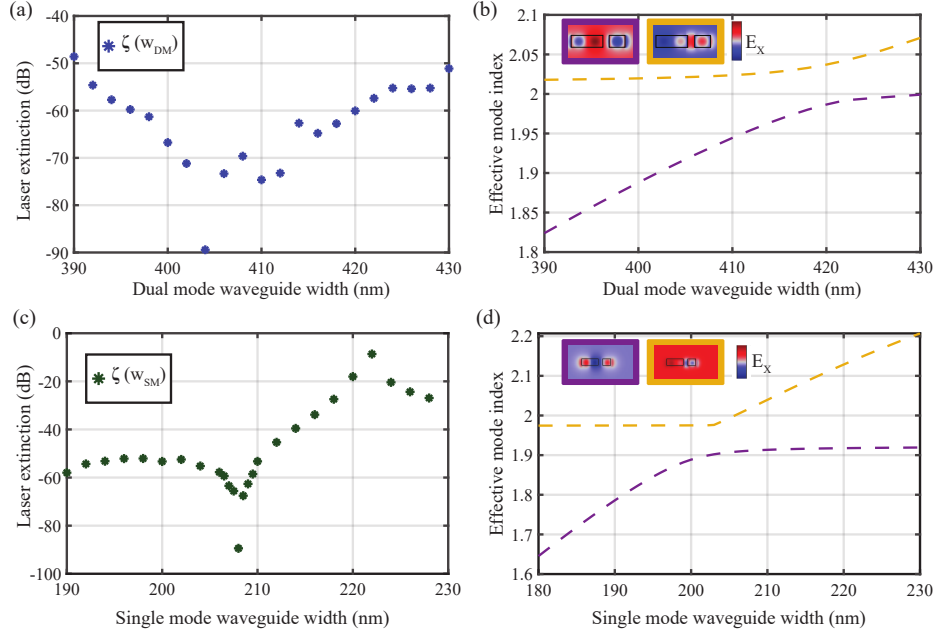


Figure 5.6: Tailoring the dual-mode and single-mode waveguide widths of the asymmetric directional couplers for optimizing the laser extinction performance and evanescent coupling, studied by the effective index contrast.

dual-mode and single-mode waveguide width, respectively. We can see the reduced index contrast where the evanescent mode coupling is stronger. Due to the FEM solver configurations, we see a small shift between 3D and 2D simulations.

The previously presented in-plane RF device based on the Y coupler, PhC filter, tapered and bended filters shows -14 dB for ~ 5 nm wavelength window. However current model based on asymmetric directional coupler shows a laser extinction of maximum -47 dB within 60 nm spectral window, as presented in Fig. 5.8, which is a significant improvement of the device bandwidth.

Calculations for investigating the impact of the geometrical parameters show that the extinguished even mode is robust within a large spectral window. We can see that the efficient generation of the excitation mode (odd mode) at the emitter section in the dual-mode waveguide can be achieved with high reproducibility (based on its robustness to fab.-induced effects). The proposed design is ready to improve the in-plane resonant excitation of a quantum excitation through the waveguide in terms of better purity, power performance, and wide bandwidth.

Here, our ultimate goal is to boost the laser extinction (ζ) at the emitter section. Therefore, we investigate the mode transfer and coupling behavior of the asymmetric directional coupler. We study the propagating fundamental modes in the evanescently coupled waveguides by utilizing FEM simulations. Initially, we calculated the influence

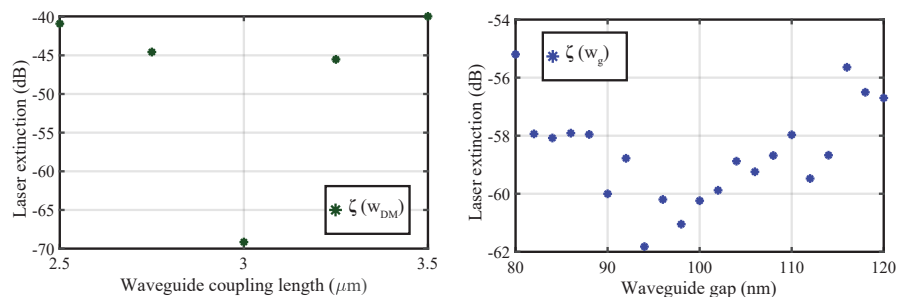


Figure 5.7: Tuning the waveguide coupling length (L) and gap (g) for monitoring the laser extinction performance via tuning the evanescent coupling.

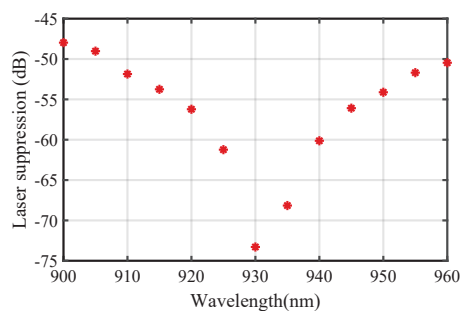


Figure 5.8: Laser extinction bandwidth of the asymmetric directional coupler-based In-plane RF device.

of the single-mode and dual-mode waveguide widths on the laser extinction parameter (see Fig. 5.6). The evanescent coupling strength can be further boosted by optimizing the gap distance between the waveguides. Besides, by tailoring the gap and length of the coupling region, we can improve the coupled fraction of light between the adjacent waveguides.

5.1.3 Power Budget for Resonance Fluorescence

When we excite the QD out-of-plane, we need an optimized setup design including free-space optics and electro-optical elements to prepare the resonant excitation pulse. While driving the resonant excitation laser on the QD with the in-plane method, we couple to the nanophotonic circuit after passing through a similar excitation setup. Also, we introduce on-chip losses. Considering the scalability in terms of multiple QD resonant excitation, the implementation becomes challenging as the power budget becomes an important criterion.

Initially, we evaluate the electric field prepared at the emitter section under $1\mu\text{W}$ input power by the finite-element electric-field approach. Figure 5.9a. and b. shows the

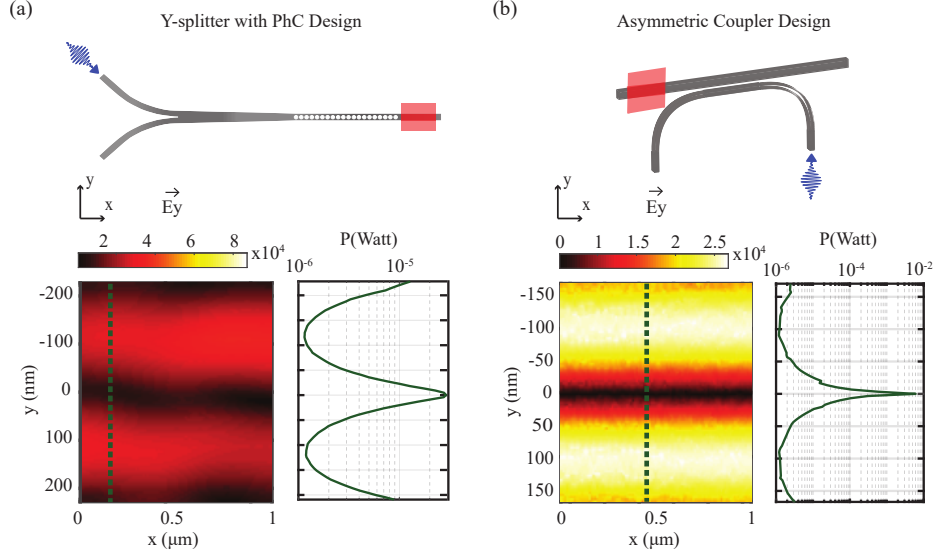


Figure 5.9: Electric field produced at the emitter sections of in-plane RF devices and required peak pulse power at the excitation port for reaching the π -pulse area for QD resonant excitation. (a) Waveguide-based excitation, where the QD excitation pulse is generated through a Y-splitter and PhC. (b) The in-plane RF device is based on the asymmetric directional coupler design. The electric field is evaluated by FEM calculations. Excitation laser peak power is calculated along the cross-section (a single cut line is selected, shown with green dashed lines) of the emitter sections.

two different in-plane RF designs, which were both explained earlier in this chapter. Here, we see dominantly generated odd mode for exciting the QD. By utilizing the electric field in the dipole direction, we can calculate the required laser peak power for resonant excitation of the QD and by using the Rabi frequency (Ω) at zero detuning.

First, we calculate the electric field driving the emitter section by using the Rabi frequency (Ω_π) at the π -pulse area. Experimentally, the excitation pulse has the Gaussian form. Since here, we count on the peak power of the laser, we use a square sine wave ($\pi/2\sqrt{2\pi} \cdot 1/\tau_p$) to model the laser pulse. As explained previously, the pulse length is stretched to $\tau_p = 30$ ps and the funneled power is $1 \mu\text{W}$. Assuming that the dipole and electric field polarization are parallel, the strength of the electric field can be derived as

$$\vec{E} = \frac{\hbar}{\vec{d}} \Omega_\pi, \quad (5.2)$$

where \vec{d} is the transition dipole moment of the charged particle of the QD in the homogeneous media. The transition dipole \vec{d} is given by $\vec{d} = q \cdot \vec{r}_{vc}$, where q is the elementary electric charge and $vec(r)_{vc}$ is the the dipole matrix element. In GaAs, the magnitude of $abs(vec(r)_{vc})$ is approximately 6.1 Å (Rosencher & Vinter, 2002). Accordingly, we calculate the electric field strength 3.18×10^4 V/m at the emitter section

Figures-of-merit	Y-splitter with PhC Design	Asymmetric Coupler Design
ζ	-14 dB	-89.42 dB
P_E/P_{in}	25%	34%
P_π	1.6 μ W	1.6 μ W

Table 5.1: Measures for evaluating the single-photon purity and power budget for the resonance fluorescence in in-plane RF devices.

for the driven π -pulse peak power. Finally, to have a reasonable power budget, we require a peak power of at least 10 W at the π -pulse area. Note that for the waveguide-based, in-plane excitation approach, the QD position is a crucial factor, and we consider QD position based on the calculations in Fig. 4.5. We chose the 75 nm offset from the waveguide center to have a consistent comparison with the previously measured device in Sec 4.5. Figure 5.9 plots the laser pulse peak power for a single cut at the waveguide cross-section for both in-plane RF designs, where we obtain the required laser peak power as $\sim 1.6 \mu$ W at 75 nm distance from the waveguide center when a signal with 1 μ W power is injected to circuits.

For comparison, we can estimate the required peak power of the pulse for resonant excitation of the QD out-of-plane. The focused area of the beam on the QD $\sim 1 \mu\text{m}^2$ area. Now, by taking into account the calculated electric field strength $E \approx 3.18 \times 10^4$ V/m, the impedance of free space $Z=376.73 \Omega$, we can calculate the required peak power: $P = E^2 \cdot A/Z$ as 2.7 μ W.

As we see, Rabi flop is reached approximately at 10 μ W driving laser power, which is ten times higher compared to the out-of-plane triggering.

In Table 5.1 we define the power fraction of the input laser monitored at the emitter section for exciting the QD (P_E/P_{in}), which is related to the power budget.

Besides, in the in-plane RF model with PhC filter, emitters sitting on the dual-mode waveguide, hosting predominantly the odd mode and negligibly the fundamental mode at around 940 nm. Still, in the presence of the fabrication imperfections and at the different wavelength windows.

* * *

In this chapter, we introduced an improved design to realize waveguide integrated single-photon sources, robust to fabrication imperfection and presenting large laser suppression for a broad wavelength range. We started by highlighting the impact of fabrication imperfection on the laser extinction of the in-plane RF design based on mode filtering with a PhC. We concluded that unavoidable PhC holes size variation leads to a decrease of laser extinction and shift in the spectrum of the device, an obstacle to reliable reproducibility. In turn, we proposed an in-plane RF device based on an asymmetric directional coupler. This all-waveguide based geometry presents the advantage to be more robust to fabrication errors and shows excellent performance in term of laser suppression and bandwidth. We finally estimate the excitation power needed to excite the QDs deterministically and show that it fits the laser power available

in lab conditions. This optimized design enables the integration of plug-and-play single-photon sources within a scaled-up architecture, thanks to the excellent laser suppression for a spectral window as broad as the QD inhomogeneous broadening and the expected reproducibility. Additionally, spot-size converters can be integrated into this geometry to realize fiber-based excitation and collection, a necessary requirement for scalability in terms of efficiency and packaging.

CHAPTER



6

TOWARDS SCALABLE CHIP-TO-CHIP AND CHIP-TO-FIBER INTERFACES

In this chapter we present the recent efforts in scaling the chip-to-fiber coupling method (Chapter 3) to multi-port optical channels using suspended spot-size converters (SSC). As highlighted in Chapter 1, the integration of multiple input-output optical interfaces is key for scaling quantum photonic integrated circuits including single-photon sources (Kim et al., 2017; Uppu et al., 2021) and realizing hybrid platforms that rely on different chip materials. For example, the lithium niobate (LN) circuit platform offers excellent switching functionality with low loss, which is key for quantum gate operation. However, the LN platform relies on waveguides with large mode-field profiles and thus are not directly compatible with GaAs waveguides. In the following, we discuss the challenges towards realizing optical interfaces between waveguides or fibers of different sizes using spot-size converters compatible with quantum photonic integrated circuits in GaAs. The data and results presented here, while preliminary, indicate that the SSC devised in this thesis constitute a promising approach to scalable chip-to-fiber coupling and to realize fully-packaged single-photon sources.

6.1 MULTI-PORT CHIP-TO-FIBER COUPLING

The standard approach to interfacing multiple waveguides to fibers relies on fiber arrays, which consist of fibers aligned on a v-groove carrier with equal spacing (see Fig. 6.1 for conceptual illustration). Several manufacturers provide customized fiber-array solutions, including polarization-maintaining, angled-polished, and anti-reflection coated fibers⁽¹⁾. Fiber arrays are widely used to pigtail photonic chips such as diode lasers, modulators, and optical transceivers. However, one significant limitation of v-groove

(1) <https://www.sqs-fiberoptics.com/products/fiber-optic-arrays>

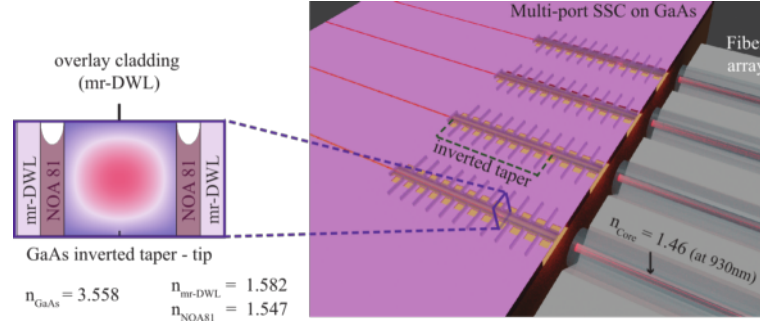


Figure 6.1: Concept and implementation of coupling between multi-port SSC and four channel fiber array. Optical fiber array assembly, where the fibers are inserted on the v-grooves with a pitch of $127\ \mu\text{m}$ and multi-port polymer out-couplers designed accordingly. Inset shows the cross section image of the SSC at the end inverted taper tip showing the mode field diameter. Optical mode is localized in overlay cladding and UV adhesive (NOA81 is deposited in the micro channels between the polymer walls (patterned with mr-DWL5) and cladding). Refractive indices are given to highlight the index contrast preventing guided mode leakage to the surrounding optical adhesive.

fiber assemblies is that lensed fibers cannot be aligned with precision and manufactured with high repeatability, resulting in sub-optimal coupling with the chip. While more advanced solutions likely exist in the market, they require complex manufacturing processes, for example three-dimensional printing.

To couple single photons off-chip to a standard fiber array, larger mode-field diameters (MFD) of SSC are required. For example, a typical 930 nm fiber core MFD is $\sim 4.75\ \mu\text{m}$, which is more than four times larger than what was previously demonstrated. Increasing the size of the overlay polymer waveguide, however, is challenging, as it leads to multi-mode guiding conditions and therefore requires longer inverted tapers to satisfy the adiabatic transfer of the GaAs waveguide mode to the fundamental mode of the overlay waveguide (see Fig. 6.1 inset). From numerical simulations (cf. Chapter 3), we estimate that an optimal taper length would be around $141\ \mu\text{m}$ -long (see Fig. 6.2). Clearly, such a long suspended taper cannot be realized directly without a risk of collapse and bending due to stiction. Therefore polymer support tethers are built with equal spacing ($15\ \mu\text{m}$) which anchor the epoxy polymer walls. Subsequently, optical adhesive is infiltrated into the channels and UV cured to ensure permanent, stable formation.

6.1.1 Device design

To fabricate longer tapers with overlay epoxy waveguides with larger MFD, we propose to infiltrate the suspended waveguides with an optically-transparent and ultraviolet (UV) curable adhesive through microfluidic channels (see the device structure in Figure 6.2). By doing so, the polymer waveguide is supported mechanically, while keeping the optical mode localized in the overlay cladding. The adhesive is chosen so that

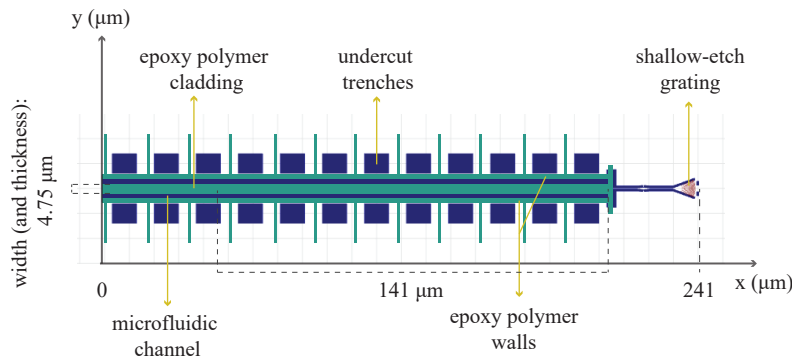


Figure 6.2: Spot Size Converter for fiber array coupling. Hidden beneath the epoxy polymer layer (represented by teal color) is the $141\ \mu\text{m}$ -long taper necessary for adiabatic mode transfer into the fundamental mode of the overlay cladding. Microfluidic channels are formed between the epoxy polymer cladding and walls that are infiltrated with UV-curable adhesive which is able to reinforce the epoxy-taper structure. The 'undercut trenches' are spaced appropriate to allow for complete undercut during the wet etch release step. Shallow-etch grating is used to collect or emit the signal for characterizing the coupling performance of the SSC.

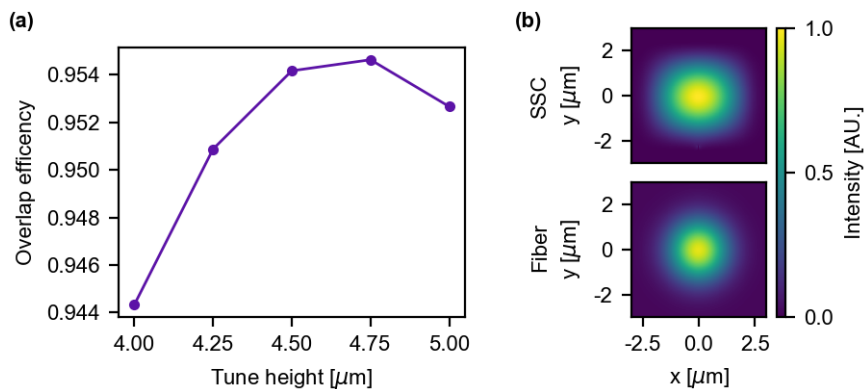


Figure 6.3: Mode overlap between the SSC and fiber. (a) Mode overlap efficiency between the SSC and cleaved fiber is calculated as a function of polymer cladding height (width). The overlap efficiency varies by less than 0.3% for heights in the range $4.5 - 5.0\ \mu\text{m}$. (b) Calculated mode field intensity profile of the SSC (width and height are $5.0\ \mu\text{m}$) and measured mode field intensity of cleaved fiber (SM800G80 Thorlabs, single mode fiber) are shown.

its refractive index is lower than the polymer. Specifically, we used NOA81 (Norland Optical Adhesive by Norland Products Inc.) whose refractive index at room temperature is $n \approx 1.54$ for 930 nm wavelengths. Figure 6.2 highlights each individual component of the long SSC design by showing the epoxy polymer cladding microfluidic channel walls, through which optical adhesive is dispensed. Finite element method (FEM) calculation are used to optimize the SSC design parameters, as well as to check robustness against cleanroom variations. Figure 6.3.a shows the mode overlap efficiency (at the near field) between the SSC and the cleaved fiber as a function of polymer cladding height (width). As well as, the mode profiles of the SSC is calculated and cleaved fiber is measured, whose beam spot shapes are illustrated in Figure 6.3.b.

The advantage of using the adhesive is two-fold: (1) it prevents waveguides from collapsing and simultaneously, and (2) it enables direct gluing to the fiber array. The proposed interface between a fiber array and SSC array is artistically depicted in Figure 6.1, where the inset (left) shows the cross section image of the design. The inset shows the calculated mode profile of the overlay waveguide when the adhesive fills two small channels on the sides by capillary forces.

6.1.2 Device fabrication

To cleanly and reproducibly infiltrate the adhesive prior to curing, we employ a microdeposition technique that relies on capillary forces to distribute the adhesive homogeneously. The fabrication steps, shown schematically in Figure 6.4 are similar to those described in Chapter 2 and built on GaAs wafer, grown by molecular beam epitaxy (process details are listed in Appendix A.2). Following the initially deposited alignment markers (see Fig. 6.4.a) are used for precise alignment of the shallow-etched grating couplers (SEG) to GaAs waveguides and to the epoxy polymer. Electron beam (e-beam) lithography technique is used to fabricate the SEG (see Fig. 6.4.b) and GaAs circuit (Figure 6.4.c), followed by dry and wet etching (Midolo et al., 2015). A commercial epoxy polymer resin mr-DWL5 (Microresist GmbH) is used to coat the wafer with a final thickness of 4.75 μm . The epoxy polymer is as a negative resist with sensitivity to both ultra-violet light (i-line) and electron beams (del Campo & Greiner, 2007; Wahlbrink et al., 2009). By using electron beam lithography in an Elionix F-125 system (acceleration voltage 125 keV and a uniform dose of 5 $\mu\text{C}/\text{cm}^2$), we achieved enabling smooth and vertical patterning of the waveguide cladding and microchannel walls with small (< 20 nm) alignment errors. After e-beam patterning, the polymer is hard baked to make it permanent on the substrate. The epoxy polymer fabrication is shown in Figure 6.4.d.

Several issues were encountered during the fabrication, which are summarized in the following:

- Proximity effect correction for such thick resist is required to compensate for the forward scattering, which typically leads to side ‘wings’ around the designed patterns (see Fig.6.5).

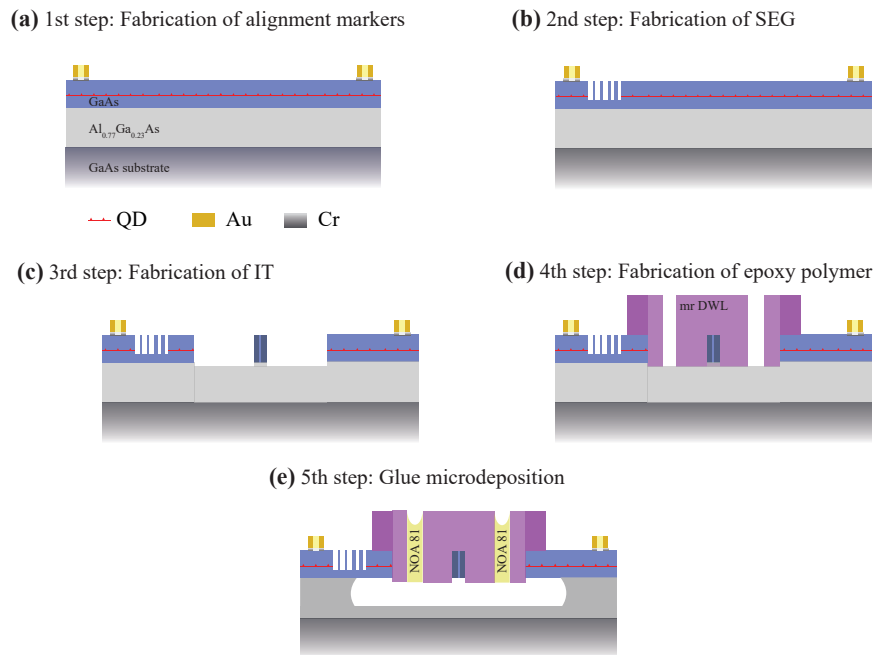


Figure 6.4: Schematics of the fabrication process flow. (a) The layer structure of the GaAs wafer used for fabricating. An InAs QD layer is embedded into an intrinsic layer of GaAs with 160 nm thickness. (b) The alignment markers are defined on a sample coated with a positive tone resist by utilizing e-beam lithography. To ensure the alignment between the subsequent e-beam lithography steps, Cr/Au alignment markers are deposited through a lift-off process. (c) The second e-beam lithography step is used to pattern shallow-etched grating couplers, which are then formed by the following dry etching (RIE) process. (d) GaAs waveguides, inverted tapers, loop mirrors are formed at the third e-beam process step, followed by another RIE step. (e) The third e-beam process patterns the epoxy polymer cladding, as well as the support structures (cladding micro-channel walls and tethers) are formed. The epoxy polymer is hard-baked to form the cladding permanently linked on the substrate. (e) The UV curable adhesive (NOA81) is infiltrated and cured with UV light. A thermal treatment process is additionally applied to increase the resistance for the further chemical process. Sample is cleaved to leave the SSC output ports at the endface of the chip and device is released in HF acid solution. Final critical point drying is used to prevent structural deformation.

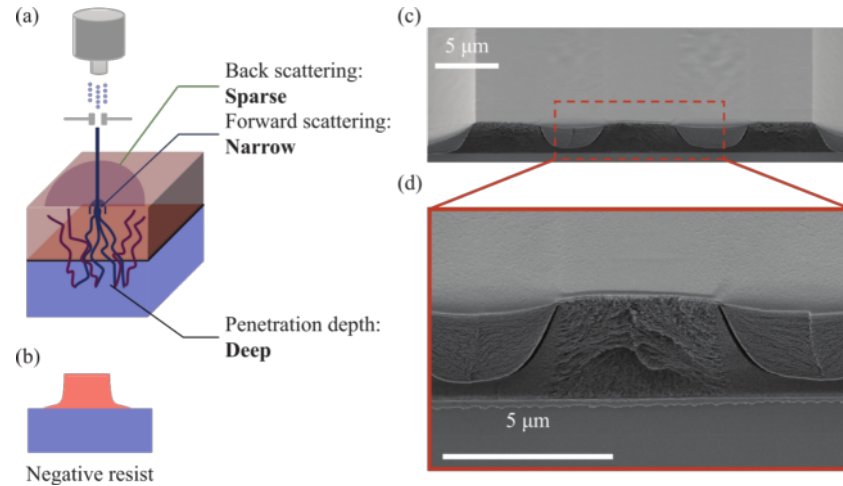


Figure 6.5: Electron forward scattering effect on the negative-tone e-beam resist. (a) Electron beam broadening effect due to the forward scattered electrons. (b) Slide-like sidewall formation at the sides of the polymer cladding as a result of forward scattering. (c) SEM image presents the resulting features of the exposed polymer structures, which are widened at the base from the forward scattered electrons. For close patterns this leads to a feature overlap. (d) Zoomed in SEM image of the overlay waveguide (from c.) with the broadened side features (slide-like sidewalls).

- An adhesion promoter (Omniccoat, from MicroResist GmbH) is needed to ensure the successful yield of microchannels with high aspect ratio (e.g. 5:1 height to width).
- To ensure fully-suspended waveguide after HF undercut, trenches were implemented and optimized. These trenches are visible in Figure 6.2, as small boxes. They need to be placed sufficiently close to each other to achieve complete undercut.

The final fabrication step is dispensing the optical adhesive and diffusing it through the glue micro-channels, with the end result shown in Figure 6.4.e. After the photosensitive adhesive is infiltrated (see Fig. 6.6.a), it is cured by 405 nm UV light for approximately 90 s. Next, thermal curing is needed to achieve a permanent glue deposition (see Fig. 6.6.b). Subsequently, the sample is cleaved and undercut using HF. We note that the controlled glue micro-deposition technique employed here ensures that the undercut trenches are not covered, thereby allowing for a sufficient etch of the sacrificial layer to complete the release step.

Figure 6.7 shows the setup for aligning chips to fiber arrays. With this setup, permanent gluing between chip and fiber can be performed. Our setup is capable of alignment precision better than 20 nm. It consists of two pairs of 3-axis stages, each piezo-controlled to allow accurate alignment. Two pitch and yaw stages are included to allow for off-axis rotation adjustments. Custom holders were made for both the fiber

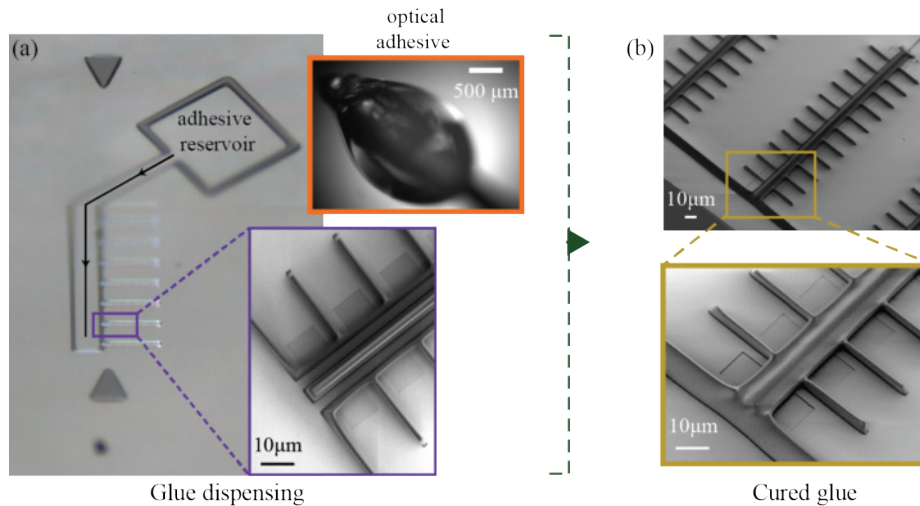


Figure 6.6: Optical glue microdeposition. (a) GaAs sample is patterned with the adhesive reservoir for dispensing the UV curable glue, utilizing a twisted wire (orange framed inset). This optical adhesive firstly fills the main glue channel (following the arrow) and benefits from the hydrophilic surface of the GaAs. Next, optical adhesive is diffused through the glue micro-channels (purple framed inset) via the capillary forces. (b) UV-cured and thermally treated optical glue guarantees the permanent formation of the long SSC structures. Zoom in image shows the completely infiltrated and cured optical glue, cladding the epoxy polymer cladding.

array and the GaAs chip. After optical alignment, the same adhesive used to infiltrate the chip during fabrication is deposited at the edge with a twisted metallic wire. A single drop of glue diffuses by capillary forces and fill the gaps between the array and the chip. At this point, it is still possible to re-adjust the alignment before UV curing. The latter is carried out using a set of UV light-emitting diodes surrounding the setup (Fig.6.8).

Using this method, a maximum chip-to-fiber coupling of 1% was observed. The poor coupling efficiency is likely due to imperfections in the sample cleaving, which resulted in a rough and dirty facet. However, the gluing process was successful and the samples have been cooled down to liquid nitrogen temperatures (77 K) without any visible mechanical failure. Future work will require an improved cleaving technique, as very thick polymers do not follow the crystallographic direction of GaAs. A potential solution is to use a focused ion beam, or another similar tool, that allows improved precision for the sample cutting without roughness.

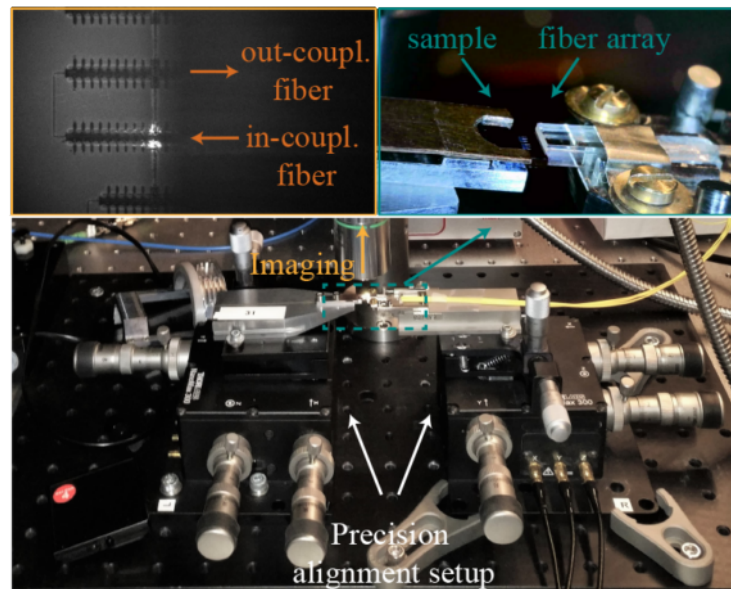


Figure 6.7: Setup for bonding of fiber arrays to GaAs chip. Alignment setup is used for positioning chip with respect to the fiber array while optimizing the transmission efficiency between the fiber array and the SSC (top left inset). The optical adhesive is dispensed from the edge of the chip and cured to form a permanent pigtailed. The setup should enable an alignment precision between waveguides and fibers below 200 nm. Fiber array pigtailed and cured GaAs chip is shown in the top right inset.

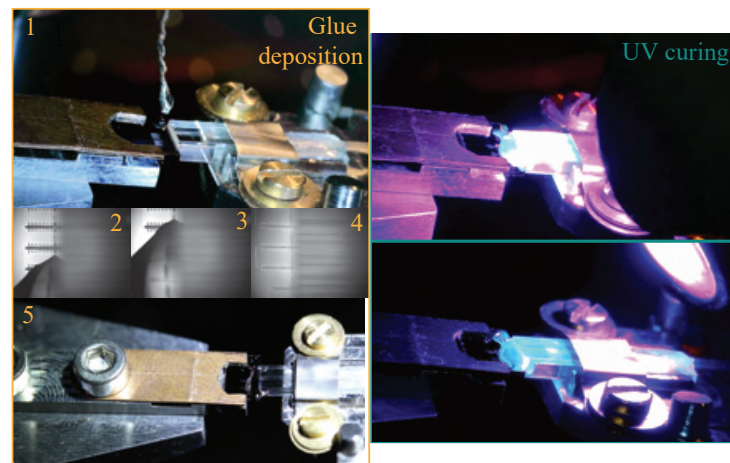


Figure 6.8: Procedural depiction of the process to add NOA81 adhesive to epoxy polymer claddings, from deposition through the microfluidic channels to the final UV curing step. Details provided in text.

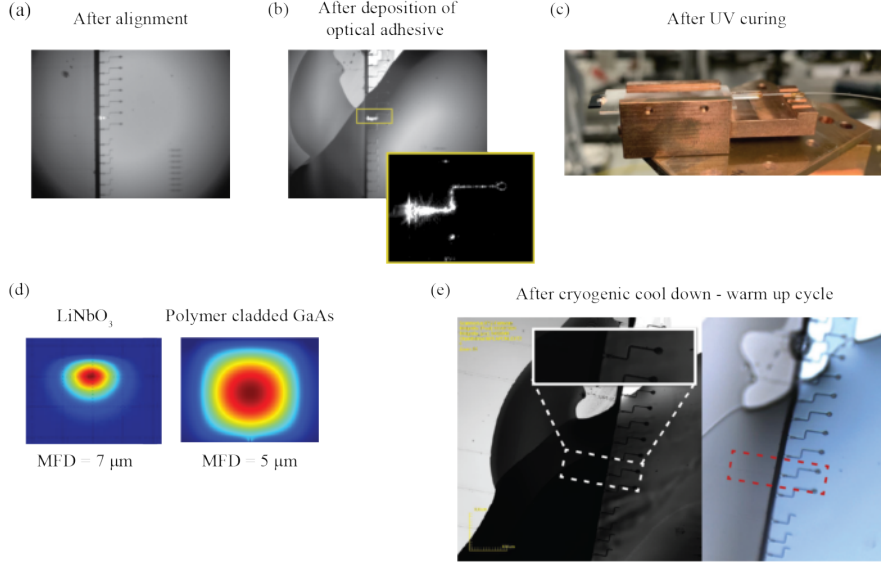


Figure 6.9: Abridged fabrication process for multiport SSC on GaAs and LN waveguides. (a) Optical micrograph representing LN (left) and GaAs (right) chips after initial alignment. The transmission efficiency is optimized through power measurements (preliminary optimization process). Laser light is transmitted from the fiber pigtailed LN waveguide to GaAs waveguide, that is terminated by a loop mirror reflector. Collected, reflected power signal is utilized for alignment optimization. (b) Optical micrograph during the glue diffusion on the GaAs - LN. Inset shows the light coupled to the GaAs waveguide, through scattered signal on the device. (c) After chip-to-chip bonding is achieved (after glue is cured). (d) Mode field profiles of the Ti:LN and GaAs waveguides. (e) Chip-to-chip bonding (glue diffused, cured and bonded GaAs-LN) is tested for cryogenic compatibility by cooling down to 0.8K and warming up.

6.2 OUTLOOK

The multi-port optical interfaces investigated in this thesis can be potentially used for the realization of hybrid platforms by directly interfacing photonic integrated circuits on different chips (i.e. without using fibers). I have studied the feasibility of such hybrid integration during a short external stay at University of Paderborn (Germany) in the Mesoscopic Quantum Optics group of Prof. Tim Bartley, which develops photonic integrated circuits based on Ti:LN waveguides (Höpker et al., 2019). The MFD of such waveguides is roughly $7\ \mu\text{m}$ wide, which makes the design of SSC in GaAs even more demanding. Nevertheless, I was able to experiment with the glue deposition techniques and interface a GaAs source to a LN circuit (Figure 6.9). To our knowledge, this is the first attempt at realizing a fiberless coupling between GaAs and LN. Moreover, the strength of the adhesive has been tested down to millikelvin temperatures, without damage, suggesting that the materials chosen for the SSC are indeed suitable for quantum applications. More work is needed, however, to demonstrate a good coupling efficiency, which is key in quantum applications that involve single photons.

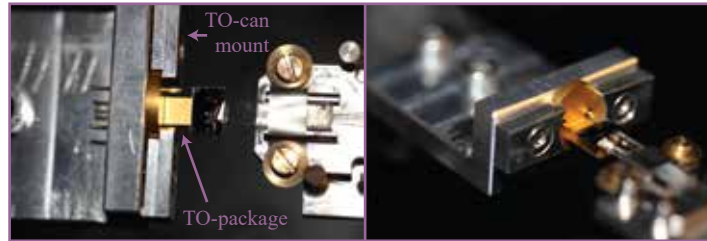


Figure 6.10: Device packaging idea. (Left) shows the hermetic, transistor outline (TO)-can mounted on the custom made mount. GaAs chip is placed on the submount and fiber array is placed on the fiber holder. (Right) angled view of the pigtailed, packaged GaAs chip.

Demonstrating fiberless coupling between GaAs and LN is but one of many potential applications for our fabrication methods. For example, one could envision coupling to other single photon emitters embedded in other host structures, leading to interfacing emitters of radically different types, mediated by spot-size converters. Moreover, by combining the waveguide-integrated single-photon source with resonant excitation illustrated in Chapters 4 and 5 of this thesis, a fully packaged and pigtailed source can be realized. Figure 6.10 shows the ongoing effort in establishing a fully packaged coherent and deterministic single-photon sources based on waveguides (see Fig. 6.10). The work presented here constitutes the first important step towards ensuring that all materials involved are compatible with the bonding process, the pigtailed, and cryogenic operation.



CONCLUDING REMARKS

In this project, we tackle the challenge of interfacing functional quantum photonic waveguide circuits. Interfacing waveguides between photonic integrated circuits across different material platforms requires mode adapters, irrespective of whether the goal is to perform chip-to-fiber out-coupling or chip-to-chip bonding.

While a diverse range of chip-to-fiber coupling solutions have been explored in the literature (e.g. waveguide tapers, grating couplers, and evanescent couplers), a one-size-fits-all solution does not yet exist. In particular, quantum photonic circuits demand cryogenic compatibility of all the materials involved, to ensure coherent quantum emission from, e.g., quantum dots. Directly addressing the interfacing of heterogeneous platforms, both to exploit the advantages of each and to understand the fundamental limits in coupling the disparate systems, has been the main objective of this work.

A summary of the key outcomes of the thesis is below:

1. Efficient spot-size converters (SSC) have been successfully implemented in planar nanostructures using a novel fabrication method that integrates optical polymers with suspended waveguides. A reproducible polymer fabrication process is introduced for the suspended GaAs circuitry. A QD-based single-photon source terminated by a optical polymer cladded inverted taper SSC for photon (single-photon) out-coupling into a lensed optical fiber was realized with coupling efficiency $\eta > \approx 48\%$. The single-photon nature of the emission is confirmed by second-order correlation measurement with $g^{(2)}(0) = 0.015 \pm 0.002$.
2. Waveguide-based in-plane resonance fluorescence schemes have been investigated, allowing realization of efficient and scalable excitation of the integrated quantum dot sources. The investigated method is based on the resonant excitation, generating highly coherent single-photons and enabling deterministic quantum operations. This novel resonant excitation scheme exploits the potential

of planar nanostructures. By carefully engineering the excitation and collection paths of the nanophotonic circuitry, $> 80\%$ single-photon coupling efficiency is achieved into the waveguide mode with a strong laser suppression better than $< 10^{-4}$. Consequently, the studied on-chip single-photon source device achieves high-purity $g^{(2)}(0) = 0.020 \pm 0.005$ and simultaneously high-indistinguishability $V = 96 \pm 2\%$. Next, a device design is introduced for in-plane resonant excitation that enhances suppression of the background laser signal to $\sim 10^{-8}$, boosting single-photon purity. Furthermore, the bandwidth increases by over an order of magnitude, simultaneously with an improved power budget.

3. An approach for realizing arrays of SSCs for chip-to-fiber out-coupling and chip-to-chip bonding has been implemented. A novel fabrication method based on glue microdeposition and microfluidics enabled the realization of long suspended tapers. Moreover, interfacing different waveguiding platforms has been explored using GaAs and LN circuits. Such an approach is expected to reduce interface losses and architecture complexity when compared to fiber coupling.

Alongside the novel structures presented in this thesis, the fabrication methods described in this work can be used for introducing a plethora of new functionalities in GaAs planar waveguide platforms. For example, optical polymers allow suspending entire sections of GaAs waveguides without the need of adding tethers, reducing losses. Additionally, metallic wire networks could be created by using polymer insulation layers for creating near-zero loss waveguide-to-wire crossings and wire-to-wire crossings. The latter is an essential building block to realize scalable electrical interconnects on-chip. Finally, thanks to the compatibility of these polymers with aggressive chemicals such as hydrofluoric acid, polymer structures can be used as protection for electrical contacts or to perform a full encapsulation of the chip to protect it from dust and oxidation.

In conclusion, this work highlights the important role of nanofabrication in developing novel solutions to the challenge of interfacing disparate quantum photonic systems. In the future, a suite of dedicated, mutually compatible, devices can be envisioned with clear prospects for integration, standardization and even commercialization.



DEVELOPED NANOFABRICATION RECIPES

A.1 EPOXY CLADDED INVERTED TAPER WAVEGUIDES

I. Exposing Alignment Markers

- 1) **Pre-clean the wafer:** Flush the sample with acetone, IPA, and lastly millipore (MQ) water (each for 2 min @37 kHz and 80 %). Blow dry with N₂, then perform dehydration bake at 185 °C for 5 min on hotplate.
- 2) **Spin-coat ZEP520A (60 µL) resist:** Spin resist at 2000 rpm for 60 s (static dispense, acc. 1000rpm). Soft bake for 5 min on a hotplate at 185 °C.
- 3) **Electron Beam Lithography:** For the 125 keV machine, expose with proximity effect correction (PEC) and the following parameters:

	Alignment Markers
Beam Current:	1 nA
Clearing Dose:	350 µC/cm ²
Numerical Aperture:	120 µm
Write Field:	500 µm
Feed Pitch (scan pitch):	10 dots (5 nm)
Dot number:	10 ⁶ dots
Dwell Time (dose time):	0.0875 µs

- 4) **Room temperature Development:** Develop exposed sample in chilled n-Amyl acetate for 60 s, then in IPA for 10 s. Blow dry with N₂.
- 5) **Surface Preparation with O₂ Plasma:** Perform O₂ plasma on dried sample for 30 s (50 W RF, 3 mbar). This removes organic residues from the exposed/developed regions, as well as 'activates' the surface prior to metal deposition.

- 6) **Deposition of Ti/Au marks by E-beam evaporation:** Deposit a 50 Å adhesive layer of Ti at a rate of 2 Å/s, with accelerating voltage 6 kV and beam current 0.03 A. Without breaking vacuum, deposit 850 Å of Au at a rate of 1 Å/s, with accelerating voltage 6 kV and beam current 0.10 A. For both depositions, the chamber pressure should be at or below 1×10^{-7} mbar.
- 7) **Resist Lift-off with 1-methyl-2-pyrrolidone (NMP):** Perform initial lift-off with NMP heated to 80 °C, 10 min. Sonicate for 2 minutes (80 kHz, 40% intensity) to complete lift-off, then transfer to room-temperature NMP for rinsing, 30 s. Rinse with IPA squirt-bottle and blow dry with N₂.

II. Patterning GaAs nanostructures and Etch monitor:

- 1) **Substrate Preparation:** Flush the sample with acetone, IPA, millipore water, then N₂ blow dry.
- 2) **Ti Evaporation:** Evaporate 20 Å Ti on surface to improve surface adhesion.
- 3) **Spin Coat CSAR:** Spin resist at 2000 rpm for 60 s (static dispense). Soft bake for 5 min on hotplate at 185 °C.
- 4) **Electron Beam Lithography:** For the 125 keV machine, expose with PEC. The photonic circuit and etch monitor patterns use different EBL parameters, as follows:

	Circuit	Etch Monitor
Beam Current:	1 nA	20 nA
Clearing Dose:	350 μC/cm ²	400 μC/cm ²
Numerical Aperture:	120 μm	120 μm
Write Field:	500 μm	500 μm
Feed Pitch (scan pitch):	8 dots (4 nm)	40 dots (8 nm)
Dot number:	10 ⁶ dots	10 ⁶ dots
Dwell Time (dose time):	0.056 μs	0.08 μs

- 5) **Cold Development:** Develop exposed sample in chilled n-Amyl acetate (-5 °C) for 30 s, then chilled IPA (-5 °C) for 20 s. Blow dry with N₂.
- 6) **Dry Etching:** Mount the sample to the Si carrier wafer using a small drop of Fomblin oil. This establishes thermal conductivity between the backside cooling gas and the sample through the carrier wafer, necessary for a stable etch rate. A standard BCl₃/Ar etch process is then performed using the following parameters:
 - BCl₃ flow: 5 sccm
 - Ar flow: 10 sccm
 - Chamber Pressure: 0 mTorr
 - Temperature: 0 °C
 - ICP power: 0 W
 - RF power: 25 W

- DC bias: 159 V

End point detection is used to stop the process after etching completely through the 160 nm GaAs layer, and then a further 10 nm into AlGaAs sacrificial layer.

- 7) **Resist Strip with NMP:** Strip resist with NMP heated to 70 °C, 10 min. Transfer to room-temperature NMP for rinsing, 20 min. Rinse with IPA squirt-bottle and blow dry with N₂.
- 8) **Ti Strip with HF:** HF 1% dip for 3 s, MQ water 10 s, MQ water for 30 s, IPA dip for 10 s.

III. Patterning Epoxy cladding on GaAs nanostructures

- 1) **Substrate Preparation:** Ensure that the sample is clean from all possible residues. If necessary, use O₂ plasma followed by phosphoric acid etch to clean the surface. Normally, clean the sample first by using agitation with acetone (2 min), then IPA (2 min), and lastly MQ (2 min). Blow dry with N₂.
- 2) **Spin coat EpoCore2:** A multi-step spin recipe is used to obtain a target thickness of 1.15 μm. Spin at (1) 8000 rpm for 10 s (static dispense, acc. 6000 rpm), then (2) 3750 rpm for 60 s (static dispense, acc. 1750 rpm).
- 3) **Ramped Soft Bake:** The multi-step soft bake for EpoCore2 resist starts with 2 min bake at 50 °C, and ends with a 2 min bake at 90 °C. The temperature is ramped over 340 s by programmable hotplate.
- 4) **Electron Beam Lithography:** For the 125 keV machine, expose without PEC and the following parameters:

	EpoCore2
Beam Current:	0.5 nA
Clearing Dose:	9 μC/cm ²
Numerical Aperture:	120 μm
Write Field:	500 μm
Feed Pitch (scan pitch):	40 dots (20 nm)
Dwell Time (dose time):	0.072 μs
Dot number:	10 ⁶ dots
Dose Coefficient (schedule file)	0.75

- 5) **Ramped Post-exposure bake (PEB), with cooldown:** The multi-step PEB for EpoCore2 resist starts with 2 min bake at 50 °C, and ends with a 3 min bake at 85 °C. The temperature is ramped over 170 s by programmable hotplate. The sample cools for 40 min before continuing.
- 6) **Development:** Develop using mr-Dev 600, 60 s with agitation. Rinse with IPA then MQ, both for 30 s with agitation.

- 7) **Ramped Hard Bake:** The multi-step hard bake for EpoCore2 resist starts with 2 min bake at 90 °C, and ends with a 20 min bake at 130 °C. The temperature is ramped over 600 s by programmable hotplate.
- 8) **Residue Removal with O₂ Plasma:** 10 min, 100RF
- 9) **Cleave:** Indent and cleave to leave the flat polymer out-coupler interface at the chip edge.
- 10) **Undercut:**
 - i. 30 sec in 5% HF (5 mL HF (40%):35 mL MQ), 10 s MQ, 1.5 min MQ, 3.5 min MQ, 5 min MQ.
 - ii. 1 min in H₂O₂, 10 s MQ, (the warm-bath was set to 35 °C before the undercut process started-45 °C was read), 2.5 min warm MQ, 3.5 warm MQ, 9 min warm MQ.
 - iii. 30 sec in 1:10 HCl (5 ml HCl 37%: 50ml MQ), 10 s MQ, 1.5 min MQ, .5 MQ, 5 min MQ.
 - iv. IPA beakers: 10 s, then 1.5 (remove boat in 2nd beaker), 3.5 min, 5 min.

A.2 MULTIPORT EPOXY CLADDED INVERTED TAPER WAVEGUIDES WITH OPTICAL ADHESIVE

I. Exposing Alignment Markers

- 1) **Pre-clean the wafer:** Flush the sample with acetone, IPA, and lastly millipore (MQ) water (each for 2 min @37 kHz and 80 W). After, blow dry with N₂ then perform dehydration bake at 185 °C for 5 minutes on a hotplate.
- 2) **Spin-coat CSAR 13 resist (60 mL):** Spin resist at 2200 rpm for 60 s (static dispense, acc. 1000rpm). Soft bake for 1 minute on a hotplate at 185 °C. Expected thickness: ~550 nm.
- 3) **Electron Beam Lithography:** For the 125 keV machine, expose with proximity error correction (PEC) and the following parameters:

	CSAR 13
Beam Current:	1 nA
Clearing Dose:	250 μC/cm ²
Numerical Aperture:	120 μm
Write Field:	500 μm
Feed Pitch (scan pitch):	8 dots (4 nm)
Dot number:	10 ⁶ dots
Dwell Time (dose time):	0.04 μs

- 4) **Room Temperature Development:** Develop exposed sample in n-Amyl acetate for 60 sec, then IPA for 10 sec. Blow dry with N₂.
- 5) **Surface Preparation with O₂ Plasma:** Perform O₂ plasma on dried sample for 30 sec (50 W RF, 3 mbar). This removes organic residues from the exposed/developed regions, as well as ‘activates’ the surface prior to metal deposition.
- 6) **Deposition of Cr/Au marks by E-beam evaporation:** Deposit a 100 Å adhesive layer of Cr Without breaking vacuum, deposit 1700 Å of Au For both depositions, the chamber pressure should be at or below 1 × 10⁻⁷ mbar.
- 7) **Resist Lift-off with 1,3-Dioxolane (I-III Diox):** Perform initial lift-off with room temperature I-III Diox, 10 minutes. Rinse with I-III Diox (pipette) until all metal layers are removed. Rinse with IPA squirt-bottle and blow dry with N₂.

II. Patterning Shallow Etch Grating (SEG) and Etch monitor:

- 1) **Substrate Preparation:** Flush the sample with acetone, IPA, MQ water, then N₂ blow dry.
- 2) **Spin Coat CSAR 9% (Target - 200 μm):** Spin resist at 4000 rpm for 60 s (static dispense). Soft bake for 1 minutes on hotplate at 185 °C.

- 3) **Electron Beam Lithography:** For the 125 keV machine, expose with PEC. The SEG and etch monitor patterns use different EBL parameters, as follows:

	SEG	Etch Monitor
Beam Current:	1 nA	20 nA
Clearing Dose:	350 $\mu\text{C}/\text{cm}^2$	400 $\mu\text{C}/\text{cm}^2$
Numerical Aperture:	120 μm	120 μm
Write Field:	500 μm	500 μm
Feed Pitch (scan pitch):	8 dots (4 nm)	40 dots (8 nm)
Dot number:	10^6 dots	10^6 dots
Dwell Time (dose time):	0.0512 μs	0.08 μs

- 4) **Cold Development:** Develop exposed sample in chilled n-Amyl acetate (-5°C) for 40 sec, then chilled IPA (-5°C) for 20 sec. Blow dry with N_2 . (**Note: Prepare the cold bath 1 hour in advance. Use the target parameters but don't forget to blow N_2 under the Al plate.**)

- 5) **Dry Etching:** Mount the sample to the Si carrier wafer using a small drop of Fomblin oil. This establishes thermal conductivity between the backside cooling gas and the sample through the carrier wafer, necessary for a stable etch rate. A standard BCl_3/Ar etch process is then performed using the following parameters:

- BCl_3 flow: 5 sccm
- Ar flow: 10 sccm
- Chamber Pressure: 0 mTorr
- Temperature: 0°C
- ICP power: 0 W
- RF power: 25 W
- DC bias: 159 V

End point detection is used to aim for an **etch depth of 90 nm**.

- 6) **Resist Strip with NMP:** Strip resist with NMP heated to 70°C , 10 min. Transfer to room-temperature NMP for rinsing, 20 min. Rinse with IPA squirt-bottle and blow dry with N_2 .

III. Patterning GaAs circuit and Etch monitor:

- 1) **Substrate Preparation:** Flush the sample with acetone, IPA, MQ water, then N_2 blow dry.
- 2) **Coat Adhesion Layer:** Spin AR-30080 at 4000 rpm for 60 s (static dispense). Soft bake for 2 min on hotplate at 115°C . I-III Diox (2 min) + Acetone (2 min) + IPA (2 min)
- 3) **Spin Coat CSAR 9% (Target - 200 μm):** Spin resist at 4000 rpm for 60 s (static dispense). Soft bake for 1 min on hotplate at 185°C .

- 4) **Electron Beam Lithography:** For the 125 keV machine, expose with PEC. The SEG and etch monitor patterns use different EBL parameters, as follows:

	Circuit	Etch Monitor
Beam Current:	1 nA	20 nA
Clearing Dose:	350 $\mu\text{C}/\text{cm}^2$	400 $\mu\text{C}/\text{cm}^2$
Numerical Aperture:	120 μm	120 μm
Write Field:	500 μm	500 μm
Feed Pitch (scan pitch):	8 dots (4 nm)	40 dots (8 nm)
Dot number:	10^6 dots	10^6 dots
Dwell Time (dose time):	0.0512 μs	0.08 μs

- 5) **Cold Development:** Develop exposed sample in chilled n-Amyl acetate (-5°C) for 40 s, then chilled IPA (-5°C) for 20 s. Blow dry with N_2 .
- 6) **Dry Etching:** Mount the sample to the Si carrier wafer using a small drop of Fomblin oil. This establishes thermal conductivity between the backside cooling gas and the sample through the carrier wafer, necessary for a stable etch rate. A standard BCl_3/Ar etch process is then performed using the following parameters:
- BCl_3 flow: 5 sccm
 - Ar flow: 10 sccm
 - Chamber Pressure: 0 mTorr
 - Temperature: 0°C
 - ICP power: 0 W
 - RF power: 25 W
 - DC bias: 159 V

End point detection is used to stop the process after etching completely through the 160 nm GaAs layer, and then a further 10 nm into AlGaAs sacrificial layer.

- 7) **Resist Strip with NMP:** Strip resist with NMP heated to 70°C , 10 min. Transfer to room-temperature NMP for rinsing, 20 min. Rinse with IPA squirt-bottle and blow dry with N_2 .

IV. Patterning Epoxy cladding on GaAs nanostructures

- 1) **Substrate Preparation:** Agitate sample in acetone, then IPA, and lastly MQ water - for 2 minutes each. Blow dry with N_2 . Additionally, perform a 5 min dehydration bake on a hotplate set to 185°C , then let cool for 10 min.
- 2) **Coat Adhesion Layer:** Spin OmniCoat at 3000 rpm for 45 s (static dispense). Soft bake for 2 min on hotplate at 115°C , then let cool for 5 min.
- 3) **Spin coat mrDWL5 (4.75 μm):** Spin mrDWL5 at 3000 rpm for 30 s (static dispense, 1000 rpm acce.).

- 4) **Ramped Soft Bake:** The multi-step soft bake for mrDWL5 starts with 2 min bake at 50 °C, and ends with a 2 min bake at 90 °C. The temperature is ramped over 340 s by programmable hotplate. The sample cools for 30 min before continuing.
- 5) **Electron Beam Lithography:** For the 125 keV machine, expose with PEC and the following parameters:

	mr-DWL5
Beam Current:	0.1 nA
Clearing Dose:	5 $\mu\text{C}/\text{cm}^2$
Numerical Aperture:	120 μm
Write Field:	500 μm
Feed Pitch (scan pitch):	16 dots (8 nm)
Dot number:	10^6 dots
Dwell Time (dose time)	0.032 μs
Dose Coefficient (schedule file)	0.8

- 6) **Ramped Post-Exposure Bake (PEB):** The multi-step PEB for mrDWL5 starts with 2 min bake at 50 °C, and ends with a 4 min bake at 90 °C. The temperature is ramped over 250 s by programmable hotplate. The sample cools for 30 min before continuing.
- 7) **Development:** Develop using mr-Dev 600 for 4 min, including agitation for the first 1 min. Rinse with IPA for 3600 s, then agitate for 2 min. Finally, rinse in MQ water for 30 s with agitation.
- 8) **Ramped Hard Bake:** The multi-step hard bake for EpoCore2 resist starts with 2 minute bake at 90 °C, and ends with a 20 min bake at 130 °C. The temperature is ramped over 600 s by programmable hotplate.
- 9) **Residue Removal with O₂ Plasma:** 600 sec, 100RF

V. Glue Deposition:

- 1) **Microdeposition of NOA 81:** Deposit glue on the patterned glue reservoir (see Fig. 6.6) by using a twisted wire to transfer the adhesive. Wait for the deposited adhesive to diffuse to the glue channels. The sample is placed on a vacuum holder and white light is used to increase the diffusion rate.
- 2) **UV Curing:** After the glue channels are completely filled with the optical glue (confirmed under optical microscope) a hand held UV gun (Lumatec SUPERLIGHT 01@ 370 nm) is focused on the sample for 60 s from approx. 10 mm distance.
- 3) **Hard Bake:** A multi-step bake is applied on the cured NOA 81. Starting with 10 min bake at 90 °C, and ends with a 12 hour bake at 130 °C. The temperature is ramped over 600 s by programmable hotplate.

VI. **High Accuracy Cleaving:** To leave the spot-size converter (SSC) end faces at the chip edge, Loomis indent and pressure cleave is used with the following parameters:

- Applied pressure: 0.55 psi (optimized for avoiding high edge roughness)
- Tool alignment correction: 0.04 μm

VII. **Release the membrane layer using liquid HF:**

- 1) **HF dip to remove sacrificial layer:** Dip sample in 5% HF (5 mL HF:35 mL MQ) for 30 s. Clean with a succession of rinses of MQ water - 10 s, 1.5 min, 3.5 min, 5 min.
- 2) **Oxidation with H_2O_2 :** Dip sample in H_2O_2 for 1 min. Clean with a succession of rinses of warm MQ water ($\sim 40^\circ\text{C}$) - 10 s, 2.5 min, 3.5 min, 9 min.
- 3) **Residue removal with HCl:** Dip oxidized sample in 1:10 HCl (5 mL HCl 37%: 55 mL MQ) for 30 s. Clean with a succession of rinses of MQ water - 10 s, 1.5 min, 3.5 min, 5 min.
- 4) **Final IPA Clean:** At last, clean with a succession of IPA rinses - 10 s, 1.5 min, 3.5 min, 5 min.

APPENDIX



HETEROSTRUCTURE COMPOSITION AND SAMPLE FABRICATION

The samples detailed in Chapter 4 are fabricated on a GaAs heterostructure grown by molecular beam epitaxy on $\langle 100 \rangle$ GaAs substrates. Wet etching releases the composition into a membrane through removal of an 1150 nm thick $\text{Al}_{0.75}\text{Ga}_{0.25}\text{As}$ sacrificial layer. The heterostructure layers are shown in Fig. B.1, exhibiting an AlAs layer containing self-assembled InAs quantum dots (QDs) embedded in a p - i - n diode to enable control of the charge state and Stark tuning of each emitter. The 53 nm $\text{Al}_{0.3}\text{Ga}_{0.7}\text{As}$ barrier layer limits the current to \sim few nA when the diode is operating under forward bias.

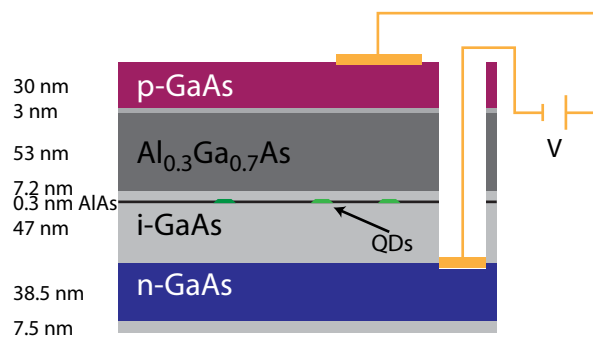


Figure B.1: Layout of the p - i - n diode heterostructure utilized to build the in-plane resonance fluorescence single-photon source device.

Electrical contacts to the n -doped layer are fabricated first, starting with RIE to open the via to the buried n -layer. Then, $Ni/Ge/Au$ contacts are deposited by electron-beam physical vapor deposition. This is followed by 430 °C annealing to ensure homogeneity of the Ge-Au eutectic alloy. Subsequently, Cr/Au contacts are deposited on the surface to form Ohmic p -type contacts; no annealing is required. At last, the waveguides are patterned using EBL and etched by ICP-RIE using $BCl_3/Cl_2/Ar$ chemistry. The sacrificial layer is finally removed with HF and cleaned, as detailed in Ref. (Midolo et al., 2015).



RESONANCE FLUORESCENCE OF A TWO-LEVEL EMITTER

We model the quantum dot as a two-level system with a ground state $|g\rangle$ and an excited state $|e\rangle$. The energy levels are separated in energy by $\hbar\omega_{\text{qd}}$. The two levels are coupled with rate Ω by a monochromatic laser detuned from the quantum dot resonance by $\Delta = \omega_{\text{L}} - \omega_{\text{qd}}$. The coupling rate Ω is also commonly called Rabi frequency. In the next paragraphs, we will briefly describe how we model the dynamics induced by the laser field, as well as the decoherence processes of spontaneous emission and dephasing.

The Hamiltonian of the light-matter system, in the rotating wave approximation and in a rotating frame with the laser frequency, is written as [cite]

$$\hat{H}_{\text{s}} = \hat{H}_{\text{qd}} + \hat{H}_{\text{int}} = \hbar\Delta\hat{\sigma}_{\text{ee}} + \hbar\Omega(\hat{\sigma}_{\text{eg}} + \hat{\sigma}_{\text{ge}}), \quad (\text{C.1})$$

where $\hat{\sigma}_{ij} = |i\rangle\langle j|$ are the operators in the $i, j = \{|g\rangle, |e\rangle\}$ basis. The first term in equation C.1, \hat{H}_{qd} , represents the energy of the quantum dot system, and the term \hat{H}_{int} represents the coupling of the system with the laser field.

In reality, the quantum dot is also coupled to its electromagnetic surroundings. A common approach to model such interactions leads to the master equation for the density operator ρ

$$\dot{\rho}(t) = -i[\hat{H}_{\text{s}}, \rho] + \sum_k \hat{L}_k \rho \hat{L}_k^\dagger - \frac{1}{2} \left(\hat{L}_k^\dagger \hat{L}_k \rho + \rho \hat{L}_k^\dagger \hat{L}_k \right), \quad (\text{C.2})$$

written in the $\{|g\rangle, |e\rangle\}$ basis. The density operator relates to the operators of the system via $\rho_{ij} \equiv \langle \hat{\sigma}_{ij} \rangle = \text{Tr}[\rho \hat{\sigma}_{ij}]$. The operators \hat{L}_k are the jump operators related to the couplings to the environment. These couplings lead to the loss of coherence over time. In the present case, we will consider the effects of spontaneous emission, modelled by $\hat{L}_{\text{se}} = \sqrt{\gamma}\hat{\sigma}_{\text{ge}}$, and pure dephasing, accounted via the jump operator $\hat{L}_{\text{d}} = \sqrt{\gamma_{\text{d}}}(\hat{\sigma}_{\text{gg}} + \hat{\sigma}_{\text{ee}})$.

Inserting C.1 and the jump operators in the master equation C.2, we calculate the time evolution of the density matrix elements. In the matrix form, we can write

$$\dot{\rho}(t) = \mathbf{M}\rho(t), \quad (\text{C.3})$$

where the matrix \mathbf{M} is

$$\mathbf{M} = \begin{pmatrix} 0 & \frac{i\Omega}{2} & -\frac{i\Omega}{2} & \gamma \\ \frac{i\Omega}{2} & -\frac{\gamma+2\gamma_d}{2} + i\Delta & 0 & -\frac{i\Omega}{2} \\ -\frac{i\Omega}{2} & 0 & -\frac{\gamma+2\gamma_d}{2} - i\Delta & \frac{i\Omega}{2} \\ 0 & -\frac{i\Omega}{2} & \frac{i\Omega}{2} & -\gamma \end{pmatrix} \quad (\text{C.4})$$

and the density operator is

$$\rho(t) = \begin{pmatrix} \rho_{gg}(t) \\ \rho_{ge}(t) \\ \rho_{eg}(t) \\ \rho_{ee}(t) \end{pmatrix}. \quad (\text{C.5})$$

The variables $\rho_{gg}(t)$ and $\rho_{ee}(t)$ are the ground and the excited state populations, respectively, and $\rho_{ge}(t)$ and $\rho_{eg}(t)$ describe the coherence between the states. The solution to equation C.3 is

$$\rho(t) = e^{\mathbf{M}t} \rho(t_0), \quad (\text{C.6})$$

where $\rho(t_0)$ is the density matrix at the initial time.

Under pulsed resonant excitation, the coupling rate is time dependent. For the case of a pulse with Gaussian profile, we write

$$\Omega(t) = \frac{\Theta}{\sqrt{\pi}\sigma} e^{-(t-t_0)^2/\sigma^2}. \quad (\text{C.7})$$

In this scenario, equation C.3 is solved numerically.

BIBLIOGRAPHY

- Aghaeimeibodi, S., Desiatov, B., Kim, J.-H., Lee, C.-M., Buyukkaya, M. A., Karasahin, A., Richardson, C. J., Leavitt, R. P., Lončar, M., & Waks, E. (2018). Integration of quantum dots with lithium niobate photonics. *Applied Physics Letters*, *113*(22), 221102 (cit. on pp. 23, 26).
- Aharonovich, I., Englund, D., & Toth, M. (2016). Solid-state single-photon emitters. *Nature Photonics*, *10*(10), 631–641 (cit. on p. 10).
- Almeida, V. R., Panepucci, R. R., & Lipson, M. (2003). Nanotaper for compact mode conversion. *Optics letters*, *28*(15), 1302–1304 (cit. on p. 48).
- Arcari, M., Söllner, I., Javadi, A., Lindskov Hansen, S., Mahmoodian, S., Liu, J., Thyrestrup, H., Lee, E. H., Song, J. D., Stobbe, S., & Lodahl, P. (2014). Near-unity coupling efficiency of a quantum emitter to a photonic crystal waveguide. *Phys. Rev. Lett.*, *113*, 093603 (cit. on pp. 10, 15, 22, 58, 59, 67).
- Arute, F., Arya, K., Babbush, R., Bacon, D., Bardin, J. C., Barends, R., Biswas, R., Boixo, S., Brandao, F. G., Buell, D. A., et al. (2019). Quantum supremacy using a programmable superconducting processor. *Nature*, *574*(7779), 505–510 (cit. on p. 6).
- Ates, S., Ulrich, S. M., Reitzenstein, S., Löffler, A., Forchel, A., & Michler, P. (2009). Post-selected indistinguishable photons from the resonance fluorescence of a single quantum dot in a microcavity. *Phys. Rev. Lett.*, *103*, 167402 (cit. on p. 60).
- Ates, S., Ulrich, S., Ulhaq, A., Reitzenstein, S., Löffler, A., Höfling, S., Forchel, A., & Michler, P. (2009). Non-resonant dot–cavity coupling and its potential for resonant single-quantum-dot spectroscopy. *Nat. Photonics*, *3*(12), 724 (cit. on pp. 15, 60).
- Awschalom, D., Berggren, K. K., Bernien, H., Bhave, S., Carr, L. D., Davids, P., Economou, S. E., Englund, D., Faraon, A., Fejer, M., et al. (2021). Development of quantum interconnects (quics) for next-generation information technologies. *PRX Quantum*, *2*(1), 017002 (cit. on p. 8).
- Awschalom, D. D., Bassett, L. C., Dzurak, A. S., Hu, E. L., & Petta, J. R. (2013). Quantum spintronics: Engineering and manipulating atom-like spins in semiconductors. *Science*, *339*(6124), 1174–1179 (cit. on p. 7).
- Bauters, J. F., Heck, M. J., John, D., Dai, D., Tien, M.-C., Barton, J. S., Leinse, A., Heideman, R. G., Blumenthal, D. J., & Bowers, J. E. (2011). Ultra-low-loss high-aspect-ratio $3 \times 3 \times 4$ waveguides. *Optics express*, *19*(4), 3163–3174 (cit. on p. 24).

- Biberman, A., Shaw, M. J., Timurdogan, E., Wright, J. B., & Watts, M. R. (2012). Ultralow-loss silicon ring resonators. *Optics letters*, 37(20), 4236–4238 (cit. on p. 24).
- Billah, M. R., Blaicher, M., Hoose, T., Dietrich, P.-I., Marin-Palomo, P., Lindenmann, N., Nestic, A., Hofmann, A., Troppenz, U., Moehrle, M., et al. (2018). Hybrid integration of silicon photonics circuits and InP lasers by photonic wire bonding. *Optica*, 5(7), 876–883 (cit. on pp. 25, 26, 48).
- Bovington, J., Heck, M., & Bowers, J. (2014). Heterogeneous lasers and coupling to silicon near 1060 nm. *Optics letters*, 39(20), 6017–6020 (cit. on p. 48).
- Bowers, J. E., Komljenovic, T., Davenport, M., Hulme, J., Liu, A. Y., Santis, C. T., Spott, A., Srinivasan, S., Stanton, E. J., & Zhang, C. (2016). Recent advances in silicon photonic integrated circuits. *Next-Generation Optical Communication: Components, Sub-Systems, and Systems V*, 9774, 977402 (cit. on p. 48).
- Bremer, L., Weber, K., Fischbach, S., Thiele, S., Schmidt, M., Kaganskiy, A., Rodt, S., Herkommer, A., Sartison, M., Portalupi, S. L., et al. (2020). Quantum dot single-photon emission coupled into single-mode fibers with 3d printed micro-objectives. *APL Photonics*, 5(10), 106101 (cit. on pp. 27, 29).
- Briegel, H.-J., Dür, W., Cirac, J. I., & Zoller, P. (1998). Quantum repeaters: The role of imperfect local operations in quantum communication. *Physical Review Letters*, 81(26), 5932 (cit. on p. 8).
- Brown, R. H., & Twiss, R. Q. (1956). Correlation between photons in two coherent beams of light. *Nature*, 177(4497), 27–29 (cit. on pp. 13, 77).
- Buckley, S., Rivoire, K., & Vučković, J. (2012). Engineered quantum dot single-photon sources. *Reports on Progress in Physics*, 75(12), 126503 (cit. on p. 12).
- Burek, M. J., Meuwly, C., Evans, R. E., Bhaskar, M. K., Sipahigil, A., Meesala, S., Machielse, B., Sukachev, D. D., Nguyen, C. T., Pacheco, J. L., et al. (2017). Fiber-coupled diamond quantum nanophotonic interface. *Physical Review Applied*, 8(2), 024026 (cit. on p. 48).
- Burns, W. K., & Hocker, G. (1977). End fire coupling between optical fibers and diffused channel waveguides. *Applied optics*, 16(8), 2048–2050 (cit. on p. 30).
- Chen, Z., & Segev, M. (2021). Highlighting photonics: Looking into the next decade. *eLight*, 1(1), 1–12 (cit. on p. 9).
- Cohen, J. D., Meenehan, S. M., & Painter, O. (2013). Optical coupling to nanoscale optomechanical cavities for near quantum-limited motion transduction. *Optics express*, 21(9), 11227–11236 (cit. on pp. 48, 51).
- Dalgarno, P. A., Smith, J. M., McFarlane, J., Gerardot, B. D., Karrai, K., Badolato, A., Petroff, P. M., & Warburton, R. J. (2008). Coulomb interactions in single charged self-assembled quantum dots: Radiative lifetime and recombination energy. *Phys. Rev. B*, 77, 245311 (cit. on p. 17).
- Davanco, M., Liu, J., Sapienza, L., Zhang, C.-Z., Cardoso, J. V. D. M., Verma, V., Mirin, R., Nam, S. W., Liu, L., & Srinivasan, K. (2017). Heterogeneous integration for on-chip quantum photonic circuits with single quantum dot devices. *Nature communications*, 8(1), 1–12 (cit. on pp. 23, 26, 27, 30, 48).
- Daveau, R. S., Balram, K. C., Pregolato, T., Liu, J., Lee, E. H., Song, J. D., Verma, V., Mirin, R., Nam, S. W., Midolo, L., et al. (2017). Efficient fiber-coupled single-photon

- source based on quantum dots in a photonic-crystal waveguide. *Optica*, 4(2), 178–184 (cit. on pp. 27, 30, 48).
- del Campo, A., & Greiner, C. (2007). Su-8: A photoresist for high-aspect-ratio and 3d submicron lithography. *Journal of micromechanics and microengineering*, 17(6), R81 (cit. on p. 94).
- Devoret, M. H., & Schoelkopf, R. J. (2013). Superconducting circuits for quantum information: An outlook. *Science*, 339(6124), 1169–1174 (cit. on p. 7).
- Dietrich, C. P., Fiore, A., Thompson, M. G., Kamp, M., & Höfling, S. (2016). Gaas integrated quantum photonics: Towards compact and multi-functional quantum photonic integrated circuits. *Laser & Photonics Reviews*, 10(6), 870–894 (cit. on pp. 6, 12, 15, 47).
- Dietrich, P.-I., Blaicher, M., Reuter, I., Billah, M., Hoose, T., Hofmann, A., Caer, C., Dangel, R., Offrein, B., Troppenz, U., et al. (2018). In situ 3d nanoprinting of free-form coupling elements for hybrid photonic integration. *Nature Photonics*, 12(4), 241–247 (cit. on pp. 25, 26).
- Ding, X., He, Y., Duan, Z.-C., Gregersen, N., Chen, M.-C., Unsleber, S., Maier, S., Schneider, C., Kamp, M., Höfling, S., et al. (2016). On-demand single photons with high extraction efficiency and near-unity indistinguishability from a resonantly driven quantum dot in a micropillar. *Physical review letters*, 116(2), 020401 (cit. on pp. 10, 14, 15, 47).
- DiVincenzo, D., & Loss, D. (1998). Quantum information is physical. *Superlattices and Microstructures*, 23(3), 419–432 (cit. on p. 7).
- Dowling, J. P., & Milburn, G. J. (2002). Quantum technology: The second quantum revolution. *arXiv preprint quant-ph/0206091* (cit. on p. 5).
- Dreeßen, C. L., Ouellet-Plamondon, C., Tighineanu, P., Zhou, X., Midolo, L., Sørensen, A. S., & Lodahl, P. (2018). Suppressing phonon decoherence of high performance single-photon sources in nanophotonic waveguides. *Quantum Science and Technology*, 4(1), 015003 (cit. on pp. 50, 56).
- Eich, A., Spiekermann, T. C., Gehring, H., Sommer, L., Bankwitz, J. R., Schrinner, P. P., Preuß, J. A., de Vasconcellos, S. M., Bratschitsch, R., Pernice, W. H., et al. (2021). Single photon emission from individual nanophotonic-integrated colloidal quantum dots. *arXiv preprint arXiv:2104.11830* (cit. on pp. 27, 29).
- Elshaari, A. W., Pernice, W., Srinivasan, K., Benson, O., & Zwiller, V. (2020). Hybrid integrated quantum photonic circuits. *Nature Photonics*, 14(5), 285–298 (cit. on pp. 9, 10, 24).
- Elshaari, A. W., Zadeh, I. E., Fognini, A., Reimer, M. E., Dalacu, D., Poole, P. J., Zwiller, V., & Jöns, K. D. (2017). On-chip single photon filtering and multiplexing in hybrid quantum photonic circuits. *Nature communications*, 8(1), 1–8 (cit. on pp. 10, 47).
- Fan, R. S., & Hooker, R. B. (1999). Tapered polymer single-mode waveguides for mode transformation. *Journal of lightwave technology*, 17(3), 466 (cit. on p. 48).
- Fischer, K. A., Hanschke, L., Kremser, M., Finley, J. J., Müller, K., & Vučković, J. (2017). Pulsed rabi oscillations in quantum two-level systems: Beyond the area theorem. *Quantum Science and Technology*, 3(1), 014006 (cit. on p. 77).

- Flamini, F., Spagnolo, N., & Sciarrino, F. (2018). Photonic quantum information processing: A review. *Reports on Progress in Physics*, 82(1), 016001 (cit. on p. 8).
- Fukuda, T., Ishikawa, S., Fujii, T., Sakuma, K., & Hosoya, H. (2004). Improvement on asymmetry of low-loss waveguides written in pure silica glass by femtosecond laser pulses. *Optical Fibers and Passive Components*, 5279, 21–28 (cit. on p. 24).
- Galán, J., Sanchis, P., Sánchez, G., & Martí, J. (2007). Polarization insensitive low-loss coupling technique between soi waveguides and high mode field diameter single-mode fibers. *Optics express*, 15(11), 7058–7065 (cit. on pp. 48, 51).
- Gehring, H., Blaicher, M., Hartmann, W., Varytis, P., Busch, K., Wegener, M., & Pernice, W. (2019). Low-loss fiber-to-chip couplers with ultrawide optical bandwidth. *APL Photonics*, 4(1), 010801 (cit. on p. 29).
- Gerry, C., & Knight, P. (2005). *Introductory quantum optics*. Cambridge University Press. (Cit. on p. 16).
- He, M.-Y., Wang, H., Chen, M.-C., Ding, X., Qin, J., Duan, Z.-C., Chen, S., Li, J.-P., Liu, R.-Z., Atatüre, M., Höfling, S., Lu, C.-Y., & Pan, J.-W. (2019). Coherently driving a single quantum two-level system with dichromatic laser pulses. *Nat. Phys.*, 15, 941–946 (cit. on p. 79).
- Heidelberger, C., & Fitzgerald, E. A. (2018). Gaasp/ingap hbts grown epitaxially on si substrates: Effect of dislocation density on dc current gain. *Journal of Applied Physics*, 123(16), 161532 (cit. on p. 25).
- Hepp, S., Jetter, M., Portalupi, S. L., & Michler, P. (2019). Semiconductor quantum dots for integrated quantum photonics (adv. quantum technol. 9/2019). *Advanced Quantum Technologies*, 2(9), 1970053 (cit. on pp. 12, 15).
- Hong, C.-K., Ou, Z.-Y., & Mandel, L. (1987). Measurement of subpicosecond time intervals between two photons by interference. *Physical review letters*, 59(18), 2044 (cit. on pp. 13, 78).
- Höpker, J. P., Gerrits, T., Lita, A., Krapick, S., Herrmann, H., Ricken, R., Quiring, V., Mirin, R., Nam, S. W., Silberhorn, C., et al. (2019). Integrated transition edge sensors on titanium in-diffused lithium niobate waveguides. *APL Photonics*, 4(5), 056103 (cit. on p. 99).
- Hu, W., Sarveswaran, K., Lieberman, M., & Bernstein, G. H. (2004). Sub-10 nm electron beam lithography using cold development of poly (methylmethacrylate). *Journal of Vacuum Science & Technology B: Microelectronics and Nanometer Structures Processing, Measurement, and Phenomena*, 22(4), 1711–1716 (cit. on p. 40).
- Huber, T., Davanco, M., Müller, M., Shuai, Y., Gazzano, O., & Solomon, G. S. (2020). Filter-free single-photon quantum dot resonance fluorescence in an integrated cavity-waveguide device. *Optica*, 7(5), 380–385 (cit. on p. 60).
- Hughes, S. (2004). Enhanced single-photon emission from quantum dots in photonic crystal waveguides and nanocavities. *Optics letters*, 29(22), 2659–2661 (cit. on p. 33).
- Ihn, T. (2010). *Semiconductor nanostructures: Quantum states and electronic transport*. Oxford university press. (Cit. on p. 10).

- Iványi, V., Davidsson, J., Deegan, N., Falk, A. L., Klimov, P. V., Whiteley, S. J., Hruszkewycz, S. O., Holt, M. V., Heremans, F. J., Son, N. T., et al. (2019). Stabilization of point-defect spin qubits by quantum wells. *Nature communications*, 10(1), 1–8 (cit. on p. 7).
- Javadi, A., Mahmoodian, S., Söllner, I., & Lodahl, P. (2018). Numerical modeling of the coupling efficiency of single quantum emitters in photonic-crystal waveguides. *J. Opt. Soc. B*, 35(3), 514–522 (cit. on pp. 22, 33).
- Johansen, J., Julsgaard, B., Stobbe, S., Hvam, J. M., & Lodahl, P. (2010). Probing long-lived dark excitons in self-assembled quantum dots. *Phys. Rev. B*, 81, 081304 (cit. on pp. 18, 56).
- Kako, S., Santori, C., Hoshino, K., Götzinger, S., Yamamoto, Y., & Arakawa, Y. (2006). A gallium nitride single-photon source operating at 200 K. *Nat. Mater.*, 5(11), 887 (cit. on p. 68).
- Kataoka, K. (2010). Estimation of coupling efficiency of optical fiber by far-field method. *Optical review*, 17(5), 476–480 (cit. on p. 52).
- Katsumi, R., Ota, Y., Osada, A., Tajiri, T., Yamaguchi, T., Kakuda, M., Iwamoto, S., Akiyama, H., & Arakawa, Y. (2020). In situ wavelength tuning of quantum-dot single-photon sources integrated on a cmos-processed silicon waveguide. *Applied Physics Letters*, 116(4), 041103 (cit. on pp. 10, 23, 26).
- Kim, J.-H., Aghaeimeibodi, S., Carolan, J., Englund, D., & Waks, E. (2020). Hybrid integration methods for on-chip quantum photonics. *Optica*, 7(4), 291–308 (cit. on pp. 9, 24, 25, 59).
- Kim, J.-H., Aghaeimeibodi, S., Richardson, C. J., Leavitt, R. P., Englund, D., & Waks, E. (2017). Hybrid integration of solid-state quantum emitters on a silicon photonic chip. *Nano letters*, 17(12), 7394–7400 (cit. on pp. 10, 24, 91).
- Kimble, H. J. (2008). The quantum internet. *Nature*, 453(7198), 1023–1030 (cit. on p. 8).
- Kiršanskė, G., Thyrrerstrup, H., Daveau, R. S., Dreeßen, C. L., Pregolato, T., Midolo, L., Tighineanu, P., Javadi, A., Stobbe, S., Schott, R., Ludwig, A., Wieck, A. D., Park, S. I., Song, J. D., Kuhlmann, A. V., Söllner, I., Löbl, M. C., Warburton, R. J., & Lodahl, P. (2017). Indistinguishable and efficient single photons from a quantum dot in a planar nanobeam waveguide. *Phys. Rev. B*, 96, 165306 (cit. on pp. 48, 51, 59, 73).
- Kok, P., Munro, W. J., Nemoto, K., Ralph, T. C., Dowling, J. P., & Milburn, G. J. (2007). Linear optical quantum computing with photonic qubits. *Rev. Mod. Phys.*, 79, 135–174 (cit. on p. 7).
- Kuhlmann, A. V., Houel, J., Ludwig, A., Greuter, L., Reuter, D., Wieck, A. D., Poggio, M., & Warburton, R. J. (2013). Charge noise and spin noise in a semiconductor quantum device. *Nature Physics*, 9(9), 570–575 (cit. on pp. 48, 76).
- Kwiat, P. G., Mattle, K., Weinfurter, H., Zeilinger, A., Sergienko, A. V., & Shih, Y. (1995). New high-intensity source of polarization-entangled photon pairs. *Physical Review Letters*, 75(24), 4337 (cit. on p. 7).
- Laucht, A., Hohls, F., Ubbelohde, N., Gonzalez-Zalba, M. F., Reilly, D. J., Stobbe, S., Schröder, T., Scarlino, P., Koski, J. V., Dzurak, A., et al. (2021). Roadmap on quantum nanotechnologies. *Nanotechnology*, 32(16), 162003 (cit. on p. 6).

- Le Ru, E., Fack, J., & Murray, R. (2003). Temperature and excitation density dependence of the photoluminescence from annealed InAs/GaAs quantum dots. *Physical Review B*, 67(24), 245318 (cit. on p. 13).
- Lindenmann, N., Dottermusch, S., Goedecke, M. L., Hoose, T., Billah, M. R., Onanuga, T. P., Hofmann, A., Freude, W., & Koos, C. (2015). Connecting silicon photonic circuits to multicore fibers by photonic wire bonding. *Journal of Lightwave Technology*, 33(4), 755–760 (cit. on p. 26).
- Liu, F., Brash, A. J., O’Hara, J., Martins, L. M., Phillips, C. L., Coles, R. J., Royall, B., Clarke, E., Bentham, C., Prtljaga, N., Itskevich, I. E., Wilson, L. R., & Fox, A. M. (2018). High Purcell factor generation of indistinguishable on-chip single photons. *Nat. Nanotechnol.*, 13(9), 835 (cit. on p. 60).
- Liu, J., Konthasinghe, K., Davanço, M., Lawall, J., Anant, V., Verma, V., Mirin, R., Nam, S. W., Song, J. D., Ma, B., et al. (2018). Single self-assembled InAs/GaAs quantum dots in photonic nanostructures: The role of nanofabrication. *Physical Review Applied*, 9(6), 064019 (cit. on p. 10).
- Liu, J., Su, R., Wei, Y., Yao, B., da Silva, S. F. C., Yu, Y., Iles-Smith, J., Srinivasan, K., Rastelli, A., Li, J., et al. (2019). A solid-state source of strongly entangled photon pairs with high brightness and indistinguishability. *Nature Nanotechnology*, 14(6), 586–593 (cit. on p. 15).
- Löbl, M. C., Scholz, S., Söllner, I., Ritzmann, J., Denneulin, T., Kovács, A., Kardynał, B. E., Wieck, A. D., Ludwig, A., & Warburton, R. J. (2019). Excitons in InGaAs quantum dots without electron wetting layer states. *Commun. Phys.*, 2(1), 93 (cit. on pp. 11, 64).
- Löbl, M. C., Söllner, I., Javadi, A., Pregolato, T., Schott, R., Midolo, L., Kuhlmann, A. V., Stobbe, S., Wieck, A. D., Lodahl, P., Ludwig, A., & Warburton, R. J. (2017). Narrow optical linewidths and spin pumping on charge-tunable close-to-surface self-assembled quantum dots in an ultrathin diode. *Phys. Rev. B*, 96(16), 165440 (cit. on p. 59).
- Lodahl, P. (2017). Quantum-dot based photonic quantum networks. *Quantum Science and Technology*, 3(1), 013001 (cit. on p. 12).
- Lodahl, P., Mahmoodian, S., & Stobbe, S. (2015). Interfacing single photons and single quantum dots with photonic nanostructures. *Rev. Mod. Phys.*, 87(2), 347 (cit. on pp. 6, 11, 12, 15–18, 21, 22, 47, 51, 59).
- Loredo, J. C., Zakaria, N. A., Somaschi, N., Anton, C., De Santis, L., Giesz, V., Grange, T., Broome, M. A., Gazzano, O., Coppola, G., et al. (2016). Scalable performance in solid-state single-photon sources. *Optica*, 3(4), 433–440 (cit. on p. 60).
- Ludwig, A., Prechtel, J. H., Kuhlmann, A. V., Houel, J., Valentin, S. R., Warburton, R. J., & Wieck, A. D. (2017). Ultra-low charge and spin noise in self-assembled quantum dots. *Journal of Crystal Growth*, 477, 193–196 (cit. on p. 35).
- Ma, J., Sun, Z., Wang, X., & Nori, F. (2012). Entanglement dynamics of two qubits in a common bath. *Phys. Rev. A*, 85, 062323 (cit. on p. 8).
- Malko, A., Baier, M., Karlsson, K., Pelucchi, E., Oberli, D., & Kapon, E. (2006). Optimization of the efficiency of single-photon sources based on quantum dots under optical excitation. *Applied Physics Letters*, 88(8), 081905 (cit. on p. 13).

- Marchetti, R., Lacava, C., Carroll, L., Gradkowski, K., & Minzioni, P. (2019). Coupling strategies for silicon photonics integrated chips. *Photonics Research*, 7(2), 201–239 (cit. on pp. 29, 30).
- Matthiesen, C., Stanley, M. J., Hugues, M., Clarke, E., & Atatüre, M. (2014). Full counting statistics of quantum dot resonance fluorescence. *Scientific reports*, 4(1), 1–6 (cit. on p. 76).
- McNab, S. J., Moll, N., & Vlasov, Y. A. (2003). Ultra-low loss photonic integrated circuit with membrane-type photonic crystal waveguides. *Optics express*, 11(22), 2927–2939 (cit. on p. 48).
- Melet, R., Voliotis, V., Enderlin, A., Roditchev, D., Wang, X., Guillet, T., & Grousseau, R. (2008). Resonant excitonic emission of a single quantum dot in the Rabi regime. *Phys. Rev. B*, 78(7), 073301 (cit. on p. 60).
- Meyer-Scott, E., Silberhorn, C., & Migdall, A. (2020). Single-photon sources: Approaching the ideal through multiplexing. *Review of Scientific Instruments*, 91(4), 041101 (cit. on pp. 7, 9).
- Meystre, P., & Sargent, M. (2007). *Elements of quantum optics*. Springer Science & Business Media. (Cit. on p. 75).
- Midolo, L., Pregolato, T., Kiršanskė, G., & Stobbe, S. (2015). Soft-mask fabrication of gallium arsenide nanomembranes for integrated quantum photonics. *Nanotechnology*, 26(48), 484002 (cit. on pp. 42, 44, 48, 94, 114).
- Mnaymneh, K., Dalacu, D., McKee, J., Lapointe, J., Haffouz, S., Weber, J. F., Northeast, D. B., Poole, P. J., Aers, G. C., & Williams, R. L. (n.d.). On-chip integration of single photon sources via evanescent coupling of tapered nanowires to sin waveguides. *Advanced Quantum Technologies*, 1900021 (cit. on p. 47).
- Monniello, L., Reigue, A., Hostein, R., Lemaitre, A., Martinez, A., Grousseau, R., & Voliotis, V. (2014). Indistinguishable single photons generated by a quantum dot under resonant excitation observable without postselection. *Phys. Rev. B*, 90, 041303 (cit. on p. 60).
- Monroe, C., & Kim, J. (2013). Scaling the ion trap quantum processor. *Science*, 339(6124), 1164–1169 (cit. on p. 7).
- Murray, E., Ellis, D., Meany, T., Floether, F., Lee, J., Griffiths, J., Jones, G., Farrer, I., Ritchie, D., Bennett, A., et al. (2015). Quantum photonics hybrid integration platform. *Applied Physics Letters*, 107(17), 171108 (cit. on pp. 23, 25).
- Najafi, F., Mower, J., Harris, N. C., Bellei, F., Dane, A., Lee, C., Hu, X., Kharel, P., Marsili, F., Assefa, S., et al. (2015). On-chip detection of non-classical light by scalable integration of single-photon detectors. *Nature communications*, 6(1), 1–8 (cit. on p. 26).
- National Academies of Sciences, E., & Medicine. (2019). *Quantum computing: Progress and prospects* (E. Grumbling & M. Horowitz, Eds.). The National Academies Press. (Cit. on pp. 6, 7).
- Novotny, L., & Hecht, B. (2012). *Principles of nano-optics*. Cambridge university press. (Cit. on pp. 16, 17).
- O’Brien, J. L. (2007). Optical quantum computing. *Science*, 318(5856), 1567–1570 (cit. on p. 8).

- O'Brien, J. L., Furusawa, A., & Vučković, J. (2009). Photonic quantum technologies. *Nature Photonics*, 3(12), 687 (cit. on p. 47).
- Ocola, L., & Stein, A. (2006). Effect of cold development on improvement in electron-beam nanopatterning resolution and line roughness. *Journal of Vacuum Science & Technology B: Microelectronics and Nanometer Structures Processing, Measurement, and Phenomena*, 24(6), 3061–3065 (cit. on p. 40).
- Ollivier, H., Thomas, S. E., Wein, S. C., de Buy Wenniger, I. M., Coste, N., Loredò, J. C., Somaschi, N., Harouri, A., Lemaitre, A., Sagnes, I., Lanco, L., Simon, C., Anton, C., Krebs, O., & Senellart, P. (2021). Hong-ou-mandel interference with imperfect single photon sources. *Phys. Rev. Lett.*, 126, 063602 (cit. on p. 71).
- Orobtschouk, R. (2006). On chip optical waveguide interconnect: The problem of the in/out coupling. *Optical interconnects* (pp. 263–290). Springer. (Cit. on p. 52).
- Pan, S., Cao, V., Liao, M., Lu, Y., Liu, Z., Tang, M., Chen, S., Seeds, A., & Liu, H. (2019). Recent progress in epitaxial growth of iii–v quantum-dot lasers on silicon substrate. *Journal of Semiconductors*, 40(10), 101302 (cit. on p. 25).
- Papon, C., Zhou, X., Thyrestrup, H., Liu, Z., Stobbe, S., Schott, R., Wieck, A. D., Ludwig, A., Lodahl, P., & Midolo, L. (2019). Nanomechanical single-photon routing. *Optica*, 6(4), 524–530 (cit. on pp. 10, 47, 56).
- Patterson, J., & Bailey, B. (2010). Optical properties of solids. *Solid-state physics* (pp. 545–590). Springer. (Cit. on p. 12).
- Pedersen, F. T. (2020). *Deterministic single and multi-photon sources with quantum dots in planar nanostructures* (Doctoral dissertation). University of Copenhagen. (Cit. on p. 59).
- Pedersen, F. T., Wang, Y., Olesen, C. T., Scholz, S., Wieck, A. D., Ludwig, A., Löbl, M. C., Warburton, R. J., Midolo, L., Uppu, R., & Lodahl, P. (2020). Near transform-limited quantum dot linewidths in a broadband photonic crystal waveguide. *ACS Photonics*, 7(9), 2343–2349 (cit. on p. 60).
- Pregolato, T., Chu, X.-L., Schröder, T., Schott, R., Wieck, A. D., Ludwig, A., Lodahl, P., & Rotenberg, N. (2020a). Deterministic positioning of nanophotonic waveguides around single self-assembled quantum dots. *APL Photonics*, 5(8), 086101 (cit. on p. 68).
- Pregolato, T. (2019). *Deterministic quantum photonic devices based on self-assembled quantum dots* (Doctoral dissertation). University of Copenhagen. (Cit. on pp. 42, 82, 84, 85).
- Pregolato, T., Chu, X.-L., Schröder, T., Schott, R., Wieck, A. D., Ludwig, A., Lodahl, P., & Rotenberg, N. (2020b). Deterministic positioning of nanophotonic waveguides around single self-assembled quantum dots. *APL Photonics*, 5(8), 086101 (cit. on p. 10).
- PsiQuantum. (2021). Retrieved August 31, 2021, from <https://psiquantum.com/>. (Cit. on pp. 7, 9)
- Quandela. (2021). Retrieved August 31, 2021, from <https://quandela.com/>. (Cit. on pp. 7, 9)
- Quix. (2021). Retrieved August 31, 2021, from <https://www.quix.nl/>. (Cit. on pp. 7, 9)

- Rodt, S., & Reitzenstein, S. (2021). Integrated nanophotonics for the development of fully functional quantum circuits based on on-demand single-photon emitters. *APL Photonics*, 6(1), 010901 (cit. on p. 24).
- Roelkens, G., Van Thourhout, D., Baets, R., Nötzel, R., & Smit, M. (2006). Laser emission and photodetection in an InP InGaAsP layer integrated on and coupled to a silicon-on-insulator waveguide circuit. *Optics express*, 14(18), 8154–8159 (cit. on p. 48).
- Rosencher, E., & Vinter, B. (2002). *Optoelectronics*. Cambridge University Press. (Cit. on p. 89).
- Rudolph, T. (2017). Why I am optimistic about the silicon-photonics route to quantum computing. *APL Photonics*, 2(3), 030901 (cit. on p. 47).
- Salter, C., Stevenson, R., Farrer, I., Nicoll, C., Ritchie, D., & Shields, A. (2010). An entangled-light-emitting diode. *Nature*, 465(7298), 594–597 (cit. on p. 10).
- Sartison, M., Portalupi, S. L., Gissibl, T., Jetter, M., Giessen, H., & Michler, P. (2017). Combining in-situ lithography with 3d printed solid immersion lenses for single quantum dot spectroscopy. *Scientific reports*, 7(1), 1–7 (cit. on p. 29).
- Schleich, W. P., Ranade, K. S., Anton, C., Arndt, M., Aspelmeyer, M., Bayer, M., Berg, G., Calarco, T., Fuchs, H., Giacobino, E., et al. (2016). Quantum technology: From research to application. *Applied Physics B*, 122(5), 130 (cit. on p. 5).
- Schnauber, P., Schall, J., Bounouar, S., Höhne, T., Park, S.-I., Ryu, G.-H., Heindel, T., Burger, S., Song, J.-D., Rodt, S., et al. (2018). Deterministic integration of quantum dots into on-chip multimode interference beamsplitters using in situ electron beam lithography. *Nano Letters*, 18(4), 2336–2342 (cit. on pp. 10, 26).
- Schnauber, P., Singh, A., Schall, J., Park, S. I., Song, J. D., Rodt, S., Srinivasan, K., Reitzenstein, S., & Davanco, M. (2019). Indistinguishable photons from deterministically integrated single quantum dots in heterogeneous GaAs/Si₃N₄ quantum photonic circuits. *Nano letters*, 19(10), 7164–7172 (cit. on p. 26).
- Schweickert, L., Jöns, K. D., Zeuner, K. D., Covre da Silva, S. F., Huang, H., Lettner, T., Reindl, M., Zichi, J., Trotta, R., Rastelli, A., & Zwiller, V. (2018). On-demand generation of background-free single photons from a solid-state source. *Appl. Phys. Lett.*, 112(9), 093106 (cit. on pp. 10, 77).
- Seidl, S., Kroner, M., Dalgarno, P. A., Högele, A., Smith, J. M., Ediger, M., Gerardot, B. D., Garcia, J. M., Petroff, P. M., Karrai, K., & Warburton, R. J. (2005). Absorption and photoluminescence spectroscopy on a single self-assembled charge-tunable quantum dot. *Phys. Rev. B*, 72, 195339 (cit. on p. 17).
- Shields, A. J. (2010). Semiconductor quantum light sources. *Nanoscience And Technology: A Collection of Reviews from Nature Journals*, 221–229 (cit. on p. 15).
- Sibson, P., Erven, C., Godfrey, M., Miki, S., Yamashita, T., Fujiwara, M., Sasaki, M., Terai, H., Tanner, M. G., Natarajan, C. M., et al. (2017). Chip-based quantum key distribution. *Nature communications*, 8(1), 1–6 (cit. on pp. 23, 26).
- Smit, M., Leijtens, X., Ambrosius, H., Bente, E., Van der Tol, J., Smalbrugge, B., De Vries, T., Geluk, E.-J., Bolk, J., Van Veldhoven, R., et al. (2014). An introduction to InP-based generic integration technology. *Semiconductor Science and Technology*, 29(8), 083001 (cit. on p. 24).

- Snijders, H., Frey, J., Norman, J., Bakker, M., Langman, E., Gossard, A., Bowers, J., Van Exter, M., Bouwmeester, D., & Löffler, W. (2016). Purification of a single-photon nonlinearity. *Nature communications*, 7(1), 1–6 (cit. on p. 15).
- Snyder, A. W., & Love, J. (2012). *Optical waveguide theory*. Springer Science & Business Media. (Cit. on p. 52).
- Somaschi, N., Giesz, V., De Santis, L., Loredò, J., Almeida, M. P., Hornecker, G., Portalupi, S. L., Grange, T., Antón, C., Demory, J., Gómez, C., I., S., Lanzillotti-Kimura, N. D., Lemaître, A., A., A., White, A. G., Lanco, L., & Senellart, P. (2016). Near-optimal single-photon sources in the solid state. *Nat. Photonics*, 10(5), 340 (cit. on pp. 10, 15, 21, 56, 60, 73).
- Son, G., Han, S., Park, J., Kwon, K., & Yu, K. (2018). High-efficiency broadband light coupling between optical fibers and photonic integrated circuits. *Nanophotonics*, 7(12), 1845–1864 (cit. on p. 29).
- Sparrow. (2021). Retrieved August 31, 2021, from <https://sparrowquantum.com/>. (Cit. on pp. 7, 9)
- Sprengers, J. P., Gaggero, A., Sahin, D., Jahanmirinejad, S., Frucci, G., Mattioli, F., Leoni, R., Beetz, J., Lermer, M., Kamp, M., Höfling, S., Sanjines, R., & Fiore, A. (2011). Waveguide superconducting single-photon detectors for integrated quantum photonic circuits. *Appl. Phys. Lett.*, 99(18), 181110 (cit. on p. 47).
- Stanley, M. J., Matthiesen, C., Hansom, J., Le Gall, C., Schulte, C. H. H., Clarke, E., & Atatüre, M. (2014). Dynamics of a mesoscopic nuclear spin ensemble interacting with an optically driven electron spin. *Phys. Rev. B*, 90, 195305 (cit. on p. 76).
- Sun, J., Timurdogan, E., Yaacobi, A., Hosseini, E. S., & Watts, M. R. (2013). Large-scale nanophotonic phased array. *Nature*, 493(7431), 195–199 (cit. on p. 24).
- Thyrrerstrup, H., Kiršanskė, G., Le Jeannic, H., Pregolato, T., Zhai, L., Raahauge, L., Midolo, L., Rotenberg, N., Javadi, A., Schott, R., Wieck, A. D., Ludwig, A., Löbl, M. C., Söllner, I., Warburton, R. J., & Lodahl, P. (2018). Quantum optics with near-lifetime-limited quantum-dot transitions in a nanophotonic waveguide. *Nano Lett.*, 18(3), 1801–1806 (cit. on pp. 56, 60).
- Tiecke, T., Nayak, K., Thompson, J. D., Peyronel, T., de Leon, N. P., Vuletić, V., & Lukin, M. (2015). Efficient fiber-optical interface for nanophotonic devices. *Optica*, 2(2), 70–75 (cit. on pp. 27, 30).
- Tighineanu, P., Dreessen, C. L., Flindt, C., Lodahl, P., & Sørensen, A. S. (2018). Phonon decoherence of quantum dots in photonic structures: Broadening of the zero-phonon line and the role of dimensionality. *Phys. Rev. Lett.*, 120(25), 257401 (cit. on p. 69).
- Tomm, N., Javadi, A., Antoniadis, N. O., Najer, D., Löbl, M. C., Korsch, A. R., Schott, R., Valentin, S. R., Wieck, A. D., Ludwig, A., et al. (2021). A bright and fast source of coherent single photons. *Nature Nanotechnology*, 1–5 (cit. on pp. 10, 14, 15, 73).
- Uğurlu, A., Thyrrerstrup, H., Uppu, R., Ouellet-Plamondon, C., Schott, R., Wieck, A. D., Ludwig, A., Lodahl, P., & Midolo, L. (2019). Suspended spot-size converters

- for scalable single-photon devices. *Adv. Quantum Technol.*, 3, 1900076 (cit. on pp. 31, 47, 85).
- Unsleber, S., He, Y.-M., Gerhardt, S., Maier, S., Lu, C.-Y., Pan, J.-W., Gregersen, N., Kamp, M., Schneider, C., & Höfling, S. (2016). Highly indistinguishable on-demand resonance fluorescence photons from a deterministic quantum dot micropillar device with 74% extraction efficiency. *Optics express*, 24(8), 8539–8546 (cit. on p. 15).
- Uppu, R., Eriksen, H. T., Thyrrstrup, H., Uğurlu, A., Wang, Y., Scholz, S., Wieck, A. D., Ludwig, A., Löbl, M. C., Warburton, R. J., Lodahl, P., & Midolo, L. (2020). On-chip deterministic operation of quantum dots in dual-mode waveguides for a plug-and-play single-photon source. *Nature Communications*, 11(1), 1–6 (cit. on pp. 9, 59, 60, 69).
- Uppu, R., Midolo, L., Zhou, X., Carolan, J., & Lodahl, P. (2021). Single-photon quantum hardware: Towards scalable photonic quantum technology with a quantum advantage. *arXiv preprint arXiv:2103.01110* (cit. on pp. 8, 24, 91).
- Uppu, R., Pedersen, F. T., Wang, Y., Olesen, C. T., Papon, C., Zhou, X., Midolo, L., Scholz, S., Wieck, A. D., Ludwig, A., & Lodahl, P. (2020). Scalable integrated single-photon source. *Science Advances*, 6(50) (cit. on pp. 14, 15, 21, 59, 60).
- Vigliar, C., Paesani, S., Ding, Y., Adcock, J. C., Wang, J., Morley-Short, S., Bacco, D., Oxenløwe, L. K., Thompson, M. G., Rarity, J. G., et al. (2020). Error protected qubits in a silicon photonic chip. *arXiv preprint arXiv:2009.08339* (cit. on p. 9).
- Wahlbrink, T., Tsai, W. S., Waldow, M., Först, M., Bolten, J., Mollenhauer, T., & Kurz, H. (2009). Fabrication of high efficiency soi taper structures. *Microelectronic Engineering*, 86(4-6), 1117–1119 (cit. on p. 94).
- Wang, C., Zhang, M., Stern, B., Lipson, M., & Lončar, M. (2018). Nanophotonic lithium niobate electro-optic modulators. *Optics express*, 26(2), 1547–1555 (cit. on p. 24).
- Wang, H., Duan, Z.-C., Li, Y.-H., Chen, S., Li, J.-P., He, Y.-M., Chen, M.-C., He, Y., Ding, X., Peng, C.-Z., Schneider, C., Kamp, M., Höfling, S., Lu, C.-Y., & Pan, J.-W. (2016). Near-transform-limited single photons from an efficient solid-state quantum emitter. *Phys. Rev. Lett.*, 116, 213601 (cit. on pp. 60, 79).
- Wang, H., He, Y.-M., Chung, T.-H., Hu, H., Yu, Y., Chen, S., Ding, X., Chen, M.-C., Qin, J., Yang, X., et al. (2019a). Towards optimal single-photon sources from polarized microcavities. *Nature Photonics*, 13(11), 770–775 (cit. on pp. 21, 60, 73).
- Wang, H., He, Y.-M., Chung, T.-H., Hu, H., Yu, Y., Chen, S., Ding, X., Chen, M.-C., Qin, J., Yang, X., Liu, R.-Z., Duan, Z.-C., Li, J.-P., Gerhardt, S., Winkler, K., Jurkat, J., Wang, L.-J., Gregersen, N., Huo, Y.-H., ... Pan, J.-W. (2019b). Towards optimal single-photon sources from polarized microcavities. *Nat. Photon.*, 13, 770–775 (cit. on pp. 14, 15).
- Wang, J., Bonneau, D., Villa, M., Silverstone, J. W., Santagati, R., Miki, S., Yamashita, T., Fujiwara, M., Sasaki, M., Terai, H., et al. (2016). Chip-to-chip quantum photonic interconnect by path-polarization interconversion. *Optica*, 3(4), 407–413 (cit. on pp. 23, 26).
- Wang, J., Paesani, S., Ding, Y., Santagati, R., Skrzypczyk, P., Salavrakos, A., Tura, J., Augusiak, R., Mančinska, L., Bacco, D., Bonneau, D., Silverstone, J. W., Gong,

- Q., Acín, A., Rottwitt, K., Oxenløwe, L. K., O'Brien, J. L., Laing, A., & Thompson, M. G. (2018). Multidimensional quantum entanglement with large-scale integrated optics. *Science*, *360*(6386), 285–291 (cit. on p. 24).
- Wang, J., Sciarrino, F., Laing, A., & Thompson, M. G. (2019). Integrated photonic quantum technologies. *Nat. Photon.*, 1–12 (cit. on pp. 8, 10, 24).
- Wang, Y. (2021). *Novel nanofabrication methods and processes for quantum photonic integrated circuits* (Doctoral dissertation). University of Copenhagen. (Cit. on p. 34).
- Wang, Y., Uppu, R., Zhou, X., Papon, C., Scholz, S., Wieck, A. D., Ludwig, A., Lodahl, P., & Midolo, L. (2021). Electroabsorption in gated GaAs nanophotonic waveguides. *Applied Physics Letters*, *118*(13), 131106 (cit. on p. 10).
- Wei, Y.-J., He, Y.-M., Chen, M.-C., Hu, Y.-N., He, Y., Wu, D., Schneider, C., Kamp, M., Höfling, S., Lu, C.-Y., & Pan, J.-W. (2014). Deterministic and robust generation of single photons from a single quantum dot with 99.5% indistinguishability using adiabatic rapid passage. *Nano Lett.*, *14*(11), 6515–6519 (cit. on p. 79).
- Weisskopf, V., & Wigner, E. (1997). Berechnung der natürlichen linienbreite auf grund der Diracschen Lichttheorie. *Part i: Particles and fields. part ii: Foundations of quantum mechanics* (pp. 30–49). Springer. (Cit. on p. 16).
- Xanadu. (2021). Retrieved August 31, 2021, from <https://www.xanadu.ai/>. (Cit. on pp. 7, 9)
- Zadeh, I. E., Elshaari, A. W., Jöns, K. D., Fognini, A., Dalacu, D., Poole, P. J., Reimer, M. E., & Zwiller, V. (2016). Deterministic integration of single photon sources in silicon based photonic circuits. *Nano Letters*, *16*(4), 2289–2294 (cit. on pp. 23, 26).
- Zhang, M., Wang, C., Cheng, R., Shams-Ansari, A., & Lončar, M. (2017). Monolithic ultra-high-Q lithium niobate microring resonator. *Optica*, *4*(12), 1536–1537 (cit. on p. 24).
- Zhong, H.-S., Wang, H., Deng, Y.-H., Chen, M.-C., Peng, L.-C., Luo, Y.-H., Qin, J., Wu, D., Ding, X., Hu, Y., et al. (2020). Quantum computational advantage using photons. *Science*, *370*(6523), 1460–1463 (cit. on p. 8).
- Zhou, X., Kulkova, I., Lund-Hansen, T., Hansen, S. L., Lodahl, P., & Midolo, L. (2018). High-efficiency shallow-etched grating on GaAs membranes for quantum photonic applications. *Appl. Phys. Lett.*, *113*(25), 251103 (cit. on p. 61).